STRUCTURE AND PROPERTIES OF LIGAND-CAPPED GOLD NANOPARTICLES

Thesis submitted in accordance with the requirements of the University of Liverpool for the degree of Doctor in Philosophy

by

Christopher Paul Shaw

September 2011

ABSTRACT

Thiolated ligands are known to form self-assembled monolayers on gold nanoparticles, and the self-organisation of these ligands provides a route towards nanoparticles with programmable and complex molecular structures. This body of work investigates the structures and chemical properties of ligand monolayers based on peptides and alkanethiol derivatives. We evaluate a series of published articles reporting the peculiar self-organisation of ligands into striated domains on the surface of nanoparticles, which was shown by scanning tunnelling microscopy (STM). Image analysis of the STM micrographs shows the stripe-like domains to be scanning artefacts, and our attempts to reproduce data on nanoparticle stability and cell entry give results conflicting with those published. Self-assembled monolayers made from peptides allow the use of peptide motifs to drive self-organisation. We investigate the effects of using an amyloidogenic sequence, CFGAILSS, in a monolayer. FTIR, 2DIR and solid state NMR reveal the presence of inter-peptide hydrogen bonding consistent with a parallel β-sheet structure, which is not seen in a monolayer made from the CALNN peptide. Fluorescently labelled peptide-capped gold nanoparticles were irradiated by a femtosecond laser pulse. The timings of the reaction dynamics of this ligand release were measured by splitting the laser beam and introducing a variable delay. These measurements show that this process is a hot electron mediated process. We suggest that such laser induced release measurements can provide some insights into the intermolecular interactions within the monolayer

CONTENTS

LIST OF FIGURES

ACKNOWLEDGMENTS

I wish to firstly thank my supervisors, Dr Raphaël Lévy and Prof. David Fernig, for their help and guidance throughout this project and without whom none of this work would be possible. I would like to say thank you to Dr Martin Volk for introducing me to FTIR and his often-fruitful interest in my research. A sincere thank you goes to group members of old and new, Dr Paul Free, Dr. Yann Cesbron, Dr Nicolas Schaeffer, Umbreen Shaheen, Dan Nieves and Dr Lara Bogart. I also thank Dr Paul Donaldson for his discussion and rewarding colaborations. I would also like to thank all members of Lab D, old and new, for creating a highly enjoyable atmosphere both in and out of work.

Finally I would like to thank Joanne Denyer, and my parents Christopher and Brenda Shaw, without whose love and continual support I would not have undertaken this project.

My whole post-graduate experience at Liverpool University has been extremely rewarding, and changed my way of thinking. I strongly believe my experiences will help me not only now, but in many years to come.

CHAPTER 1

An introduction to nanoscale self-assembly and self-organisation

1.1. Nanotechnology

A nanoparticle is recognised as an object with at least one dimension on the order of less than ~100 nm. This term encompasses many shapes such as rods [1], cubes [2] and spheres [3] to name but a few. Here we focus on spherical nanoparticles to use as building blocks towards biologically inspired nanomaterials.

1.2. Gold nanoparticles

Noble metal nanoparticles, in particular gold, are excellent candidates for emerging nano-based technologies because of their strongly size-dependent electronic [4], optical [5,6], and catalytic [7] properties.

Gold nanoparticles have been known since approximately 400 AD where they were used to stain glass. It wasn't until Michael Faraday's work in 1857 however that their difference in colour to bulk gold was attributed to their small size. The colour of a suspension of gold nanoparticles strongly depends on their size. [8] Nanoparticles range from yellow for the smallest nanoparticles through brown, orange, red, purple and finally blue for the largest. This vivid colour caused by the localised surface plasmon resonance (LSPR). This is observed as

a strong absorbance between 500 nm and 575 nm [1]. Surface plasmons are the collective oscillation of surface conduction electrons and resonant energy transfer occurs between these and photons. Since the LSPR is a surface property, it is sensitive to changes in the size and shape of the particle. Adsorbed ligands alter the refractive index around the particle and thus can red shift the position of the SPR by approximately 4 nm. [8] The refractive index of the medium also affects the surface plasmon band absorbance [8].

1.3. Colloidal stability

In the 1940s Deryagin, Landau, Vewey and Overbeek developed a theory to describe the stability of colloids (DVLO theory). This theory describes the colloidal stability as determined by the balance of potential energy of the attractive Van der Waals interaction and the potential energy of the repulsive electrostatic interaction.

Due to Brownian motion, convection or gravity, particles in a colloidal suspension collide with one another. These collisions can result either in repulsion or aggregation. As particles are brought closer together they are attracted to each other by van der Waals forces. If a collision is to result in aggregation the van der Waals interaction must be greater than the repulsion. If a suspension of particles is to maintain colloidal stability the force of repulsion must balance the force of attraction. A fundamental mechanism by which colloids are prevented from aggregating is by electrostatic stabilisation. The repulsive Coulomb forces counterbalance the van der Waals forces between charged particles. A charged particle's surface attracts a layer of

counter ions, with opposite charge to the surface charge, and are held in place by electrostatic force forming the Stern layer. The Stern layer is then covered by a layer of solvent forming a diffuse layer containing a higher concentration of the positive counter ions. These layers form the electric double layer surrounding the particle providing the electrostatic charge that contributes to electrostatic stabilisation. The ionic content of the solution can cause screening of this electrostatic repulsion leading to aggregation.

1.4. Capping with ligands to increase colloidal stability

It is possible to exchange the stabilising counter ions on the particle surface that provide only electrostatic repulsion, for larger organic ligands that also provide a steric barrier to aggregation. Many types of compounds have been used to date, including nucleic acids, [9-11] peptides, [12-14] polymers, [15] alkanethiols, [16] and polyethylene glycols. [17] There have also been reports of inorganic compounds such as phosphines [18] and tungsten oxides [19] used as ligands. Gold readily bonds with a thiol group to form a strong covalent bond that is used frequently to anchor ligands to nanoparticles. These ligands are not only useful as means to stabilise nanoparticles, but also as a way to introduce functionality. Ligands incorporating molecular recognition motifs [14], and fluorophores [20,21] have received wide interest, due to their applications in assays and as molecular delivery vehicles [22]

1.5. Self organisation of ligands

1.5.1. Bio-inspired nanotechnology

Molecular self-assembly is a central theme of biochemistry and molecular biology. Self-assembly drives the folding of biological polymers (proteins and nucleic acids) and the formation of membranes. Perhaps more pertinent is the realisation that biological molecules do not function alone, but in macromolecular assemblies, which form reversibly and dynamically, readily changing components to gain new functionalities. Some of these assemblies are nanoscale machines, producing motion (molecular motors, kinesin, dyenin, myosin), in some instances processive (RNA and DNA synthesizing complexes [23]) or cleaving polymers in a Fordist assembly line fashion [24]. Artificial complex structures have been built in particular using the programmable properties of DNA and RNA [25], proteins [26] or peptides [27]. Bottom up self-assembly of several different nanometre sized non-biological building blocks into one functional device remains, however, a major challenge. Such nanoengineering requires the ability to model, design, produce, and characterize complex nanoparticles that have well-defined orthogonal interactions.

1.5.2. Controlling nanoparticle assembly

Assembly, as aggregation or coagulation of colloids has been studied in depth over the past decades, because of its fundamental importance to many industrial processes, from paint formulation to waste water treatment. Depending on whether the process is limited by diffusion of the colloid, or by the sticking probability (reaction

limited), different structures are obtained, characterized by different fractal dimensions of the aggregates [28]. Gold particles were used as an exemplary colloid in some of the early studies, and nearly half a century ago, Turkevich and Enustun reported how varying the solution parameters between particles allowed the control of the formation of aggregates of 20 nm citrate gold nanoparticles [29]. They observed and discussed the formation of remarkably linear aggregates in the case of slow coagulation at low ionic strength, when the repulsion between nanoparticles is reduced by partly neutralizing the surface charge. An example of such linear aggregates, from the original 1963 article, is reproduced in figure 1.1a. Further linear aggregates were observed by other authors, and in particular by Lin *et al.* who varied systematically the degree of substitution of citrate with 2-mercaptoethanol [30] (Fig. 1a, and additional discussion of this study in section 5). Progress in the functionalization of nanoparticles has allowed advances well beyond fine tuning of the balance between electrostatic and Van der Waals interactions. Specific biological interactions such as those of nucleic acids [11] and peptides [31], as well as non-biological interactions using, for example, polymers [32], have been employed to mediate the interaction between nanoparticles (Fig. 1b). These interactions were used to control not only the dynamics of nanoparticle aggregation, but also the spatial arrangement of different building blocks and to form responsive assemblies that could be disassembled upon a particular stimulus [9]. The same interactions can be used to direct the nanoparticles to assemble along predesigned templates [33]. Templates made from polymers (synthetic or biological) allow some control of the spatial arrangement of nanoparticles [34] (Fig. 1E and F), but little in

terms of total assembly size. In an early example by Rotello and co workers, a polymer was used that made nanoparticles assemble into large spherical aggregates of a controlled size range [32]. The 2 nm diameter nanoparticles, when assembled along the polymer, formed regularly sized spherical aggregates around 97 nm in diameter (Fig. 1G). In a later study by Mastroianni *et al.* a smaller template made from DNA allows both positional control and limited size control [35] (Fig. 1H). In these two examples the template controls the complexity of the assembly. Sardar et al. shown that by controlling the nanoparticle surface ligand position the formation of one-dimensional chains was possible [36] (Fig. 1I). Further discussion of this work is in section 4. These examples, whilst showing some control over nanoparticle assembly, enable little control over the resultant geometric complexity. To date no published assembly techniques enable control over both the number of particles beyond dimers, trimers or tetramers with complete control over the resultant geometry [31,37]. As the technology has evolved the assembly methods and interface by which each constituent particle interacts has become more specific. Starting with some non-specific interactions published by Turkevich [29] studies have gone on to control the valency [38,39], exhibit some relative positional control using both ligands [40] and using large oligomeric templates to influence the size and relative position [34]. Templates densely decorated with particles have been shown to be a route to forming nanowires [41]. Working examples of computer based simulation studies [42], however, have yet to be realized due to, in part, a lack of techniques that efficiently and reproducibly result in particles exhibiting several simultaneous levels of relative ligand positional control.

Molecular simulations of nanoparticles with highly organised ligand shells show that complex networks of particles may be produced by precisely controlling the positioning of these functional ligands [42] [43]. Current methods, however, do not impart such a degree of control. Moreover, we lack a critical understanding of how ligands on the surface of nanomaterials organise themselves around nanoparticles and the factors that govern this process.

Molecular level understanding of the structure of the biofunctionalised building block is integral to the realization of complex assemblies. In the studies mentioned above UV/Visible spectroscopy and TEM were the key nanoparticle characterisation techniques. It should be noted nm) with a small number of atoms, due to more stable preferred numbers of gold atoms in a nanoparticle (magic numbers) [45] arising from closed geometric atomic shells. This has enabled the recent report of the first gold nanoparticle crystal structure, with a resolution of 1.1 Å [46]. The topography of nanoparticles compared to flat surfaces makes characterisation difficult for scanning probe techniques such

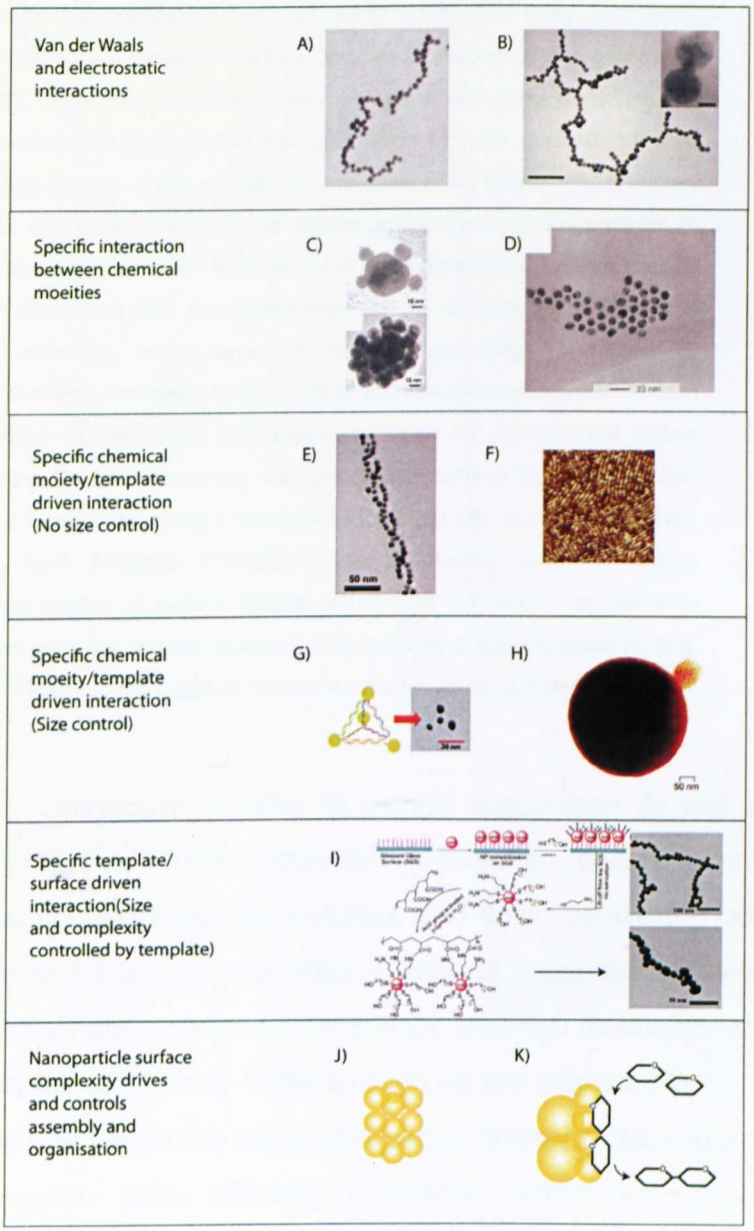

Figure 1.1 Nanoparticle interaction and assembly; Linear assembly driven by Van der Waals forces and electrostatic interactions A) (Reprinted with

permission from ref. 29, © 1962 American Chemical Society) and B) (Reprinted with permission from ref. 30 © 2005 John Wiley and Sons). Using chemical moieties to interface particles C) (Reprinted with permission from ref. 31 © 2005 American Chemical Society) with some limited control on stoichiometry D) (Reprinted with permission from ref. 9 © 1996 Nature Publishing Group). Using a molecular self-assembled template (respectively peptide and DNA) to control the spacial arrangement of nanoparticles E) (Reprinted with permission from ref. 34 © 2008 American Chemical Society) and F) (Reprinted with permission from ref. 10 © 2006 John Wiley and Sons). Achieving overall assembly size control using a template G) (Reprinted with permission from ref. 35 © 2009 American Chemical Society) or polymer H) (Reprinted with permission from ref. 32 © 2000 Nature Publishing Group). Controlling the nanoparticle surface ligand distribution allows it to assemble along a template I) (Reprinted with permission from ref. 36 © 2008 American Chemical Society). Attaining complete relative positional control of surface ligands would then not require templates to produce complex shaped assemblies J) performing specific tasks K) (e.g. nanoparticles coming together to form a complex analogous to an enzyme).

that TEM is intrinsically sensitive to sample preparation as well as experimenter's bias during acquisition. Therefore careful control experiments should always be included, and entire datasets should be provided as supporting information instead of single representative pictures. Since nanoparticles exhibit surface plasmon resonance and are electron dense, both of these techniques are very sensitive and can indicate changes in the nanoparticle environment, surface ligands and aggregation state allowing substantial information to be obtained[5,8,44]. Due to the limitations of current synthesis methods, size polydispersity means that some structural biology techniques, such as crystallography are usually not applicable. For smaller sizes, it is possible to synthesise sufficiently monodisperse nanoparticles (<2 as

atomic force microscopy (AFM) and scanning tunnelling microscopy (STM) at sub-nanometre resolution, due to the relatively large variations in sample surface height. Techniques that are used for structural biology such as Fourier transform infrared spectroscopy and solid state NMR show promise and can provide information on interactions between ligands, as well the presence of any long range order [32,47,48]. If we are to build more complex nanomaterials, methods for precisely indicating and controlling the relative spatial arrangement of ligands on a nanoparticle surface will be critical.

1.5.3 Are SAMs on gold nanoparticles dynamic?

The formation and properties of self-assembled monolayers of thiolated ligands on gold nanoparticles is well understood thanks to over two decades of research [49]. The ligand adsorption configurations [50] on flat Au(111) surfaces have been studied in addition to monolayer defects [51] as well as how mixtures of thiolates form phase separated domains on the surface [52], where some ligands preferentially adsorb to the surface over others. The formation of a self-assembled monolayer is spontaneous and brought about by several interacting processes. Ligands in solution chemisorb to a surface, replacing existing adsorbed species due to a stronger surface interaction and/or a higher concentration [53]. Ligands in mixed SAMs form islands and patches rather than a random mixture as shown by AFM. In 2000 a study by Rotello and co-workers provided evidence to support the mobility of thiolated ligands on a gold nanoparticle surface [40].

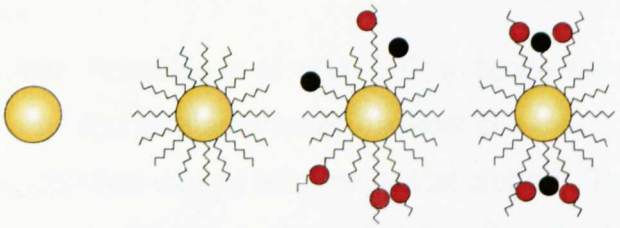

Figure. 1.2 Schematic representation of the degree of controlled complexity of a gold nanoparticle building block; a) bare, uncapped gold nanoparticle b) gold nanoparticle protected by ligand shell c) multifunctional gold nanoparticle d) multifunctional gold nanoparticle monolayer with precisely controlled placement of thiolate ligands to form surface structures. Reprinted with permission from ref. 54 © 2010 Journal of Materials Chemistry.

Nanoparticles coated with three different ligands, two of which bind to flavin, were examined under NMR in the presence of flavin. The flavin protons were monitored over 73 hours and a smooth downfield shift of ~200 ppb was observed over the time course, indicative of an increase of colloid-flavin recognition. More recently, however, thiolated ligands bound to a gold nanoparticle surface have been shown to exhibit virtually no lateral diffusion at room temperature and only very slow motility at raised temperatures (90°C) using electron paramagnetic partial randomization of ligands within the monolayer, whilst in the second system, where the ligand contained a carboxylic acid group, the ligands moved toward each other, presumably driven in part by hydrogen bonding of the carboxylic acid groups. It is worth noting, however, that discrete ligand domains produced by printing or nanolithographic techniques remain unchanged for months, indicating that very little, or no ligand motility is occurring on flat, densely packed SAMs. Presumably, the lateral diffusion of thiolate ligands on a

surface will depend heavily on the ligand itself and the density of the monolayer.

More recently Pasquato *et al.* used ESR to probe the segregation of perfluoroalkyl and alkyl amphiphilic thiolates in a mixed monolayer on a gold nanoparticle using a nitroxide radical probe [55]. The particles are initially capped with the perfluoroalkyl ligand and alkyl ligands are introduced via ligand exchange. The probe was found to mainly be present in islands of perfluorinated ligands, until the ratio of alkyl/perfluoroalkyl became >2.5. The overall behaviour was consistent with a phase separated system, rather than a homogeneous binary mixture. Whilst, it has been previously observed that phase separation occurs in Langmuir monolayers [56], micelles [57], and liposomes [58], this was the first spectroscopic evidence of the formation of domains in a 3-D SAM on nanoparticles.

Using a different approach, Duchesne *et al.* formed gold nanoparticles with a very small number (at the limit, just one) of a functional ligand within a SAM of matrix ligands that could be cross-linked [12]. When these peptide ligands were <4 nm away from another ligand, they would preferentially cross-link to their neighbour; when the separation distance was greater, the ligand would crosslink to itself. Using this proximity probe, the authors were able to show that these peptide ligands inserted themselves into the monolayer at very close proximity, even when only two or three ligands were present. The results also indicated that the formation of the patches is a cooperative process occurring during the assembly of the ligand shell, presumably to minimise the contact surfaces between two types of

ligands. More recent work supports the idea that a ligand monolayer forms through a mechanism whereby the initial bound ligand cooperatively promotes further ligand binding to form islands on the surface. In a particularly elegant study, Weinstock *et al.* label a monolayer of polyoxometalates (POM) on gold nanoparticles with tungsten ions and visualised these under cryo-TEM [19]. The authors visualise and resolve both the formation of the monolayer and individual ligands, as the nuclei of the 11 Tungsten atoms per POM scatter electrons much more effectively than their organic equivalents. The study shows that the ligands form the monolayer in patches rather than at random, perhaps to minimise the ligands contact with the solution. A different model of ligand organisation was presented in a series of studies starting in 2004, which reported the existence of "stripy" domains of alternating hydrophobic and hydrophilic ligands on the surface of small nanoparticles [59]. However the interpretation of these results and the existence of stripy nanoparticles is controversial (Chapter 2).

1.5.4. Control of stoichiometry and position of ligands

In order to regulate the reactivity of nanoparticles, it is important to gain accurate control of the surface chemical functionality. A way by which this can be achieved is through controlling the stoichiometry of functional ligands (Figure 1.2).

The first example of the synthesis of monovalent nanoparticles used an eleven atom gold cluster, 0.8 nm diameter, conjugated to an antibody [60]. A mixture of non-functional and functional ligands was added. The 0.8 nm diameter gold core is able to have 7 ligands and

here the ligands were mixed in a 1:6 ratio of functional to non-functional ligand. This would obviously give a population of particles with no functional ligand, but these are removable by ion-exchange chromatography. Levy and co-workers used a method based on immobilized metal ion affinity chromatography [39]. The nanoparticle surface was passivated with a monolayer of CALNN peptide and a small number of functional ligands containing a classic molecular biology tag, a sequence of six histidine residues, which binds immobilized divalent cations and a biotin. This functional peptide was present at a low enough concentration during the monolayer formation that particles that did have this ligand only had one, resulting in a nanoparticle population where many particles had no functional ligands. Particles that did contain a functional ligand in their monolayer could be separated using affinity chromatography. An analogous approach has used an alkanethiol terminated by ethylene glycol and a tris-nitriloacetic acid. [61,62] The latter chelates divalent metal cations and can bind hexahistidine tags found in recombinant proteins. Again, by incorporating a low mole percentage of the tris-nitriloaceitic acid containing ligand with respect to the matrix ligands, monovalently functionalised nanoparticles were produced. These were purified by affinity chromatography and coupled stoichiometrically to different recombinant proteins and a protein-based nanofibre [63 64]. This method can be applied to any nanomaterial that can be capped with a ligand that allows affinity chromatography. This list is by no means exhaustive and there have been many other methods to control the ligand stoichiometery on gold nanoparticles [38,65].

1.5.5. Templates for positional control

The structure of spherical nanoparticles capped with mixture of small molecules can be, in first instance, described by two information parameters; the stoichiometry of any species of ligands with respect to the nanoparticle, i.e. the chemical composition of the monolayer, and the position of the different ligands relative to one another on the nanoparticle. One way that the positional information can be imparted upon a nanoparticle is by using a template. Chemically directing the placement of ligand molecules on a surface allows the design and control of the surface properties, with a resolution limited by the template. Flat surfaces can be patterned using many techniques. Nanolithography is most commonly used in the fabrication of semiconductor processors with nanoscale features, masking certain areas and removing others. Using a similar technique, thiols can be stamped onto a surface using a polymer relief pattern in a process called microcontact printing [66 68]. This allows the facile creation of micron scale features. Even smaller features are possible using dip pen nanolithography, where an atomic force microscope precisely deposits individual thiolates onto a gold surface [69,70]. However, these techniques have been designed to be used on flat surfaces. Since nanoparticles are a 3-D surface, where all facets of the particle would require ligand attachment, these methods would be extremely difficult to implement. A more effective way of producing a patterning mask for a nanoparticle would be to use a large molecule to bind to the surface. Many molecules to date have been used as templates ranging from DNA and peptides to polymers.

An example of the latter approach is the work of Schumaker-Parry and co-workers, who reported asymmetrically functionalised gold nanoparticles that can be organised into one-dimensional chains along a polymer chain [36]. By immobilising the nanoparticles on a surface and effectively masking one side, the exposed particle face is selectively covered with one species of carboxylic acid terminated ligands. The particles are removed from the surface and the now bare face is functionalised with amine-terminated thiols. These "Janus" particles can now be coupled to an activated carboxylic acid polymer. The particles form a 1-D structure along the polymer that was observed by TEM and plasmon coupling. The formation of this 1-D array is evidence that the asymmetric functionalisation has succeeded.

It is possible, however, to functionalise nanoparticles anisotropically in solution, albeit with less control. A paper by Lin *et al.* shows how, when citrate from synthesis is ligand-exchanged with 2-mercaptoethanol, at the correct ratio, the resulting particles form branched one-dimensional chains with no template used [30]. This highly anisotropic behaviour is explained by the presence of an electric dipole moment when sufficient citrate is exchanged on the nanoparticle. When the mercaptoethanol content is sufficiently high the authors suggest that this forms a permanent dipole on the nanoparticle surface. It is unclear whether the mercaptoethanol ligand has a preference for a particular crystal face on the gold nanoparticle. Again this study provides evidence for progressive anisotropic formation of monolayers through patches. Ligands adsorbing to a

nanoparticle surface anisotropically is the underlying principle of the growth of nanorods by cetyl trimethylammonium bromide (CTAB), where the CTAB has a preference for a particular crystal face of the particle [71]. Mirkin and co-workers anisotropically functionalised gold particles using magnetic nanoparticles as template masks [72]. The larger magnetic particle was used to functionalise a small localised region on the surface of smaller gold nanoparticles, both sets of particles being DNA-capped. Gold particles attached to the magnetic particles could then be removed from the bulk colloid, selecting the asymmetrically functionalised particles. Whilst this method does not control the stoichiometry, the resultant particles are functionalised with only a small number of ligands localised in one area of the monolayer. Another way in which a particle can be anisotropically coated is by using an interface, otherwise known as the Langmuir method. The asymmetric environment of an air/water interface can be used as a template where hydrophilic ligands can be exchanged into a hydrophobic monolayer at the interface, or *vice versa*. A study by Chen and co-workers uses this Langmuir method under relatively high surface pressures to introduce hydrophilic ligands onto a hydrophobic alkanethiol-capped nanoparticle, when the ligands are injected into the water subphase [73]. This gave the resultant particles amphiphilic properties. The formation of amphiphilic nanoparticles was also seen by Norgaard and co-workers [74], where hydrophilic ligands were observed to organise and segregate themselves in order to minimise contact with the hydrophobic solvent. Here, it could be suggested that, hydrophobicity/hydrophilicity was the driver for the

self-organisation of the monolayer rather than the interactions of the ligands with each other.

Rosi and co-workers have focused on using peptide assemblies to produce a 1D scaffold and controlling the particle size and density [75]. The peptide forms a large 1-D structure along which particles are seeded at specific locations and grown, all from the peptide alpha helices. The peptide scaffold's secondary structure can be controlled to direct the self-assembly of the nanoparticles into several different structures, each having different effects on inter particle spacing and the number of particles along an assembly.

The ability to control the surface stoichiometry and the precise relative position of ligands could allow us to produce materials, and pave the way to producing materials that selectively self-assemble into nanomachines to perform complex tasks. To date there is evidence for different approaches for the self-organisation of ligands on the nanoparticle surface, from bottom up techniques where differences in ligand structures drives their segregation, to what could be considered top down where the ligands can be introduced using templates or lithography. A hierarchy of self-assembly, however, has yet to be established to fully exploit each of these processes.

While the controlled formation of nanometre-sized functional domains on nanoparticle still represents a major challenge, some general trends are emerging from the literature. Mobility of ligands appear to be limited [76] in most cases which may constitute a strong limitation to

the "templatable" approach [40]. On the other hand, this limited mobility provides a mechanism to freeze structures which have been obtained during the formation of the monolayer where anisotropy, patchiness, and self-organisation can occur due to the balance between ligand(s)-solvent, ligand(s)-surface and ligand-ligand interactions [12,19,30]. The latter process can be guided using templates [36] which are either surfaces of functionalised microscopic beads [72] or macromolecules [35]. A key issue in the field remains the difficulty in directly characterising the formed structures as opposed to indirect study of nanostructures formed from those building blocks. Efforts in the area of spectroscopy are needed to overcome these limitations and help towards rational design of structured nanoparticles. Computer modelling is currently in advance on the experimentation and constitutes an inspiration for materials scientists together with the remarkable biological self-assembled systems.

1.7. Ligand removal and exchange

Self-assembled monolayers on gold nanoparticles can be studied not only by the characteristics of the monolayer in situ, but also by considering the removal of the ligands. Ligands on gold nanoparticles may be removed by both chemical means, in a process called ligand exchange[53] or by ultra-fast heating using light [77 78,79]. These processes can give information on how strongly the ligands are associated within the monolayer [63 80] and also how defect rich a monolayer is [81].

In this thesis we first closely examine a body of work previously published in the literature that reports the peculiar self-organisation of

ligands on the surfaces of gold nanoparticles into stripy domains based on scanning tunnelling microscopy. The published data is subjected to image analysis techniques, and compared to a theoretical model system, both of which suggest that the proposed interpretation of the images is not valid. We then try to evaluate some of the claims regarding the physicochemical properties of those particles, including a stability study to indicate the saturation point in organic solvent, measuring the amount of non-specific binding to a charged protein, and finally nanoparticle entry into cells, leading to major discrepancy with published results.

The self-organisation of peptide ligands into structures on the surface of nanoparticles is an important step towards molecular engineering. We synthesise and characterise a peptide derived from a known amyloidogenic sequence, and compare it to the peptide sequence CALNN using a combination of techniques normally used in structural biology. In addition, colloidal stability assays reveal differences in the behaviour of these peptide self-assembled monolayers. To our knowledge, this is the first such study of characterising gold nanoparticles capped with amyloidogenic peptides.
In the final section of this thesis, an application of femtochemistry looks at the reaction dynamics of laser-induced ligand desorption using fluorescence. Using a variable delay line it is possible to elucidate the reaction dynamics of the dissociation and propose a mechanism

CHAPTER 2

Stripy nanoparticles revisited

2.1 Introduction

High-resolution structural characterisation of nanoparticles remains a significant challenge. Most samples of nanoparticles are inherently heterogeneous and therefore unsuitable for X-ray crystallography, which has been used for decades to gain angstrom resolution of proteins and other biological macromolecules on a similar size range to ligand-capped nanoparticles. [82] Nanoparticles of a sufficiently small size have their diameters decided by stable numbers of gold atoms (magic numbers) forming closed geometric shells. This has enabled the first and only example of synthesis and sub-angstrom structural resolution of gold nanoparticles. There have been no documented examples of larger nanoparticles forming suitably high quality crystals for use in X-ray crystallography. Another method traditionally used to gain structural information on macromolecules is solution state NMR. Nanoparticles are large compared to the small biological macromolecules that are usually examined, and have such have much longer tumbling time. This will often result in a significant broadening of NMR peaks[83] especially as particle size increases, and consequently structural resolution is lost. Because we are unable to use these two structural analysis techniques new ways of elucidating the structure and ordering on the nanoscale are needed. The work carried out by Stellacci *et al.* represents an attempt to further

understand how molecules behave and self-organise on the nanoscale, but draws several conclusions which should be openly discussed in the scientific community due to their wide-reaching implications.

Jackson *et al.* published an article entitled "spontaneous assembly of subnanometre-ordered domains in the ligand shell of monolayer-protected nanoparticles" in May 2004.[59] This was to become the first of a series, which now consists of more than ten research articles.[59,84-95] Throughout this series the authors base their research on the existence of "stripy" domains on the surface of gold nanoparticles, where two different thiolated organic ligands self-organise into alternating stripes across the nanoparticle surface. Numerous unusual and exciting properties have been attributed to the nanoparticles bearing these striated domains. Stripy nanoparticles are described as being "extremely effective in avoiding non-specific adsorption of a variety of proteins"[59], having the ability to "penetrate the plasma membrane without bilayer disruption" [93] in cell experiments and having poles which are particularly reactive and can be preferentially targeted to obtain divalent nanoparticles.[86] This series of articles, and the corresponding structure-property relationships reported, are important due to their direct impact on our understanding of several of the key problems in the field of nanoscience. The latter include the characterisation of materials with sub-nanometre resolution,[96] the possibility of controlling the self-organisation of ligands on gold nanoparticles,[32,36,97] the understanding of nanoparticle-biomolecule and nanoparticle-cell interactions[98] and the intracellular delivery of nanoparticles.[80,99-101] This proposed stripy structure is based on

Scanning Tunneling Microscopy (STM) observations, which to date have not been reproduced by any other research group. After carefully following the published articles we failed to observe or substantiate a number of claims made about their physical and chemical properties.

2.2 A geometrical problem

A STM topography image of a spherical particle is an approximate 2D projection of the top hemisphere. If a spherical particle is covered with stripes regularly spaced on its surface, this will not result in a 2D projection with the same inter stripe distances. For example, a 5.8 nm diameter sphere with 9 regularly spaced 1 nm wide stripes, the apparent width of the stripes decreases as the STM tip moves away from the center of the observed hemisphere, towards its edge, perpendicularly to the stripe direction (Figure 2.1a) and b)). An exemplary STM of a mercaptoproprionic acid and octanethiol-capped nanoparticle is shown in figure 2.1c) (adapted from Jackson *et al.* [59]). The authors measured, by TEM, the diameter of the gold core as 3.8 nm. The thickness of the monolayer was ~1 nm and, according to the authors, the stripe periodicity was 1 nm (table 1, supporting information, Jackson *et al.*). The simple geometric model therefore applies (3.8 nm particle diameter + 2 x 1 nm, monolayer thickness, giving a 5.8 nm diameter sphere with a 1 nm periodicity) and a dependence of the apparent stripe width in the STM image is expected (1 nm, 0.9 nm, 0.6 nm and 0.3 nm from the center of the hemisphere to the edge). This same trend is not what Jackson *et al.*

report: experimentally, the apparent stripe width does not decrease as the tip is moving away from the top of the hemisphere (Figure 2.1c) bottom). This discrepancy between the geometrical prediction and the observed experimental results cannot be explained by size polydispersity or a small error in particle sizing. For a particle 20% larger the geometrical effect would be equally apparent (having a spacing of 1 nm, 0.9 nm, 0.8 nm, 0.6 nm, 0.4 nm and 0.1 nm from the hemisphere center to the edge). The interpretation of the Jackson *et al.* STM images as indicating the presence of regularly spaced stripes on the nanoparticles conflicts with geometry since if the stripes are regularly spaced in 3-D they cannot be equally spaced in their 2D projection. Another distinctive characteristic of the stripes is that they are all aligned perpendicularly to the scanning direction. Initially Jackson *et al.* claim that this alignment is due to interdigitation between nanoparticles. This was based on data (not shown in the article) indicating a loss of this alignment when the sample it prepared above the interdigitation temperature. [59] In a later article published in 2008 Hu *et al.* again make the same claim, asserting that this interdigitation is key in directing the interactions between stripy nanoparticles. [91] The same group claim, in a subsequent article later the same year, that "*because of the charges present in the ligand shell, we can assume that the amount of interdigitation is negligible. We confirmed this using differential scanning colorimetery according to methods in the literature*". [89] Whilst interdigitation could explain some degree of correlation between nanoparticles in direct contact, it

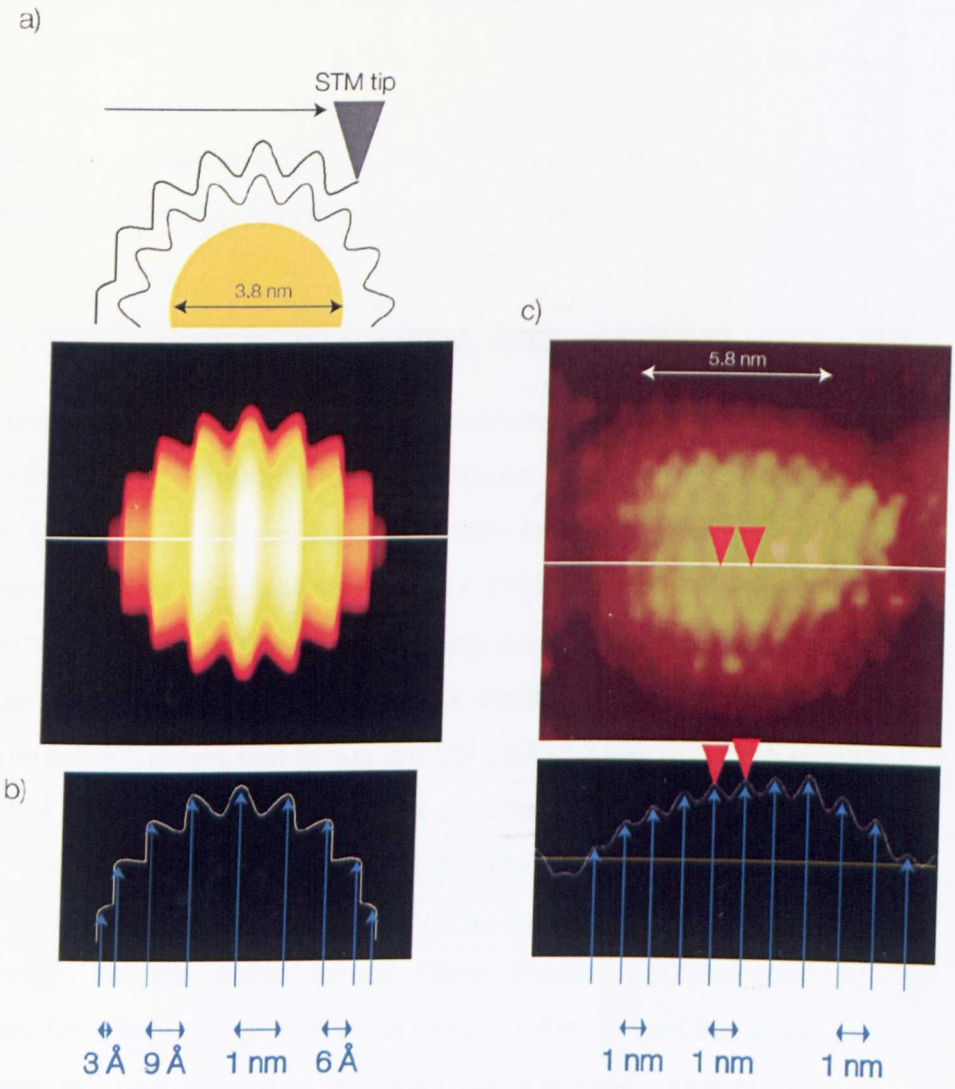

Figure 2.1. Comparison of the predicted and report stripe widths on a 5.8 nm diameter gold nanoparticle, a) (top) STM tip scanning a stripy nanoparticle orientated perpendicularly to the scanning direction, and (bottom) resulting STM image with colour coding depicting sample heights, b) Height profile corresponding to the white line drawn in a) bottom and stripe widths decreasing as the STM tip moves away from the center of the hemisphere, c) (top) Exemplary STM image (adapted from figure 1b of Jackson *et al.* [59]) (bottom) height profile corresponding to the white line in above image (adapted from figure 1d of Jackson *et al.* [59]) showing stripe

width not decreasing as the tip moves away from the center of the hemisphere.

does not explain why nanoparticles separated by gaps and several other nanoparticles are still in perfect alignment.

2.3 Evidence for stripes in STM, XRD and TEM?

Jackson *et al.* explained that the stripes could only be visualised when the stripes are perpendicular to the stripes because of convolution of the STM tip. Whilst this argument may explain why no stripes are seen parallel to the scanning direction, it does not explain why stripes that are 80° or 110° to the scanning axis are not observed. This argument, just as the previous, fails to explain why the orientations of nanoparticles in any one image are still perfectly aligned. If the stripes on the nanoparticles could only be detected if they are within ±5° of the perpendicular of the scanning direction, detecting a stripy nanoparticle would be a relatively rare event, where only one in eighteen images would exhibit these stripes. If there were no interactions between particles due to interdigitation then this would be further reduced to one in eighteen nanoparticles. Jackson *et al.*, however state that stripes were systematically observed: "*First, the imaging was performed on particles synthesised on separate occasions; each particle batch was cast on different substrates and imaged with multiple tips on various days over a period of months. The resulting images all showed the same rippled nanoparticles with a variation in the peak-to-peak spacing of less then 10%.*" [59]

As further evidence Jackson *et al.* indicate that the existence of the stripes is confirmed by X-ray diffraction (XRD): "*Indeed, all of the XRD plots of the rippled nanoparticles described in this paper showed peaks at 2θ ranging from 2.5° to 13°. Some of the peaks were temperature dependent, as is expected for peaks due to inter-particle packing arrangements.*[5] *However, one or two peaks were temperature independent, pointing to periodic arrangements, with 0.5–2.5 nm spacing, on single nanoparticles (see Supplementary Information, Fig. S1). Such temperature-independent peaks were never observed in homo-ligand nanoparticles.*" [59] The published XRD results are of three curves corresponding to two samples, and does not include the 67 % OT, 33 % MPA nanoparticles that were analysed by STM, which are claimed to exhibit stripe domains. Unfortunately no XRD data is given for nanoparticles that are claimed to not be stripy, therefore rendering any comparison impossible. Within the XRD data there are a number of peaks that are not assigned, and the presence of "temperature-independent" peaks is not proof of stripes.

Jackson *et al.* also claim that TEM data confirms the presence of stripes: "*Additional confirmation of the presence of ordered phase-separated domains was provided by transmission electron microscopy (TEM) images. In fact, in these images (see Supplementary Information, Fig. S2) we have found that there is an observable ring around the nanoparticles' metallic cores consisting of discrete dots spaced ~0.5–0.6 nm.*" The results that were published were only of one high-resolution TEM. The observed discrete dots,

attributed to ions bound to the stripes, are not easily visible due to variations of contrast due to the carbon coating of the grids. Using TEM to gain this kind of structural information has recently been demonstrated in the case of the formation of polyoxometalates (POM) SAMs. These POM ligands are based on tungsten oxide and, contrary to the purely organic ligands used by Jackson *et al.*, POMs have a high electron density providing EM contrast [19]. From the single TEM micrograph of Jackson et al, no solid conclusions can be drawn.

2.4 Fast Fourier image analysis of STM images

The dependence of the stripe periodicity on experimental factors including scanning speed [84,94] and preparative factors such as monolayer composition [59] and the stripe dependency on these has been the focus of several articles in the series. Direct measurement of the stripe width on a STM image was used but this can introduce bias and experimental errors. Fast Fourier Transform (FFT) power spectra images can be used to analyse regular patterns in noisy or imperfect images. A FFT power spectrum of a perfect sinusoidal stripy image will show two spots and the position and orientation of these two peaks is characteristic of the orientation and periodicity of the stripes, while an image with defects and different stripe orientations will show arcs, the length of the arcs show the difference in orientation and the intensity is indicative of the preferred alignment of any periodic features. [102]

Figure 2.2a shows a STM image adapted from Jackson *et al.* [59] The FFT of this image shows two vertical maxima corresponding to the stripes in the image (Figure 2.2b). As shown in the intensity profile, the periodicity measured along the x-axis is 1.3 ± 0.5 nm, instead of the 0.9 ± 0.1 nm or 1 nm originally reported by Jackson *et al.* [59] Most importantly however, is that the shape of these maxima in the FFT image is elongated and exactly aligned with the y-axis. Two vertical lines are seen going through these maxima. In a FFT image a vertical line represents a series of modes that have exactly the same periodicity along the x-axis, but different periodicity along the y-axis i.e. different wavelengths. Such modes cannot possibly be related to physical features in the sample because they have a defined wavelength along the fast scanning axis, λ_x, but no defined wavelength along the slow scanning axis, λ_y, and therefore no overall wavelength. For comparison, a theoretical model of stripy nanoparticles and it's FFT are presented (Figure 2.2d) and e)). This image was generated by using the same nanoparticle image several times, each copy being rotated between -5 and +5 degrees. Despite the near perfect alignment of the theoretical stripy particles, the maxima are still semi-circular which can be clearly seen and the wavelength of the corresponding modes is ~0.9 nm.

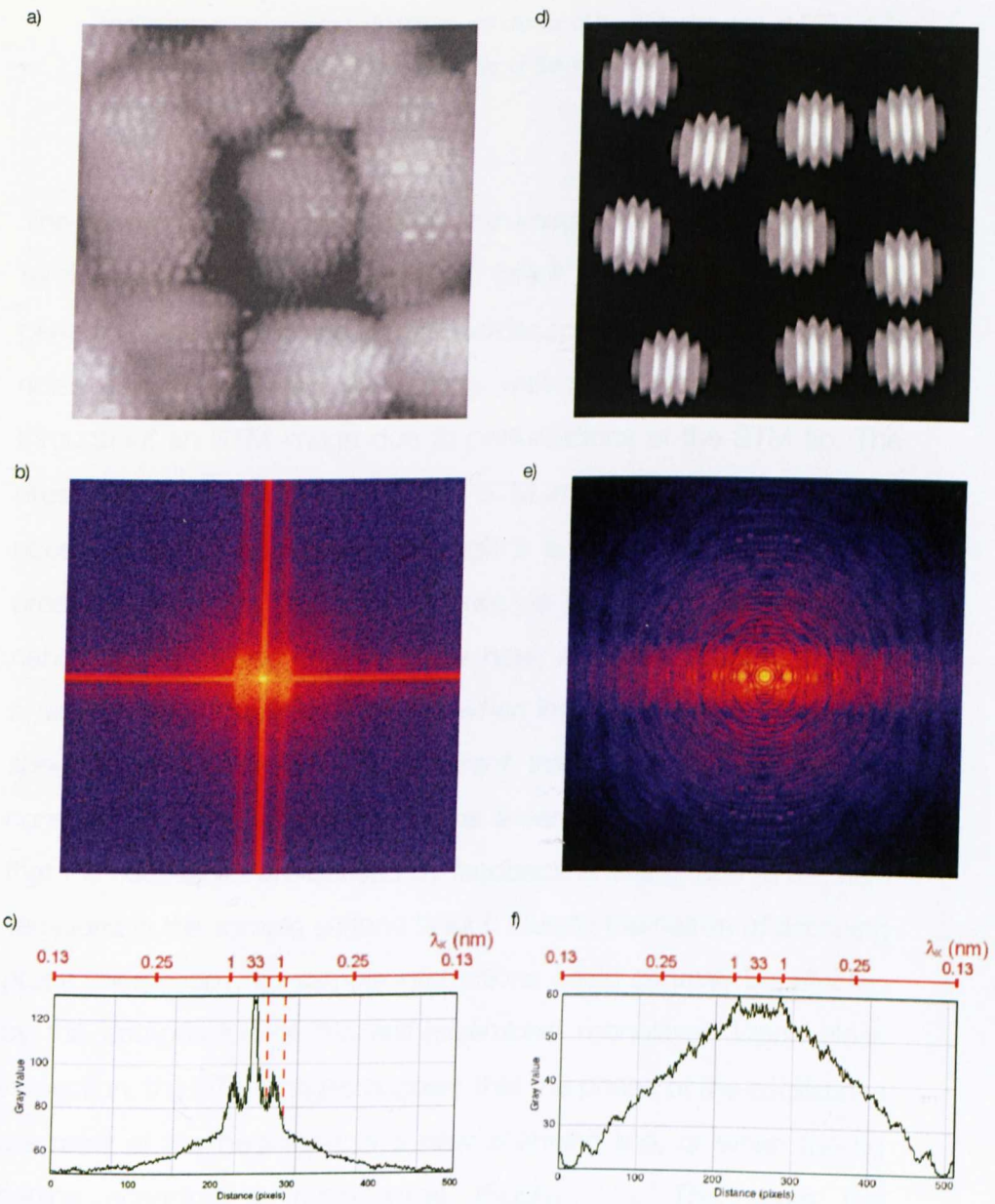

Figure 2.2. Comparison of image analyses of published experimental and model results; a) Experimental STM image (adapted from Jackson *et al.* [59]), b) FFT of image displayed in a), c) Intensity profile of the whole FFT image averaged along the y-axis, d) Theoretical image of 10 stripy nanoparticles

each rotated each rotated ±5° the perpendicular of the scanning axis, e) FFT of theoretical image d), f) Intensity profile of the entire FFT image averaged along the y-axis.

The stripy patterns observed in the images of Jackson *et al.* are reminiscent of feedback artefacts, which generate high frequency periodic noise in scanning probe microscopy images. [103] This periodic noise can be localised to features with steep slopes or be seen throughout an STM image due to perturbations of the STM tip. The presence of oscillatory noise in the STM images by Jackson *et al.* is accepted in the publication although it is argued that the noise is present on the flat substrate but not on the steep features of the nanoparticles *"These images show how, at times, ripples can look similar to noise in our images, but when images taken at different tip speeds are compared, it is apparent that ripple spacing remains constant while noise spacing scales linearly with speed"*. It is likely that the oscillations are caused by feedback artefacts due to the high variations in the sample surface height. Due to the nature of scanning probe microscopy, tip-sample interactions could certainly be affected by the composition of the self-assembled monolayer. Upon close inspection, the STM images suggest that the phase of the oscillations are reset at the beginning of a new scanning line, or when the tip begins scanning a nanoparticle (Figure 2.3). This gives the appearance of the stripes being shifted along the x-axis. These phase shifts between consecutive scanning lines is present in all of the published STM images of "stripy nanoparticles". Such shifts are even more evident if a band pass frequency filter is applied to the image (Figure 2.3c). This band pass filter works by removing information

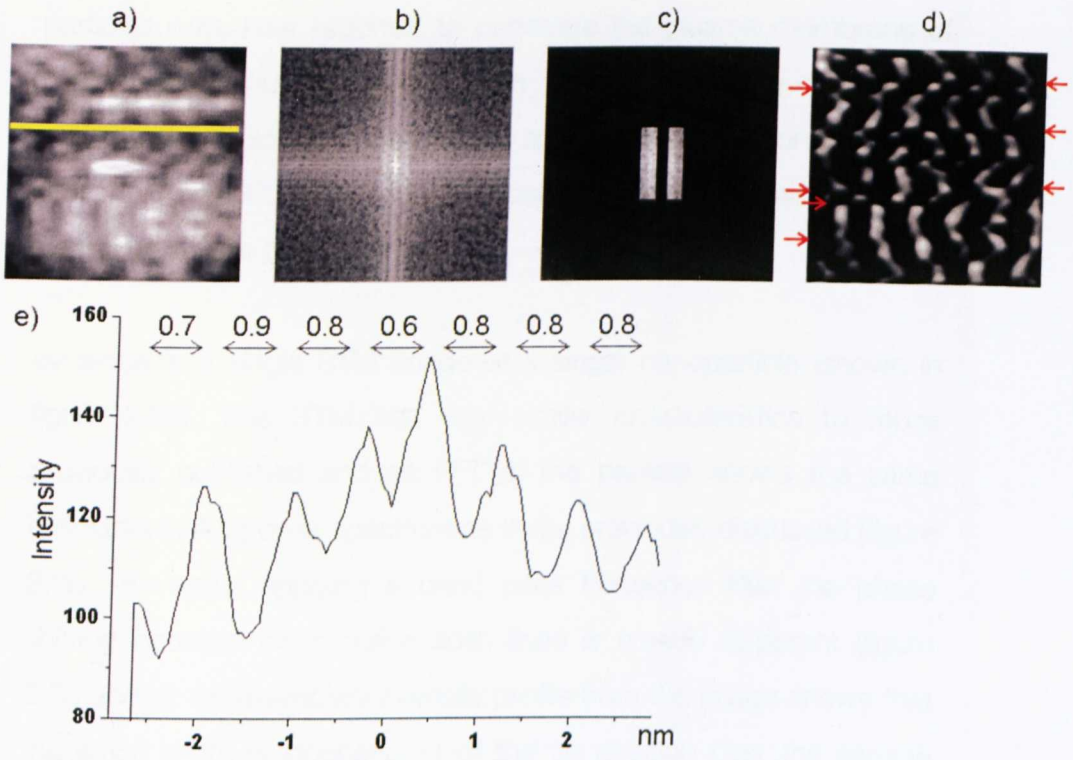

Figure 2.3. Image analysis of water-soluble 67 % MUS – 33 % OT gold nanoparticles; a) Published STM image of a water-soluble MUS/OT nanoparticle (adapted from Uzun *et al.* [92]), b) FFT of the STM image in a), c) Frequency filter applied to FFT image, d) reverse FFT of c) showing phase shifts between consecutive scanning lines (marked by red arrows), e) Intensity profile corresponding to the yellow line in a).

from the image that is a higher or lower frequency than the observed stripes.

In 2008, Uzun *et al.* reported on the synthesis of water-soluble "stripy" nanoparticles. [92] This time the monolayer composition was a mix of 11-mercaptoundecanesulfonate (MUS) and octanethiol (OT). Again, the stripes were only visible when certain compositions were used, namely a molar ratio of 2:1 of MUS:OT or OT:MUS. These same

particles were later reported to penetrate the plasma membrane of living cells without bilayer disruption and without being confined to endosomes. [93] Both of these articles are primarily based on the notion that the MUS/OT-capped nanoparticles exhibit these "stripy" domains, yet the only published

evidence is a single STM image of a single nanoparticle (shown in figure 2.3a). This STM has very similar characteristics to those previously published and an FFT of the particle shows the same hallmarks in the power spectrum as those previously discussed (figure 2.3b). By again applying a band pass frequency filter the phase shifting between consecutive scan lines is equally apparent (figure 2.3c and d). An exemplary intensity profile from the image shows that the stripe width is independent of the tip position over the sample (figure 2.3e). The FFT of this published image shows that this STM image cannot be that of a 2D representation of a spherical nanoparticle capped with regularly spaced stripe domains, and the stripes cannot correspond to physical attributes of the sample.

Stellacci and co-workers attribute some unusual physicochemical properties to the "stripy" nanoparticles to the nanoscale organisation of the ligands into striated domains. As the monolayer composition is changed the nanoparticles are claimed to exhibit non-linear; solubility profiles in various solvents, [59,89] binding interactions with proteins[59,93] and uptake of nanoparticles by live cells. [93] We attempted to repeat some of the results published, but upon close scrutiny there are

inconsistencies amongst the data published between different articles, and also our own sets of experiments.

Jackson *et al.* report on the dependence of nanoparticle "solubility" in ethanol is non-monotonous as the monolayer composition changes. [59] This is measured by a purely visual observation, the observer scoring the sample on a scale of one to four. More quantitative data is presented by Centrone *et al.* were the authors test the stability of nanoparticle suspensions with different ligand ratios in various solvents. [89] In both Jackson *et al.* and Centrone *et al.* measurements taken on the same system of gold particles capped with mixtures of MPA and OT are shown. The two papers give contradictory results (figure 2.4) and the origin of this discrepancy is not discussed in the more recent Centrone *et al.* manuscript. [89] The latter article is based on measuring the concentration of particles capped with various ratios of MPA and OT in the nanoparticle monolayers. The saturation concentration of nanoparticles capped with 100 % OT is given as ~400 nM in five different solvents i.e. benzene, tetrahydrofuran, hexane, dichlorobenzene and chloroform. The concentration of ~400 nM seems to be the saturation and none of the nanoparticles have a saturation concentration of more than 470 nM in any solvent. This is unusual not only because the solvent-nanoparticle interfacial energy vary significantly between these different solvents but also because saturation concentrations of around 400 nM are remarkably low for a colloid in

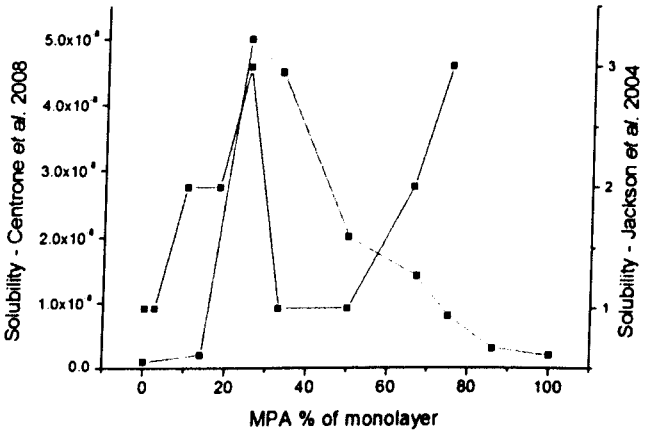

Figure 2.4. Comparison between the results published by Centrone *et al.* [89] (black data points, left y-axis) and Jackson *et al.* [59] (blue data points, right y-axis) for the effect of monolayer composition on the colloidal stability in ethanol. Centrone *et al.* measured the concentration of the colloid using an extinction coefficient expressing the saturation concentration in molarity. Jackson *et al.* used a solubility scale as follows; , *"4 = highly soluble, that is, no precipitation visually observed, 3 = mostly soluble, that is, little precipitation observed over time with consequent slight decolouration of the solution; 2 = slightly soluble, that is, most of sample precipitated but a small coloration of the solution remains, 1 = totally insoluble."*.

a good solvent. This low concentration, for a 6 nm diameter, equates to a volume fraction of 0.0027% at 400 nM. For colloids in a good solvent, volume fractions of 30 % are routinely obtained, and the absolute physical limit is the close packing of the particles. We repeated the Centrone *et al.* experiment with nanoparticles capped with 100 % OT, as described in the article, and suspended them in

100 % THF. Following the same procedure as Centrone *et al.*, and using the same extinction co-efficient, we have been unable to measure any change in an equilibrium between solid and liquid phases even after three weeks, the nanoparticles remained in suspension (Figure 2.5). We can therefore state that nanoparticles capped with 100 % OT have a saturation concentration higher than 8 μM, i.e. over 18 times higher than that reported by Centrone *et al.*

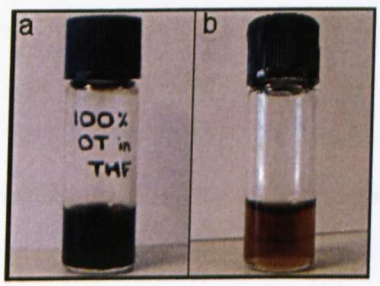

Figure 2.5. Comparing two suspensions of OT-capped gold nanoparticles; a) 8 μM OT nanoparticles in THF after three weeks, b) A 450 nM suspension of the same OT particles in THF, described by Centrone *et al.* as the saturation limit.

2.5 Non-specific binding

Both Jackson *et al.* and Verma *et al.* claim that due to the small spacing of the alternating hydrophilic/hydrophobic stripes, the adsorption of proteins is hindered because the stripes are smaller than the typical size of features on a protein, giving these charged nanoparticles excellent antifouling properties. Whilst this claim is referenced in other papers the only evidence submitted to substantiate this claim by Jackson et al is a cartoon of a stripy nanoparticle and protein. No experimental data is shown. This claim is

unusual because molecules that have very low non-specific binding are usually neutral and hydrophilic whereas these nanoparticles have both hydrophobic and negative charges (due to respectively the sulfonate, Verma *et al*, and carboxylic acid groups, Jackson *et al*). The archetypal approach to preventing non-specific binding on surfaces is to use polyethylene glycol. This has been used to passivate nanoparticles[20 63] and surfaces [104-107]. The negative charge of the MUS ligand should attract and bind any positively charged groups in the same solution. To test this hypothesis nanoparticles were prepared as described by Verma *et al.* with the same monolayer compositions; 100 % MUS, 67 % MUS – 33 % OT, 33 % MUS – 67 % OT (figure 2.6). These nanoparticles were added to increasing amounts of lysozyme, a positively charged enzyme [108] due to its multiple Lysine and Arginine residues. This highly positively charged protein should readily bind to the negatively charged nanoparticles. All of the nanoparticles exposed to the lysozyme exhibited non-specific binding with the Lysozyme and aggregated (figure 2.7.). Nanoparticles capped with 100 % MUS exhibited the most resistance to the non-specific binding. This result could be due to the increase in hydrophobic ligands leading to interaction with hydrophobic domains of the lysozyme.

2.6 Cell entry of stripy nanoparticles

Verma *et al.* report that the nanoparticles capped with a precise ratio of mercaptoundecane sulfonate (MUS) and octane thiol (OT) are able

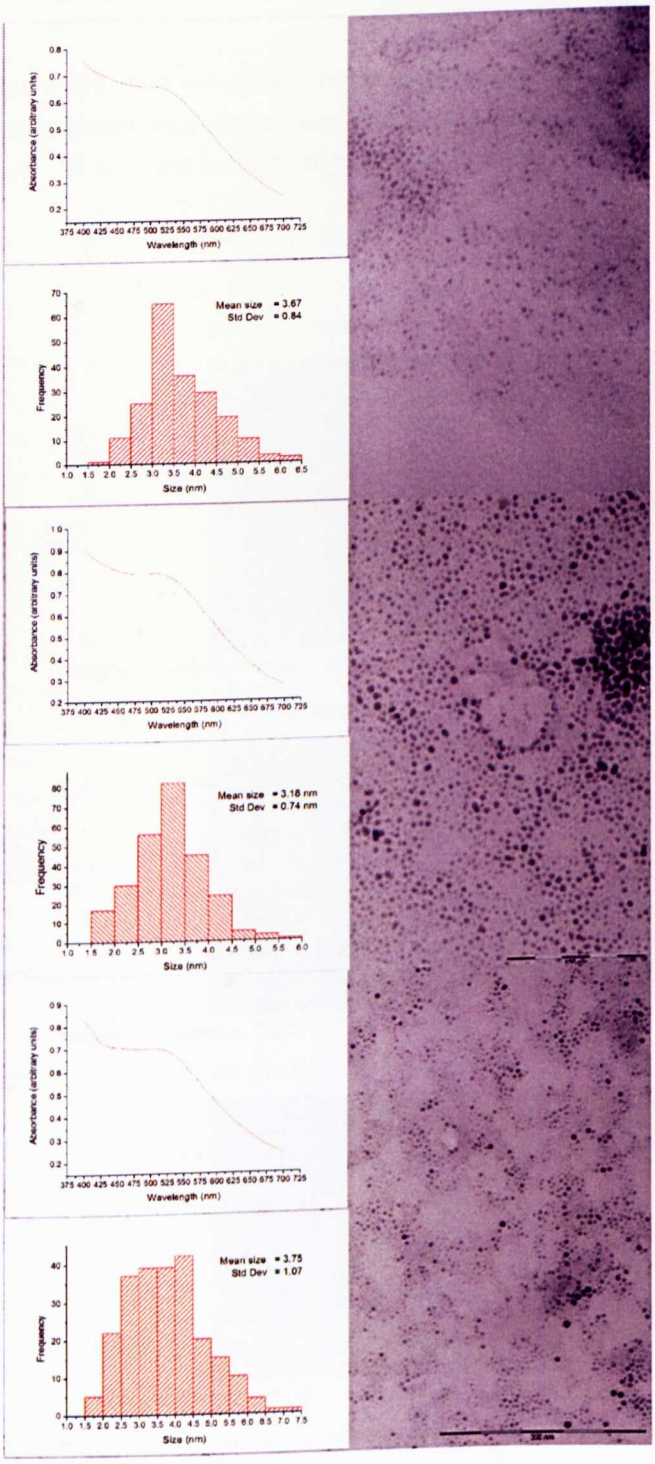
Absorbance (arbitrary units)
Wavelength (nm)
Frequency
Mean size = 3.67
Std Dev = 0.84
Size (nm)
Absorbance (arbitrary units)
Wavelength (nm)
Frequency
Mean size = 3.18 nm
Std Dev = 0.74 nm
Size (nm)
Absorbance (arbitrary units)
Wavelength (nm)
Frequency
Mean size = 3.75
Std Dev = 1.07
Size (nm)

Figure 2.6. TEM micrograph, UV-visible absorbance spectrum and nanoparticle size distribution from TEM analysis of (top) 33 % MUS - 67 % OT, (middle) 67 % MUS – 33 % OT and (bottom) 100 % MUS nanoparticles.

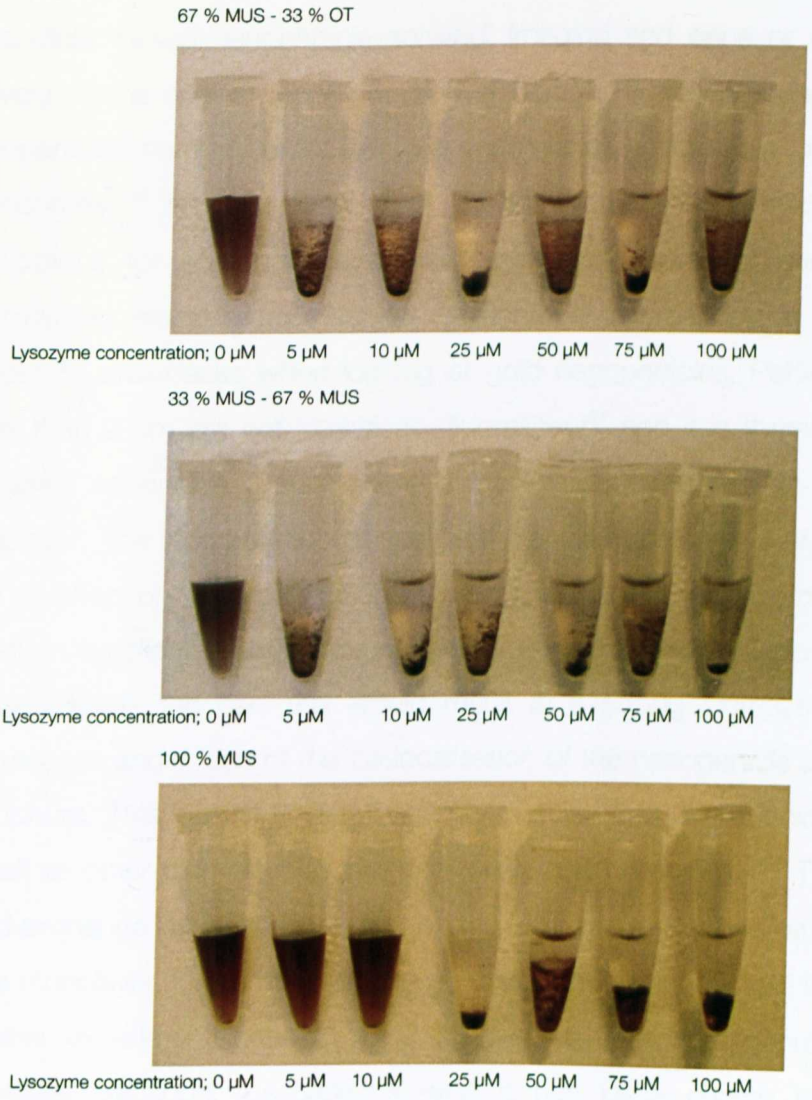

Figure 2.7. Non-specific binding assay of MUS/OT nanoparticles; (top) 33 % MUS – 67 % OT, (middle) 66 % MUS – 33 % OT, (bottom) 100 % MUS, mixed with lysozyme at 0 μM, 5 μM, 10 μM , 25 μM, 50 μM, 75 μM, 100 μM

and left at room temperature for one hour. Aggregation can be seen as precipitate.

to cross the cell membrane of living cells, gaining access to the cytosol. This is an extremely interesting observation because intracellular based nanoparticle sensing, imaging and gene or drug delivery. In the original report the largest portion of evidence comes nanoparticles normally enter cells via endocytosis and remain in the endosomes. [80] An observation such as this would have immediate applications for confocal microscopy work, with some additional transmission electron microscopy. [93] Confocal microscopy is not without its drawbacks when looking at gold nanoparticles. Particles larger than 2 nm are not intrinsically fluorescent[21] and it is therefore necessary to include a fluorescently labelled ligand as part of the monolayer. The incorporation of such a molecule is not only likely to have an effect on the organisation of the monolayer but the gold core is also an excellent fluorescence quencher. If the fluorescent ligand is released inside the cell, this would result in a strong increase of fluorescence and a loss of the co-localisation of the nanoparticle and fluorophore. This loss of thiolated ligands in cells, due to glutathione as well as other biomolecules has previously been reported. [109] This ligand exchange is highly dependent on the structure and organisation of the monolayer. [53] Verma *et al.* use an uncommon dendritic cell line in these experiments named DC2.4. This cell line has peculiar intracellular transport mechanisms, and it has been shown that exogenous antigens added to DC2.4 cells accumulate in the endoplasmic reticulum and late endosomes, followed by transport to

the cytoplasm. [110] Taking into account the factors affecting the fluorescence and the unusual behaviour of the cell line makes the interpretation of the published data difficult. Verma *et al.* also go on to claim that these MUS/OT nanoparticles are able to penetrate the cell membranes of other cells, including mouse embryonic fibroblasts, but for this the only evidence is four confocal fluorescent images each of one cell, one image for each of the four monolayer compositions they look at.

In order to simplify this process of nanoparticle uptake, and whether the MUS/OT capped nanoparticles do indeed access the cytoplasm, we looked at the delivery of MUS/OT nanoparticles in HeLa cells using photothermal microscopy. [80,111-113] The same nanoparticles used to assay the non-specific binding with lysozyme were used. Photothermal microscopy is based on the strong absorption cross-section of the gold core and is therefore immune to background scattering, but most importantly does not require additional molecular markers since it is the gold core itself is that is detected. This ultra sensitive method is able to detect single nanoparticles as small as 1.4 nm in diameter.[111] It is sensitive to the number and volume of nanoparticles in the laser spot. Salt-induced aggregation of the MUS/OT nanoparticles show that they have relatively poor colloidal stability. They have a tendency to aggregate at moderate ionic strength, and this tendency increases with the proportion of OT (figure 8). This observation is unsurprising since OT is a

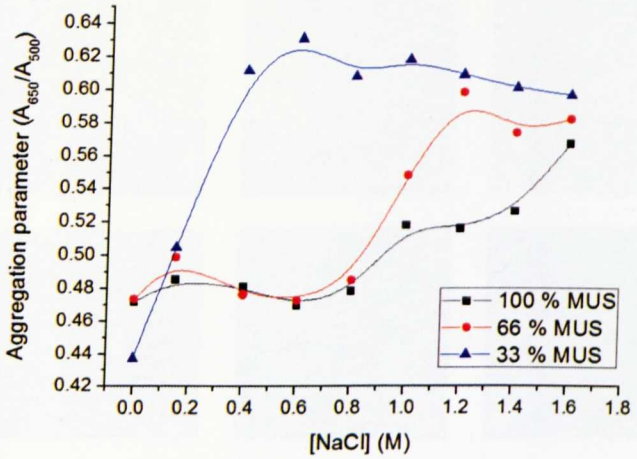

Figure 2.8. Salt-induced aggregation of MUS/OT nanoparticles; Aggregation is measured as the aggregation parameter. As nanoparticles aggregate the decrease in A_{λ} and increase at A_{λ} causes the A_{λ}:A_{λ} to increase and is indicative of the amount of aggregation taking place.

hydrophobic ligand and the salt-induced aggregation is performed in aqueous solution. Following the protocol outlined by Verma *et al.* the nanoparticles were mixed in fresh cell medium immediately before adding to the cells and incubated for three hours. They were then rinsed, fixed and imaged by photothermal and bright field microscopy (figure 2.9). As shown in figure 2.9, the cells provided very little background during this experiment. For all three nanoparticle types we observed an uptake that is characteristic of endocytosis. Importantly, there is no visible difference in localisation within the cells between the three types of nanoparticles. Photothermal microscopy has a very large dynamic range that is not easily represented on an image. In order to show the intensity contrast between the high intensity areas (endosomes) and the very low intensity areas

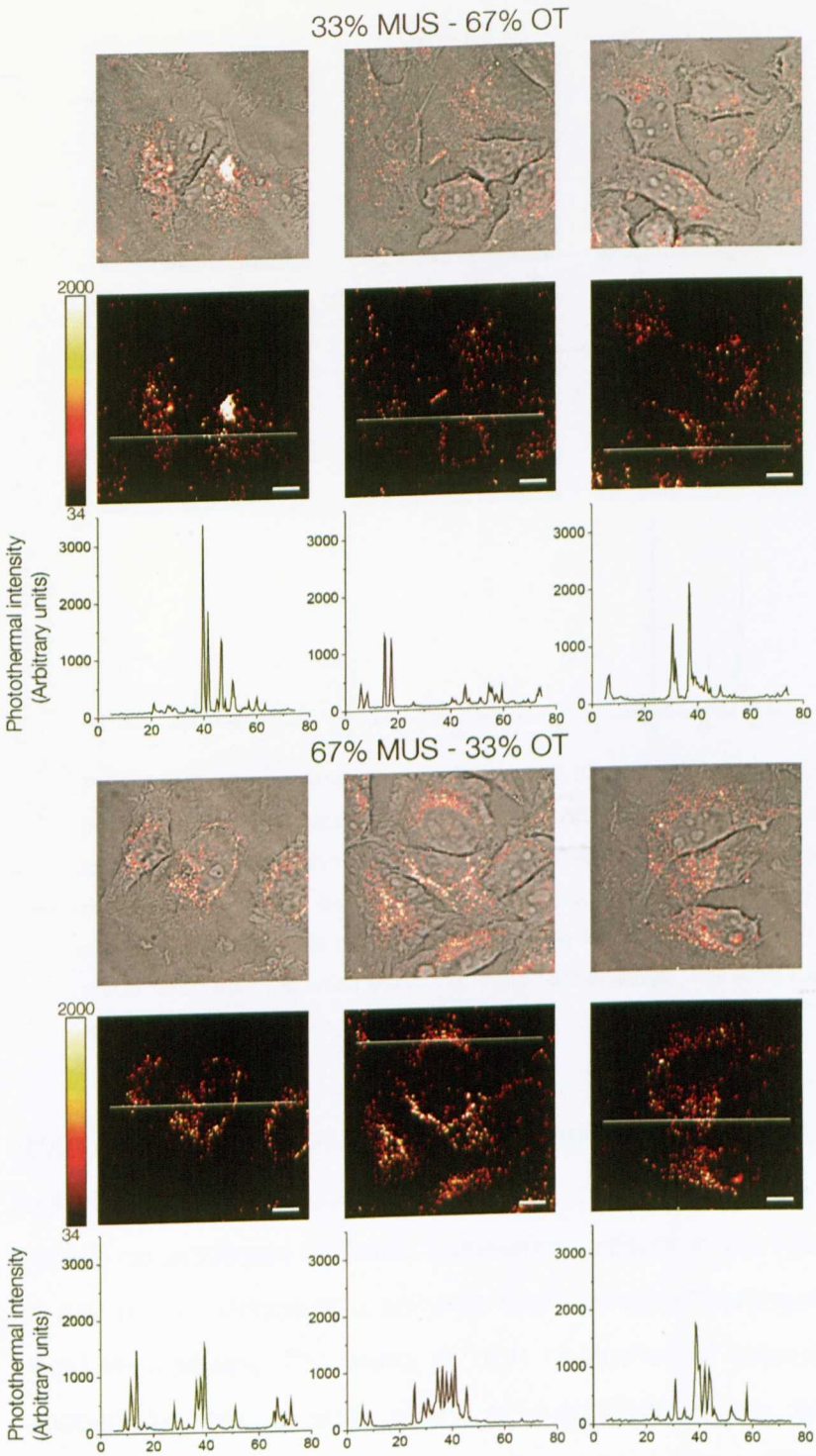
33% MUS - 67% OT
2000
34
Photothermal intensity
(Arbitrary units)
3000
2000
1000
0
0
20
40
60
80
67% MUS - 33% OT
2000
34
Photothermal intensity
(Arbitrary units)
3000
2000
1000
0
0
20
40
60
80

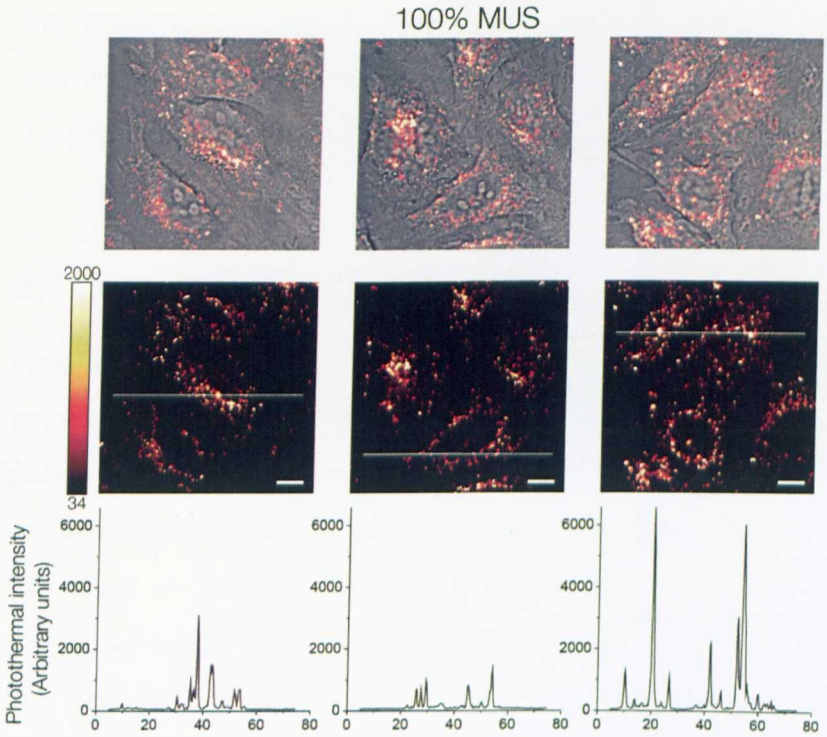

Figure 2.9. Cell internalization of (top panel) 33 % MUS – 67 % OT, (middle panel) 67 % MUS – 33 % OT and (bottom panel) 100 % MUS capped nanoparticles in HeLa cells. In each panel, the top images are an overlay of bright field and photothermal images, the center image is a photothermal image with the intensity scale to the left, at the bottom is a 1D profile taken from the white line in the photothermal image. The scale bars represent 10 μm.

(cytoplasm, nucleus and background), intensity profiles are shown for each image. The photothermal images unambiguously show that there is no significant cytosolic localisation present in the HeLa cells for any of the nanoparticle samples used, whether homogenous or mixed monolayers. The areas of high photothermal intensity from nanoparticles are several orders of magnitude higher than the background level. Because these results are based on a different cell

line, they are not in direct contradiction of those published, but rather they show clearly that the MUS/OT capped nanoparticles do not have the general property of crossing the cell membrane into the cytosol.

2.7 Conclusions

Here we have revisited the published evidence for the existence of stripe domains in mixed ligand monolayers on gold nanoparticles. The patterns seen in the various STM images cannot correspond to regularly spaced stripes at the surfaces of gold nanoparticles. This has been shown not only by the geometric argument, that if the stripes are equally spaced in 3D they cannot be equally spaced in 2D, but also that FFT shows that the stripes are indeed a scanning artefact. Whilst this work shows that the evidence for stripy domains is inconclusive, it does not rule out the existence of the self-organisation into domain structures in self-assembled monolayers, which is indeed part of the focus and motivation of this thesis. The saturation concentrations reported by Centrone *et al.* are not consistent with our own. The hydrophilic MUS/OT nanoparticles do not exhibit any unusual resistance to non-specific binding with lysozyme. Finally, we could not substantiate general claim that the MUS/OT nanoparticles are able to cross the cell membrane, after careful analysis using photothermal microscopy and HeLa cells. This instead indicated endosomal localisation regardless of monolayer composition.

CHAPTER 3

The structure of amyloidogenic and non-amyloidogenic peptides in self-assembled monolayers on gold nanoparticles

3.1 Inspiration from nature

In the past decade, a large and diverse array of water-soluble core-shell functional nanomaterials has been produced. Some of these have been described as "protein-like" but major differences remain between synthetic nanoparticles and proteins. Proteins are nanoscale objects where the exact position of each residue is critical to their function, e.g. specific recognition, catalysis. The precise spacial arrangement is obtained through the use of template mRNA for the primary structure and non-covalent interactions, self-assembly and self-organisation leading to the secondary, tertiary and quaternary structure. For these reasons proteins are a source of inspiration for the design and function of nanomaterials. The multifunctional core-shell nanomaterials obtained to date tend to have an uncontrolled, probably random, and often unknown structure at the molecular level and distribution on the nanoparticle surface. Designing, producing, and characterising nanomaterials which have an internal complexity analogous to proteins remains a long term goal in the field.[13]

Proteins exhibit primary, secondary, tertiary and quaternary structure and together they form the three-dimensional shape of the protein. In order to design and make nanoparticles with this level of complexity

an understanding of how peptides arrange on a surface is crucial. The primary structure of a protein, its sequence, contains all the information required for the folding of the higher order structures. Small peptides are ideal candidates for the design of self-assembling monolayers on gold nanoparticles. Using rational principles it is possible to design very stable dense peptide layers on nanoparticles and indirect insights on the intermolecular interactions in the peptide layer have been obtained [114] but the exact molecular structures of the peptides are unknown.

3.2 Peptide design and self assembly

In an attempt to induce local supramolecular ordering at the surface of a nanoparticle, we examine the effect of confining an amyloid fibril forming peptide on spherical gold particles of diameters from 5nm to 25nm. Several short peptides can assemble into amyloid-like fibrils with the characteristic cross-β structure (intermolecular hydrogen bonds approximately parallel to the fibril axis) that is the hallmark of larger protein fibrils associated with amyloid disease.[115] [116] Because of the specific intermolecular directional assembly, we envisioned that such peptides could constitute a category of new building blocks to engineer complex nanoparticles.

Modifications to the FGAIL sequence are known to produce peptides that form fibrillar aggregates, varying in morphologies. NFGAIL and FGAIL have been shown to assemble into completely different fibrillar assemblies [117] and NNFGAILSS can associate into both anti-parallel

and parallel β-sheet. [118] Instead of using the entire sequence NNFGAILSS, the two N-terminal asparagines were replaced by a cysteine, giving the sequence CFGAILSS. The thiol on the side chain of the cysteine allows stable binding to the gold

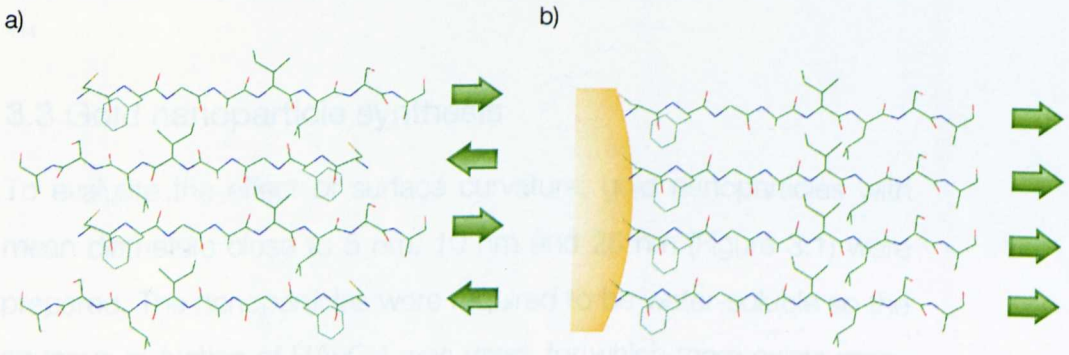

Scheme 3.1: a) CFGAILSS in fibrils containing anti parallel beta sheet b) CFGAILSS on a nanoparticle surface displaying a parallel beta sheet conformation. The arrows indicate the alignment of the peptides N to C terminal whilst in beta sheet formation.

nanoparticle. In the NNFGAILSS system, the register in which this peptide can associate into parallel β-sheet in fibrils is such that all amino acids are adjacent to the same residue in neighbouring peptides.[118] It is worth noting however that the amyloidogenic peptide sequence FGSVQ, derived from the protein Medin [119], did not form any amyloid fibrils in solution after the addition of an N-terminal a cysteine, making CFGSVQ. The peptide CALNN also does not form any visible aggregates or precipitate upon dissolving in aqueous medium.

Here, we use FTIR, 2DIR and ssNMR to compare the structure of amyloidogenic and non-amyloidogenic peptides on nanoparticles of different sizes. In particular we focus on the CFGAILSS peptide sequence derived from the human amyloid-forming protein amylin, and CALNN, a peptide rationally designed to stabilise nanoparticles. [114]

3.3 Gold nanoparticle synthesis

To evaluate the effect of surface curvature, gold nanoparticles with mean diameters close to 5 nm, 10 nm and 25 nm (Figure 3.1) were prepared. The nanoparticles were required to be water-soluble so the aqueous reduction of HAuCl4 was used, for which there exists many methods. Since no variations on a single method will provide particles in all of these three sizes with low polydispersity, two methods were used; tannic acid and acrylate reduction, adapted from citrate and tannic acid reduction [120], to form the 5 nm and 10 nm nanoparticles, and hydroxyl amine seeding [121] to form the larger 25 nm nanoparticles. Citrate, which is used in the most commonly used synthesis methods, has three carboxylic acid groups that absorb in the same region of the infrared spectrum as the characteristic amide I band, which is used to distinguish the secondary structure of peptides. Therefore the use of citrate was kept at a minimum.

The possibility of parallel β-sheet and adjacent registry make this peptide an interesting candidate for the design of supramolecular structures under the confinement of a self-assembled monolayer on a gold nanoparticle (Scheme 1). The modified peptide CFGAILSS, like

its parent peptide NNFGAILSS, forms extended fibrils in solution as shown by transmission electron

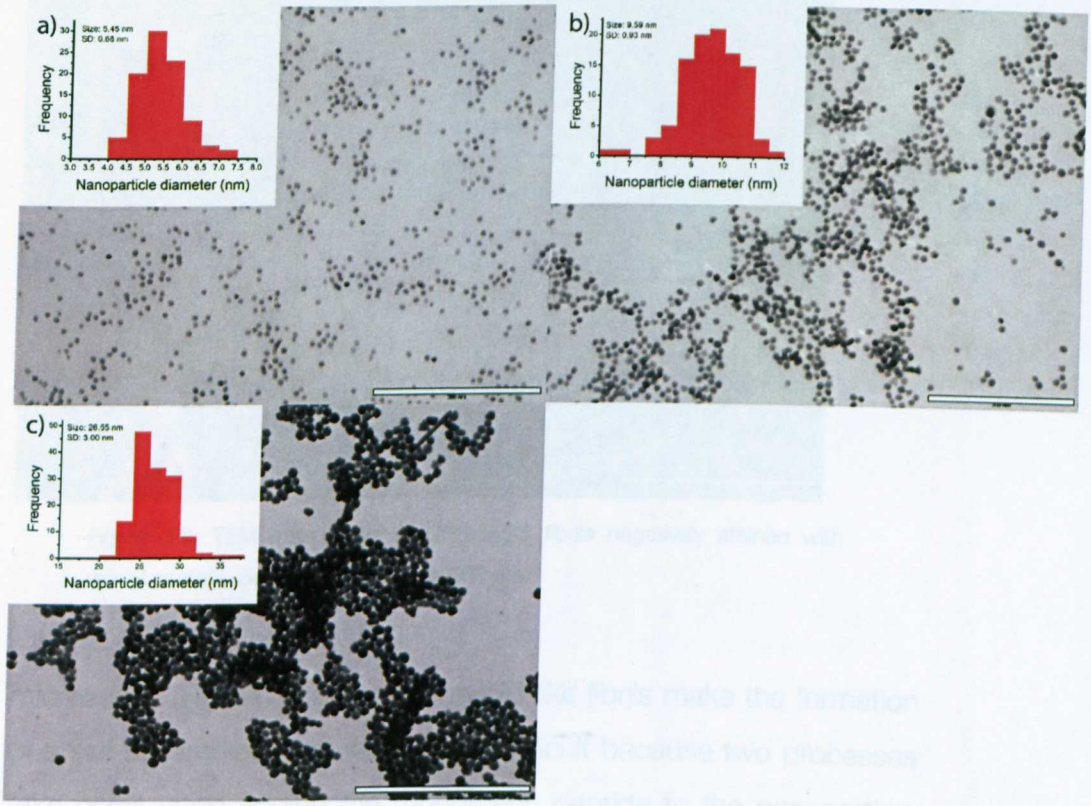

Figure 3.1. TEM and size distributions of; a) 5 nm, b) 10 nm and c) 25 nm gold nanoparticles synthesised for this work. In a and b scale bars represent 200 nm and in c, scale bar represents 500 nm.

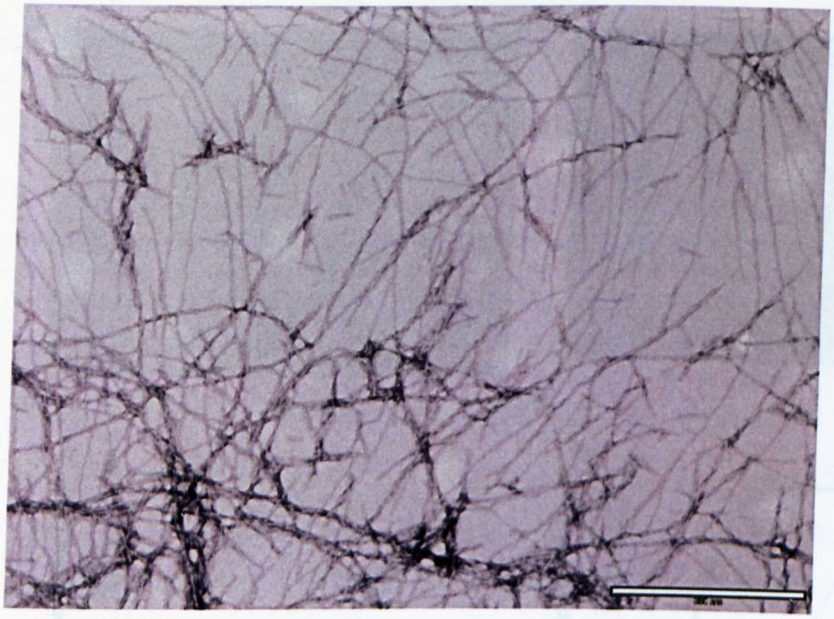

Figure 3.2. TEM micrograph of CFGAILSS fibrils negatively stained with uranyl acetate. Scale bar represents 500 nm.

microscopy (Figure 3.2). These amyloid-like fibrils make the formation of a self-assembled monolayer more difficult because two processes take place upon adding the monomeric peptide to the nanoparticle solution. The amine and cysteine from the N terminus of the peptide are attracted to the gold nanoparticle surface and begin to form a self-assembled monolayer. At the same time these peptides start to form insoluble fibrils reducing the concentration of peptide available to form the monolayer. The product of these processes is a mixture of fibrils, held together with hydrogen bonds, and the CFGAILSS peptide anchored to the gold surface through a covalent gold-thiol bond (Figure 3.3a).

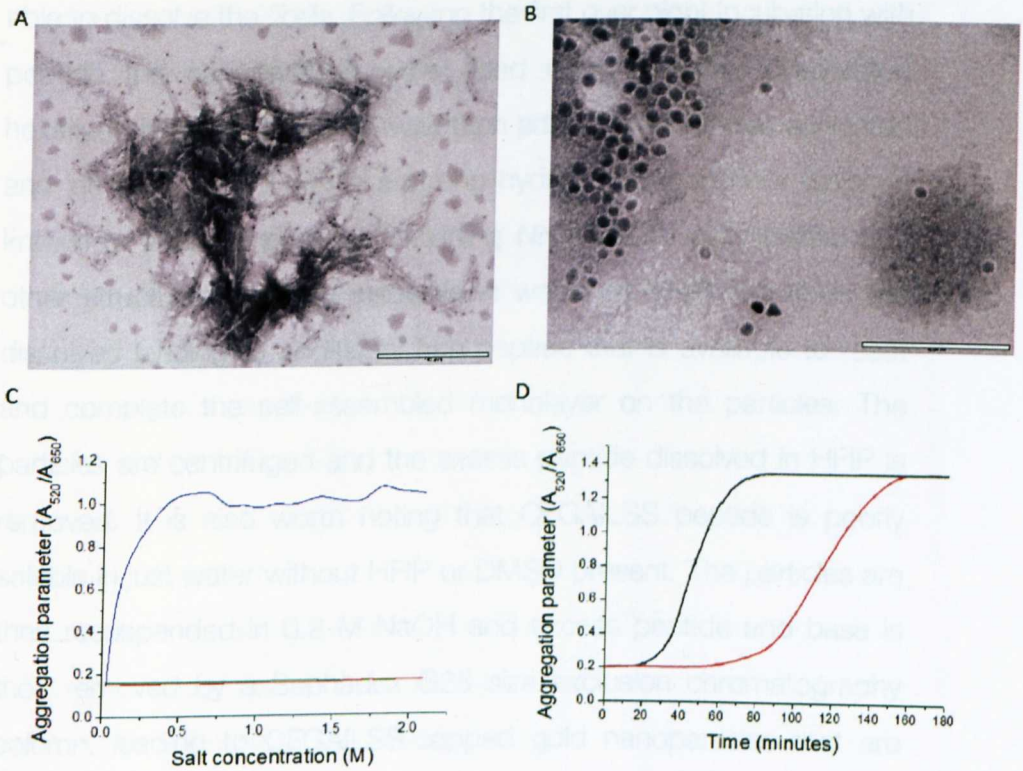

Figure 3.3. CFGAILSS, from fibrils to self-assembled monolayers; a) TEM of fibril-nanoparticle assembly formed during the first step of the capping process; b) TEM after completion of the capping process and removal of the excess peptide; c) stability against salt-induced aggregation of CALNN (red), CFGAILSS (green) and citrate-capped (blue) nanoparticles; d) stability against DTT ligand-exchange, salt-induced, aggregation of CALNN (black) and CFGAILSS (red) nanoparticles. In image a) the scale bar represents 500 nm, and in image b) the scale bar represents 100 nm.

In order to obtain nanoparticles capped with a dense layer of CFGAILSS, a protocol was developed to force the assembly on the nanoparticle surface of this peptide that will otherwise self-assemble into fibres [Chapter 6 -Materials and methods]. One aim was to control the concentration of free peptide available by using a solvent

able to dissolve the fibrils. Following the first over night incubation with peptide the nanoparticles were dried using a rotary evaporator, hexafluoroisopropanol (HFIP) was then added, the particles sonicated and left over night. HFIP is a strong hydrogen bond donor which is known to dissolve proteins, including NNFGAILSS aggregates, and other structures normally insoluble in water. In HFIP, the fibrils are dissolved leading to additional free peptide that is available to react and complete the self-assembled monolayer on the particles. The particles are centrifuged and the excess peptide dissolved in HFIP is removed. It is also worth noting that CFGAILSS peptide is poorly soluble in just water without HFIP or DMSO present. The particles are then resuspended in 0.2 M NaOH and excess peptide and base is then removed by a Sephadex G25 size exclusion chromatography column, leading to CFGAILSS-capped gold nanoparticles that are colloidally very stable in aqueous solutions. Most likely due to charge repulsion and steric hindrance, the peptides are unable to form anti-parallel β-sheet by the intercalation of peptides on two different nanoparticles. After removal of excess peptide the self-assembled monolayer can be visualised using TEM under negative stain (Figure 3.3b). To confirm the formation of the monolayer, the colloidal stability at high ionic strength was evaluated. Contrarily to uncapped nanoparticles, nanoparticles capped with CFGAILSS do not show any aggregation at all ionic strength tested (Figure 3.3c). The same results were obtained with CALNN-capped nanoparticles which is known to form a dense capping layer[114] Resistance to ligand exchange is a good indicator of the stability of a monolayer. To compare the resistance of monolayers to ligand exchange by dithiothreitol (DTT)

CALNN and CFGAILSS-capped 10 nm nanoparticles were treated with DTT. DTT is a small, uncharged molecule with two thiol groups. It ready exchanges with other ligands on the surfaces of gold nanoparticles. Since this small molecule is uncharged as it replaces the peptide monolayer it also removes the steric and electrostatic barrier that keeps the gold nanoparticles from aggregating. If this ligand exchange is done in the presence of salt it is possible to measure how quickly the peptide monolayer is replaced by measuring the extent of aggregation by the red shift in the plasmon band. Aggregation of CFGAILSS-capped nanoparticles induced by ligand exchange is more than two times slower than for CALNN-capped nanoparticles suggesting that CFGAILSS adopts a different structure in the self-assembled monolayer (Figure 3.3d). Amino acid analysis was conducted on a CFGAILSS capped 10 nm nanoparticle sample (Alta Bioscences, Birmingham). This revealed a packing density of 2.55 peptides/nm^2, i.e. higher than that of CALNN (2.4 peptides/nm^2).[63]

3.5 FTIR indicates the presence of secondary structure

Infrared spectroscopy is a routine technique used to analyse small molecules, proteins and peptides. IR light is absorbed by a molecule by interaction of electromagnetic waves with the dipole moment of a molecular vibration. If the frequencies of light and vibration are the same the electromagnetic wave couples with the dipole moment and the electric field will amplify the movement of the vibration. The units of frequency in FTIR are wavenumbers cm^{-1} ($1/\lambda$, the reciprocal of wavelength). Molecular vibrations are sensitive to their environment, and FTIR is therefore very sensitive to changes in the electron

distribution of any given vibrational mode that is affected by hydrogen bonding or conformational changes in the molecule. The backbone structure of proteins and peptides is very sensitive to the secondary structure that the molecule adopts. These changes can be seen in the two carbonyl IR absorption bands, the amide I and the amide II bands [122,123]. The Amide I band (around ~1650 cm^{-1}) is dominated by the vibrational modes of the carbonyl, but also contains contributions from the out of phase C-N stretching, the C-C-N deformation and the N-H in-plane bend. The Amide I band is affected very little by peptide side chains and because it is representative of the backbone it is most commonly used in secondary structure analysis. This sensitivity arises from transition dipole coupling.[124,125] Transition dipole coupling is a resonance interaction between the dipoles of neighbouring amide groups and the strength of this coupling depends strongly on the relative orientations of the amide groups and their distances from each other. FTIR spectra were taken in D2O because H2O has a strong absorbance band in the amide I region which would make data analysis very difficult.

Gold nanoparticles are transparent in this region of the electromagnetic spectrum allowing direct measurements of both peptide and peptide-capped nanoparticles in aqueous solution. As with all metal surfaces, however, molecules attached to metal nanoparticles are subject to the surface dipole selection rule. Due to the high conductivity of the metal surface only vibrational modes that give rise to an oscillator that is perpendicular to the surface will be IR

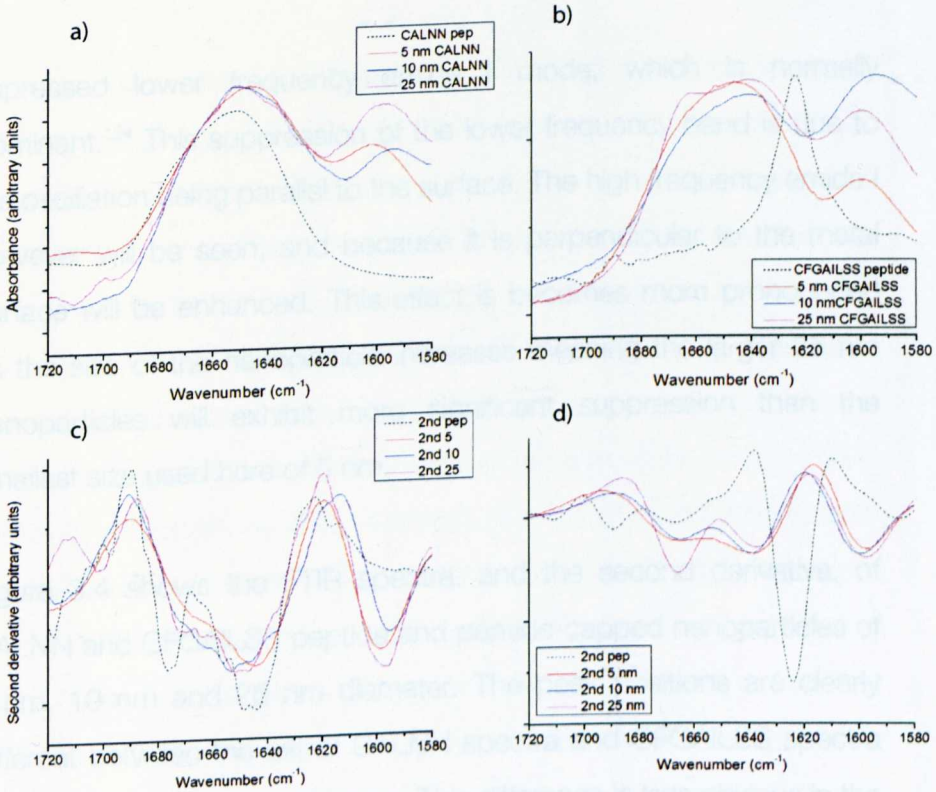

Figure 3.4. FTIR spectra of (A) CALNN peptide in solution and CALNN-capped gold nanoparticles (5, 10 and 25 nm diameter) and, (B) CFGAILSS peptide in solution and CFGAILSS-capped gold nanoparticles (5, 10 and 25 nm diameter. All spectra have been scaled to have the same maximum amide I' absorbance. Panels C and D show the second derivative of the FTIR spectra in A and B, respectively.

active and will have an observable absorption band. Oscillators that are parallel to the surface are therefore not seen.[126] It has been shown both theoretically [127] and also experimentally [128]that these selection rules apply to the surfaces of metal nanoparticles. Here the size of the particle affects how far away from the surface these dipole selection rules apply. Peptides that are anchored to the gold surface and in a parallel beta sheet conformation (Scheme 3.1b) will show a strongly

supressed lower frequency amide I mode, which is normally dominant.[124] This suppression of the lower frequency band is due to the oscillation being parallel to the surface. The high frequency amide I however will be seen, and because it is perpendicular to the metal surface will be enhanced. This effect is becomes more pronounced as the size of the nanoparticle increases meaning the larger 25 nm nanoparticles will exhibit more significant suppression than the smallest size used here of 5 nm.

Figure 3.4 shows the FTIR spectra, and the second derivative, of CALNN and CFGAILSS peptide and peptide-capped nanoparticles of 5 nm, 10 nm and 25 nm diameter. The peak positions are clearly different between the set of CALNN spectra and CFGAILSS spectra indicating differences in structure. This difference is less obvious in the smaller nanoparticles but becomes more prominent in the larger nanoparticles. The band at 1600 cm^{-1} in all spectra is that of the C-terminal carboxylate groups on the peptide and therefore its intensity is strongly pH dependent.

Figure 3.4a shows the FTIR spectra of CALNN peptide (black dashed line), 5 nm (red), 10 nm (blue) and 25 nm (magenta) CALNN-capped gold nanoparticles. The main band around 1650 cm^{-1} is the amide I band. The free peptide solution FTIR shows a broad amide I at around 1650 cm^{-1} which is consistent with a random coil (disordered) structure. [129] The same Amide I is also seen in the CALNN-capped nanoparticles. The shape or maximum of the amide I does not change as the nanoparticles increase in size meaning that there is no

size or curvature dependent structure. This result is unsurprising given the original design criteria of CALNN. It is also in agreement with molecular dynamic simulations of a CALNN monolayer.[12] Figure 3.4b shows the second derivative of the FTIR spectra. This shows the rate at which the gradient is changing in the spectrum allowing the resolution of closely overlapping bands. [130] This is a widely used band narrowing and deconvolution technique, were a negative peak in the second derivative has its minimum in the same position as the peak in the original spectrum. This method also emphasises bands with narrow distribution over those that are broad making it an excellent complimentary method to analyse spectra. A good example of this is the CALNN peptide spectrum second derivative where a band at 1672 cm^{-1} previously obscured by the amide I band is clearly visible (Figure 3.4C). This band is attributed to trifluoroacetic acid that is used for cleavage of the peptide from the solid phase at the end of peptide synthesis. It is visible in the original spectrum as a lack of symmetry but is clearly visible in the second derivative spectrum. That peak does not appear in the nanoparticle samples as the TFA does not bind to the gold surface and the TFA is eliminated at the same time as the excess peptide during the nanoparticle functionalisation procedure. The second derivative of CALNN is in agreement with the FTIR spectrum confirming that the nanoparticles of different sizes are identical with a broad peak at 1650 cm^{-1} consistent with a random coil structure.

The CFGAILSS spectra shown in figure 3.4c show significant differences between the peptide and the peptide monolayer. The

peptide (dashed line) shows two amide I bands, a large sharp dominant band at 1624 cm^{-1} and a smaller band 1689 cm^{-1}. This pair of bands is consistent with an anti-parallel β-sheet structure. These bands are however absent in the nanoparticle spectra signifying no significant amount of fibrils or anti-parallel beta sheet in the sample. The anti-parallel beta sheet is most likely unfavourable due to the geometrical constraint of the SAM: CFGAILSS is anchored to the gold through the N-terminal cysteine; this determines the orientation in the peptides within the SAM. The 5 nm CFGAILSS sample (red) shows a similar FTIR spectrum to that found in the CALNN samples giving a broad band at 1645-1650 cm^{-1} that suggests that the peptide backbone exhibits a significant amount of random coil. The second derivative (Figure 3.4c) however shows that there is also two overlapping bands at 1640 cm^{-1} and 1665 cm^{-1}. These bands are more pronounced in the 10 nm CFGAILSS FTIR spectrum (blue), which has a maximum at 1640 cm^{-1} and a shoulder at ~1665 cm^{-1}. These two bands can be seen clearly in the second derivative. These bands are also clearly visible in 25 nm CFGAILSS FTIR spectrum (magenta). These narrow bands signify that as the nanoparticles increase in size the amount of ordered structure also increases.

We are suggesting that these bands can be assigned to the parallel beta-sheet structure. That structure has a high level of similarity to the anti parallel arrangement (figure 3.5). Both structures are characterised by two peptide chains running parallel and held together by hydrogen bonds. The hydrogen bonds in parallel beta-sheet are not perpendicular to the backbone and each hydrogen

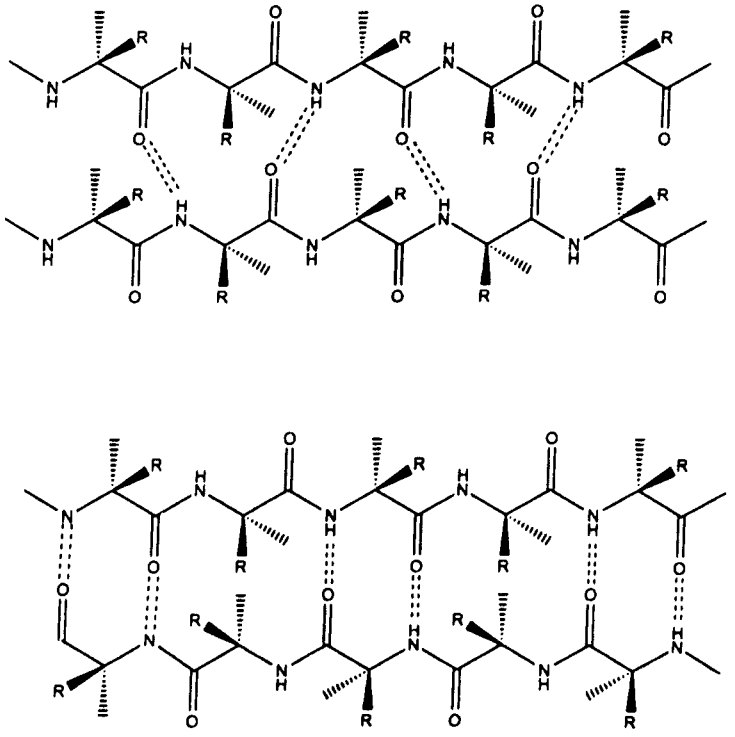

Figure 3.5. Beta-sheet structures and the hydrogen bonds that are formed; a) Parallel beta-sheet displaying the ring of 12 atoms per hydrogen bonded ring and the non-linear hydrogen bonds, b) anti-parallel beta-sheet, displaying the 10 and 14 atom hydrogen bonded rings and linear hydrogen bonds.

bonded "ring" has 12 atoms. In an anti-parallel beta sheet the hydrogen bonds are perpendicular to the backbone and the hydrogen bonded "ring" alternates between 14 and 10 atoms. Because the hydrogen bonds are perpendicular to the backbone, anti-parallel beta-sheet is more stable than parallel beta-sheet. These differences in hydrogen bonds are responsible for differences in the amide I regions.

Both beta-sheets have two narrow amide I bands, the bands being closer to each other in parallel beta-sheet, and further apart in anti-

parallel [129], parallel beta-sheet having its dominant band at higher frequencies than those for anti-parallel beta-sheet. For parallel beta-sheet the dominant band is expected at ~1630 and a much weaker band located ~20-40 cm^{-1} away at ~1650-1670 cm^{-1}.[129,131,132] These frequencies correspond to the two narrow bands in the FTIR spectra of the CFGAILSS-capped nanoparticles. Both the relative band heights and widths are not as expected for an infinite theoretical parallel β-sheet. This is probably due in part to the modes of vibration (eigenmodes) that are dependent on the number of peptides in any given beta-sheet, but also the orientation of these modes relative to the metal surface and the consequential affect of the surface dipole selection rule. These two effects are discussed further below.

For an infinite parallel beta-sheet only two oscillator vibrations are IR active [129,131-133], the dominant absorbance band at a lower frequency and a weaker absorbance band at higher frequencies. The dominant band comes from a vibration that is polarised perpendicular to the backbone and the weaker band is polarised parallel to the backbone. For beta-sheets consisting of less than ~7 residues, the modes of vibration change without significantly affecting polarisation of the vibrations. As fewer residues are included into the bets-sheet this causes a shift of the dominant band to higher frequencies but the higher frequency band is much less affected. We suggest that because the nanoparticles are confined to an inherently curved surface, this limits the number of peptide residues that can align properly into parallel beta-sheet, the smaller nanoparticles, exhibiting greater curvature, showing fewer residues that can align into a

continuous beta-sheet than the larger sizes which have an inherently lower surface curvature. The slightly higher frequencies seen in the low frequency band, 25 nm sample: 1637 cm-1 and the 10 nm sample: 1639 cm-1, are in agreement with this hypothesis. The low frequency band seen in nanoparticle FTIR spectra is much less affected, and its band position remains fairly constant at ~1665 cm-1. The broadening that is seen in the nanoparticle FTIR spectra is due to structural inhomogeneity. Since the nanoparticle sample is inherently inhomogeneous in both size of nanoparticle and surface topology, this generates different populations of different numbers of peptides in parallel beta-sheet. The intensity of the low frequency band is also suppressed because it is orthogonal to the peptide backbone and therefore parallel to the surface. As detailed above, the surface dipole selection rule causes this band to be suppressed, which is consistent with what is seen in the FTIR spectra.

3.5 2D IR study of the CFGAILSS nanoparticles.

Vibrational spectroscopic methods, such as FTIR and Raman generate a complicated 1D spectrum that can sometimes be difficult to analyse in detail. 2D infrared spectroscopy (2D IR) generates spectra in two dimensions reducing this complexity [134] [135] and allowing ultrafast time resolution.[134,136,137] In 2D IR a spectrum is spread over two frequency axes to reveal vibrational couplings through cross peaks. The spectrum correlates the frequency of vibrational excitation (ω_{pump}) with the frequency of detection (ω_{probe}). The peaks seen in the diagonal can be assigned to normal, chemically distinct vibrational

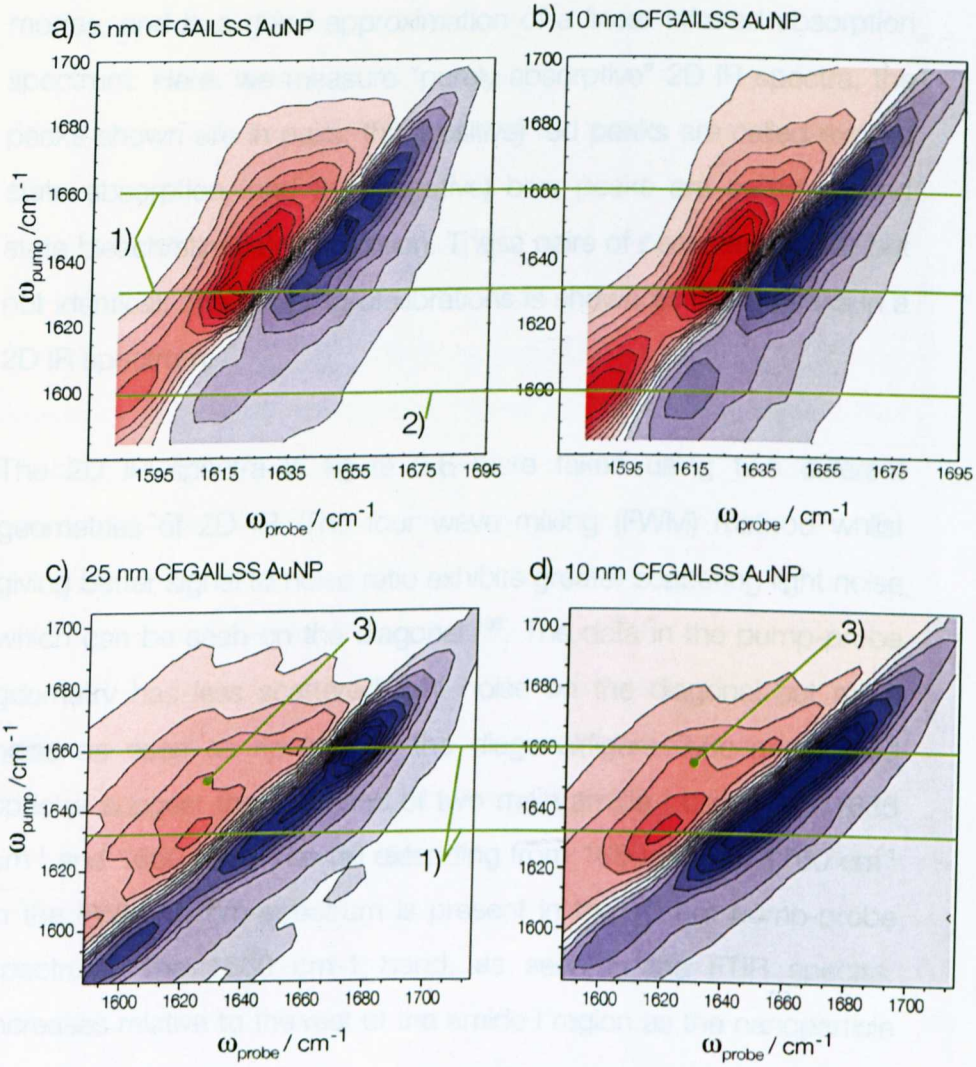

Figure 3.6. 2D IR spectra of; a) 5 nm diameter and, b) 10 nm diameter CFGAILSS-capped nanoparticles taken with the four wave mixing geometry. 2D IR spectra of c) 25 nm diameter and, d) 10 nm diameter CFGAILSS-capped nanoparticles taken with the pump-probe geometry. Numbers indicate band positions; 1) ~1635 cm and 1660 cm amide I, 2) 1600 cm COO, 3) indicates the emergence of a cross peak between the 1635 cm and 1660 cm peaks.

modes, and is a good approximation of a linear infrared absorption spectrum. Here, we measure "purely absorptive" 2D IR spectra, the peaks shown are in pairs; the (positive) red peaks are called excited state absorption, and the (negative) blue peaks are called ground state bleach/stimulated emission. These pairs of peaks are similar but not identical. The coupling of vibrations is shown as cross peaks in a 2D IR spectrum.

The 2D IR spectra in figure 3.6 were taken using two different geometries of 2D IR. The four wave mixing (FWM) method whilst giving better signal to noise ratio exhibits greater scattering light noise which can be seen on the diagonal [138]. The data in the pump-probe geometry has less scattered light noise on the diagonal but more noise as seen as rippling off the diagonal(figure 3.6c and d). All spectra suggest the presence of two main amide I bands at ~1635 cm^{-1} and 1660 cm^{-1}. The tail extending from 1680 cm^{-1} to 1760 cm^{-1} in the FWM 10 nm spectrum is present in the 10 nm pump-probe spectrum. The 1660 cm-1 band, as seen in the FTIR spectra, increases relative to the rest of the amide I region as the nanoparticle diameter increases.

The FWM spectra show differences in the contour lines between the 5 nm and 10 nm samples. The 5 nm sample (figure 3.6a) shows more rounded contour lines in the red excited/absorption spectrum, whilst the 10 nm (figure 3.6b) shows the emergence of a side peak implying the presence of more beta sheet. The emergence of these cross peaks is more visible in the 25 nm sample (figure 3.6c) implying a

further increase in the amount of beta sheet present in the sample. The diagonal stimulated emission/bleach spectrum (blue) follows the FTIR data well, the 1660 cm^{-1} band being stronger as the nanoparticles increase in size.

The 2DIR bleach/stimulated emission bands scale as the forth power of each vibrator's orientationally averaged dipole moment. In FTIR the spectrum scales with the second power of the dipole moment, and therefore a 2DIR signal will be more sensitive to changes in dipole moment. This is seen in the increased absorbance at 1660 cm^{-1} in the FTIR and 2DIR comparisons (Figure 3.7c and d). It should be noted however that for β-sheet this increase in signal is supressed by the anharmonicity of the excitonic states that are formed. In figure 3.7c) and d) an increase in the1660 cm^{-1} band can be clearly seen relative to the 1630 cm^{-1} band. It is increased by roughly the same amount in both spectra. This suggests that the 1635 cm^{-1} and 1660 cm^{-1} band ratios in the 10 nm and 25 nm samples are similar.

From the 2DIR data we can conclude, due to band position) that there is mixture of β-sheet structure present in the CFGAILSS nanoparticles which increases with particle diameter. It has previously been shown that the absence of a cross peak in the 2DIR does not exclude parallel β-sheet and its absence may constitute evidence for parallel β-sheet [133]. Whilst a band at ~1635 cm^{-1} has also been attributed a random coil [135] the presence of the band at 1660 cm^{-1} is evidence for beta sheet. [124]

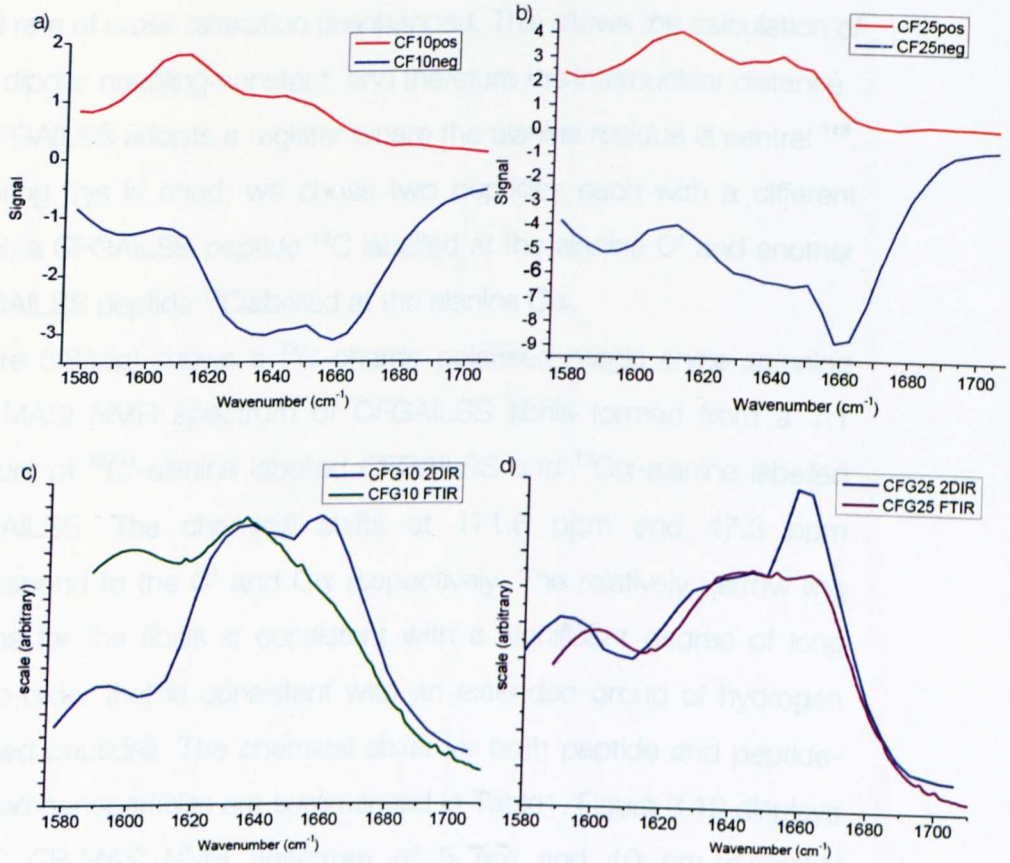

Figure 3.7. Comparison of diagonal cuts of the bleach/stimulated emission from 2DIR spectra of a) 10 nm CFGAILSS and b) 25 nm CFGAILSS. The bleach/stimulated emission diagonal peaks are compared to the FTIR spectra for c) 10 nm CFGAILSS and d) 25 nm CFGAILSS. The spectra shown in c) and d) are normalised to the 1635 cm peak height and the 2DIR data has been inverted for ease of comparison.

3.6 Solid-state NMR rotational-resonance

Rotational resonance is a magic angle spinning (MAS) NMR technique that selectively restores the dipolar interaction between a spin pair. When the rate of sample spinning matches the difference in resonant frequencies of the non-equivalent nuclei the measured peaks broaden

and rate of cross relaxation is enhanced. This allows the calculation of the dipolar coupling constant, and therefore the internuclear distance. NNFGAILSS adopts a register where the alanine residue is central [118]. Bearing this in mind, we chose two peptides each with a different label; a CFGAILSS peptide ^{13}C labelled at the alanine C' and another CFGAILSS peptide ^{13}Clabelled at the alanine Cα.

Figure 3.8(top) shows a ^{13}C charge polarised magic angle spinning (CP-MAS) NMR spectrum of CFGAILSS fibrils formed from a 1:1 mixture of $^{13}C'$-alanine labelled CFGAILSS and $^{13}C\alpha$-alanine labelled CFGAILSS. The chemical shifts at 171.6 ppm and 47.3 ppm correspond to the C' and Cα respectively. The relatively narrow line widths for the fibrils is consistent with a significant degree of long range order that is consistent with an extended group of hydrogen bonded peptides. The chemical shifts for both peptide and peptide-capped nanoparticles are summarised in Table1. Figure 3.10 displays a ^{13}C CP-MAS NMR spectrum of 5 nm and 10 nm diameter CFGAILSS-capped gold nanoparticles respectively. These were capped with a 1:1 mixture of $^{13}C'$-alanine labelled CFGAILSS and $^{13}C\alpha$-alanine labelled CFGAILSS. The width of the peaks seen in the nanoparticle sample is wider than that seen in the fibril sample. This broadening is seen to increase further in 10 nm nanoparticles. This

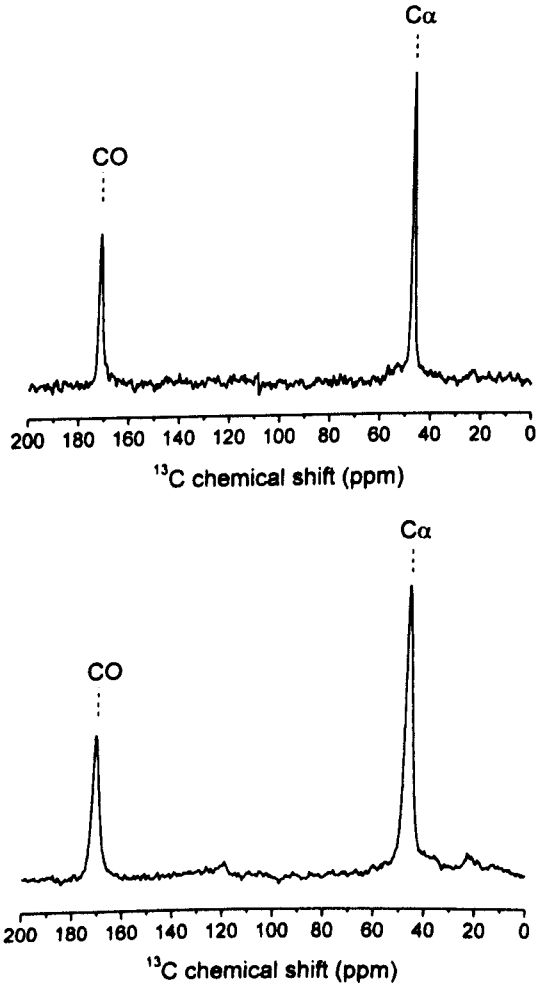

Figure 3.8. A ^{13}C CP-MAS NMR spectra of 1:1 [^{13}C'-A]CFGAILSS:[^{13}Cα-A]CFGAILSS fibrils (top) and 5 nm gold nanoparticles capped with 1:1 [^{13}C'-A]CFGAILSS:[^{13}Cα-A]CFGAILSS (bottom).

sample	chemical shift (ppm)		Line width (Hz)	
	C'	Cα	C'	Cα
CFGAILSS fibrils	171.6	47.3	125.2	115.1
CFGAILSS nanoparticle				
5 nm	170.8	46.4	300.0	307.9
10 nm	171.8	48.6	452.4	450.5
CALNN nanoparticle				
5 nm	172.6	48.7	473.0	435.6
10 nm	173.1	49.2	513.0	502.3

Table 3.1. Summary of ^{13}C chemical shifts and line widths at half height for C' and Cα of CFGAILSS fibrils and CFGAILSS- and CALNN-capped nanoparticles.

broadening is thought to arise from both structural disorder imposed by the peptide being anchored to the gold core, and also as a property of the gold nanoparticle itself. It has been shown that ^{13}C chemical shifts for thiolated ligands on gold nanoparticles exhibit broadening whilst conjugated to the nanoparticle [83]. This broadening is most pronounced closest to the gold core, but it also increases as the gold core increases in size.[47] This effect has been attributed to variations in the Au-ligand site, giving rise to distributions of chemical shifts.[47] [83] Since the nanoparticles are metal, the conduction

electrons may introduce a distribution of weak knight shifts that may contribute to this broadening [139]. The conduction electrons of the gold surface introduce an effective field at the nuclear site due to spin

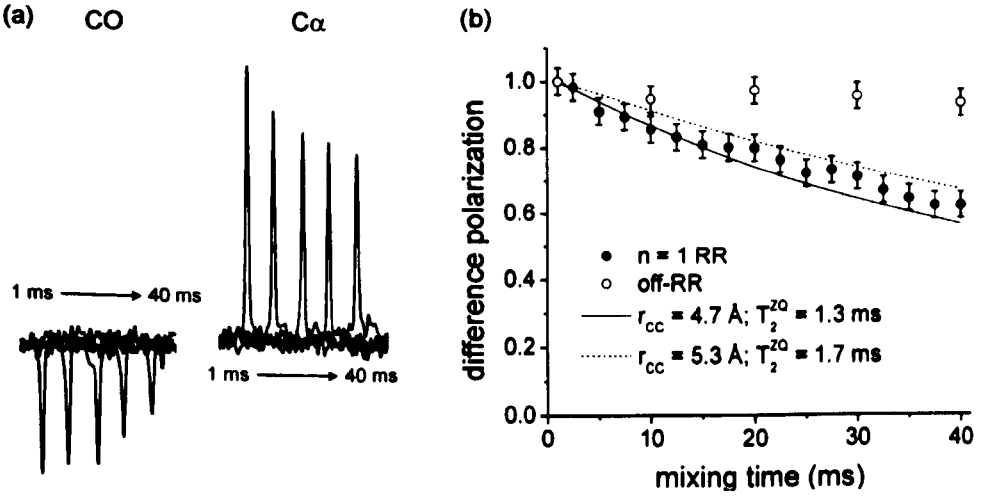

Figure 3.9. Measurement of C'-Cα dipolar couplings in 1:1 [C'-A]CFGAILSS:[Cα-A]CFGAILSS fibrils using rotational resonance NMR. (a) Spectra of fibrils obtained using the constant time experiment. Peaks for C' and Cα are shown, from left to right, for mixing times (τ) of 1, 10, 20, 30 and 40 ms at a MAS frequency of 12508 Hz, which satisfies the n = 1 RR condition. (b) A plot of magnetisation exchange, as represented by difference intensities for the C' and Cα peaks over a range of mixing times. Data are shown for n = 1 RR (filled circles) and for a MAS rate (5200 Hz) away from a RR condition (open circles). Error bars represent the level of the noise. Solid and dashed lines are numerically simulated curves bounding the upper and lower error limits of the n = 2 RR data, and correspond to the C'-Cα distances and T_2^{ZQ} values indicated.

orientations in the presence of the applied external magnetic field. This effect is known to increase with the size and/or density of the nanoparticles. [83] The increase in line width with nanoparticle size is more pronounced in the case of CALNN-capped nanoparticles than

in the case of CFGAILSS nanoparticles. This is consistent with the FTIR data that indicates an increase of order with size.

Figure 3.9a shows the 1:1, ^{13}C'-alanine:^{13}Cα-alanine labelled CFGAILSS fibrils sample in a rotational resonance experiment. The decrease in signal intensities with increased mixing time indicates that the distance-dependant
dipole coupling occurs between the ^{13}C' and ^{13}Cα labels of adjacent CFGAILSS peptides. Comparison of the exchange measurements with simulated curves (figure 3.9b) gives a dipolar coupling constant which translates to an intermolecular distance of 5 Å ± 0.3 Å. This short distance is possible if the labelled residues are in register to one another within a beta-sheet since hydrogen bonds are between 2 and 3.5 Å. In Figure 3.10a is the rotational resonance spectra of 5 nm diameter gold nanoparticles capped with 1:1, ^{13}C'-alanine:^{13}Cα-alanine labelled CFGAILSS. In a similar way to the fibril spectra, the 10 nm spectra shows a decline in peak intensities with increasing mixing time indicating that the dipole coupling occurs between the ^{13}C' and^{13}Cα labelled alanines of adjacent peptides. The exchange measurements give a dipolar coupling constant indicative of an intermolecular distance of 4.9 Å ± 0.3 Å. The rotational resonance spectra of a 10 nm gold nanoparticle capped with the same mixture of ^{13}C'-alanine and ^{13}Cα-alanine labelled CFGAILSS also shows the decline in intensities with increased mixing times indicating dipole coupling, and an intermolecular distance of 5 Å ± 0.3 Å. As described above the peptide is anchored to the gold by a thiol bond meaning the peptide cannot adopt an anti-parallel beta-sheet structure as in

the fibrils. In order for this intermolecular distance of 5 Å to be possible the peptides would have to adopt a register where the C=O of the alanine hydrogen bonds to the N-H on the glycine of the neighbouring residue. The rotational resonance spectra was also performed on CALNN capped 5 nm and 10 nm gold nanoparticles. The monolayer was a mixture 1:1 of ^{13}C'-alanine :^{13}Cα-alanine labelled CALNN. The CALNN-capped nanoparticles did not show any peak intensity changes over the same mixing times used in the CFGAILSS experiments. This is indicative of very weak dipole coupling and that the intermolecular distance is significantly greater than that seen in the CFGAILSS-capped nanoparticles and CFGAILSS fibrils. CFGAILSS and CALNN have a similar capping densities, but the CALNN peptide is not amyloidogenic and does not have the same propensity to form beta-sheet as CFGAILSS. If the observed coupling was due to the peptides being confined to the nanoparticle surface both the CALNN and CFGAILSS capped nanoparticles would show dipole coupling due to the proximity of the peptides. The labelled alanine in CALNN is also closer to the surface and thus more likely to be in closer

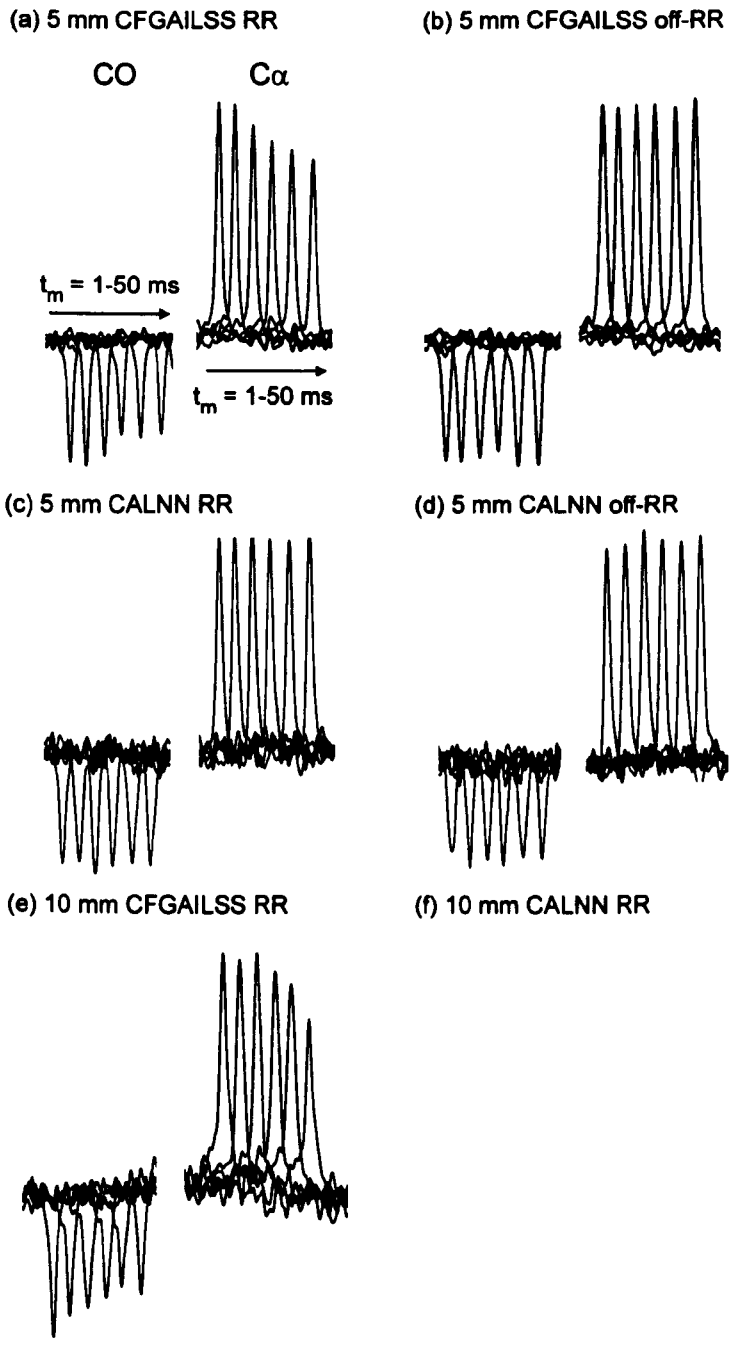

FIGURE 3.10. Detection of -C'--Cα dipolar couplings in peptide-capped gold nanoparticles using rotational resonance NMR. Peaks for C' and Cα are shown, from left to right, for mixing times (τ) of 1, 10, 20, 30, 40 and 50

ms at MAS frequencies satisfying the n = 2 RR condition. Top row: spectra for 5 nm particles capped with 1:1 [^{13}C'-A]CFGAILSS:[^{13}Cα-A]CFGAILSS at n = 2 RR (a) and off-RR (b). Middle row: spectra for 5 nm particles capped with 1:1 [^{13}C'-A]CALNN:[^{13}Cα-A]CALNN at n = 2 RR (c) and off-RR (d). Bottom row: spectra for 10 nm particles capped with 1:1 [^{13}C'-A]CFGAILSS:[^{13}Cα-A]CFGAILSS (e) and 1:1 [^{13}C'-A]CALNN:[^{13}Cα-A]CALNN (f) at n = 2 RR.

proximity to another CALNN peptide than the CFGAILSS peptide. Instead only the CFGAILSS peptide is seen to be in close enough proximity to imply hydrogen bonding. Interestingly the line widths of the CALNN-capped nanoparticles are much larger than the CFGAILSS-capped nanoparticles. As described above the peptide being anchored to the nanoparticles causes broadening of the peaks as the nanoparticle increases in size. Since the CALNN-capped nanoparticles have been shown to have a random coil structure, this structural inhomogeneity would result in larger line widths combined with the nanoparticles.

3.7. Conclusions

Here we have shown that it is possible to design and synthesise gold nanoparticles capped with a CFGAILSS monolayer that exhibits long range order in the form of protein secondary structure. These nanoparticles have resistance to salt-induced aggregation to the same extent as CALNN-capped nanoparticles, but the CFGAILSS-capped nanoparticles exhibit a greater resistance to ligand exchange, presumably due to the increased affinity each peptide has for its neighbouring peptide. FTIR and 2DIR have shown that the peptide monolayer is made up of both β-sheet and random-coil, the amount

(a) 5 nm CFGAILSS

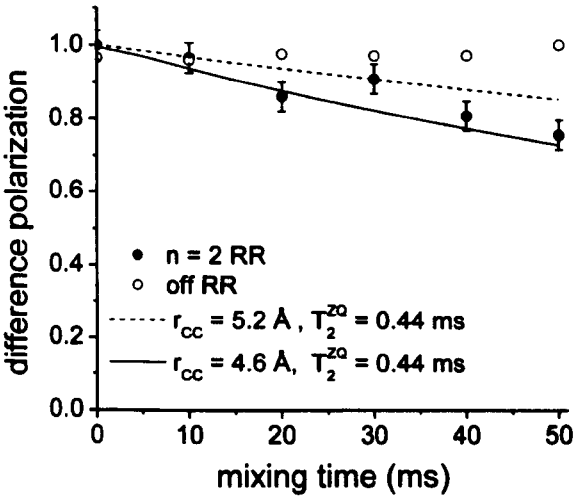

(b) 10 nm CFGAILSS

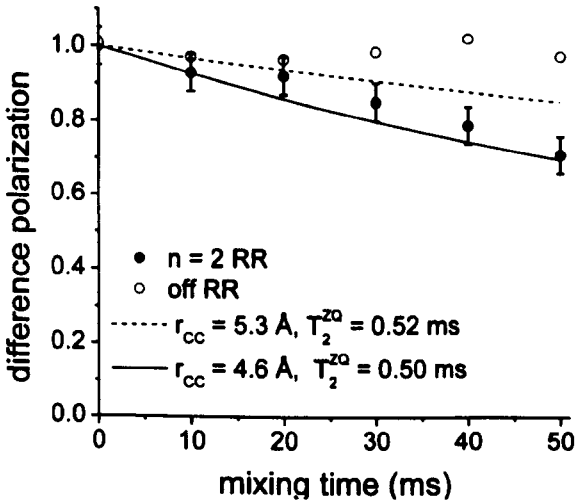

Figure 3.11. Plots of magnetisation exchange for 5 nm (a) and 10 nm (b) nanoparticles capped with 1:1 [-C'-A]CFGAILSS:[-Cα-A]CFGAILSS. Data are shown for n = 2 RR (filled circles) and for a MAS rate (5200 Hz) away from a RR condition (open circles). Solid and dashed lines are numerically

simulated curves bounding the upper and lower error limits of the n = 2 RR data, and correspond to the C'-Cα distances and T_2^{ZQ} values indicated.

of β-sheet structure present on a nanoparticle increasing as the nanoparticle size increases. This is most likely due to the reduction in the surface curvature allowing more peptide residues to join a beta-sheet structure, less hindered by geometric constraints. Solid state NMR has demonstrated that the CFGAILSS-capped nanoparticles exhibit an inter-peptide spacing consistent with that in β-sheet, and that this is not merely an effect of being confined to a surface since the CALNN peptide does not show the same effect. To our knowledge these studies are the first molecular level details on the structure of peptide self-assembled monolayers, as well as direct spectroscopic evidence of local 2D order at the surface of the nanoparticles.

CHAPTER 4

Ultrafast heating of nanoparticles

4.1 Femtochemistry and surfaces

Femtochemistry addresses chemical reaction processes including the formation and breaking of bonds that take place on the femtosecond time scale. Resolution of processes to this degree requires lasers with ultrashort pulse lengths. Femtochemistry has enhanced the understanding of chemical reactions in liquid and gas mediums over the past decades. Surfaces have represented a challenge in femtochemistry due to their additional complexity of the heat dissipation channels as a result of a solid interface interacting with the reactants. Surface reactivity is of particular importance to catalysis in the development of heterogeneous catalysts. Metals are often used to investigate reactions with molecules due to favourable effects such as a reduced reaction barrier compared to a gas phase reaction. In addition the use of a surface allows the reactant's proximity to be controlled enabling greater control over the reaction dynamics and products.

4.3 Ultrafast heating of metal substrates

In a metal substrate there are two heat baths, the sea of electrons and the metal atom nuclei forming the lattice, collectively constituting the energy content of the substrate. The collective excitations of the metal lattice heat bath are described as phonons. The two heat baths, phonon and electron, in a metal surface are in a state of

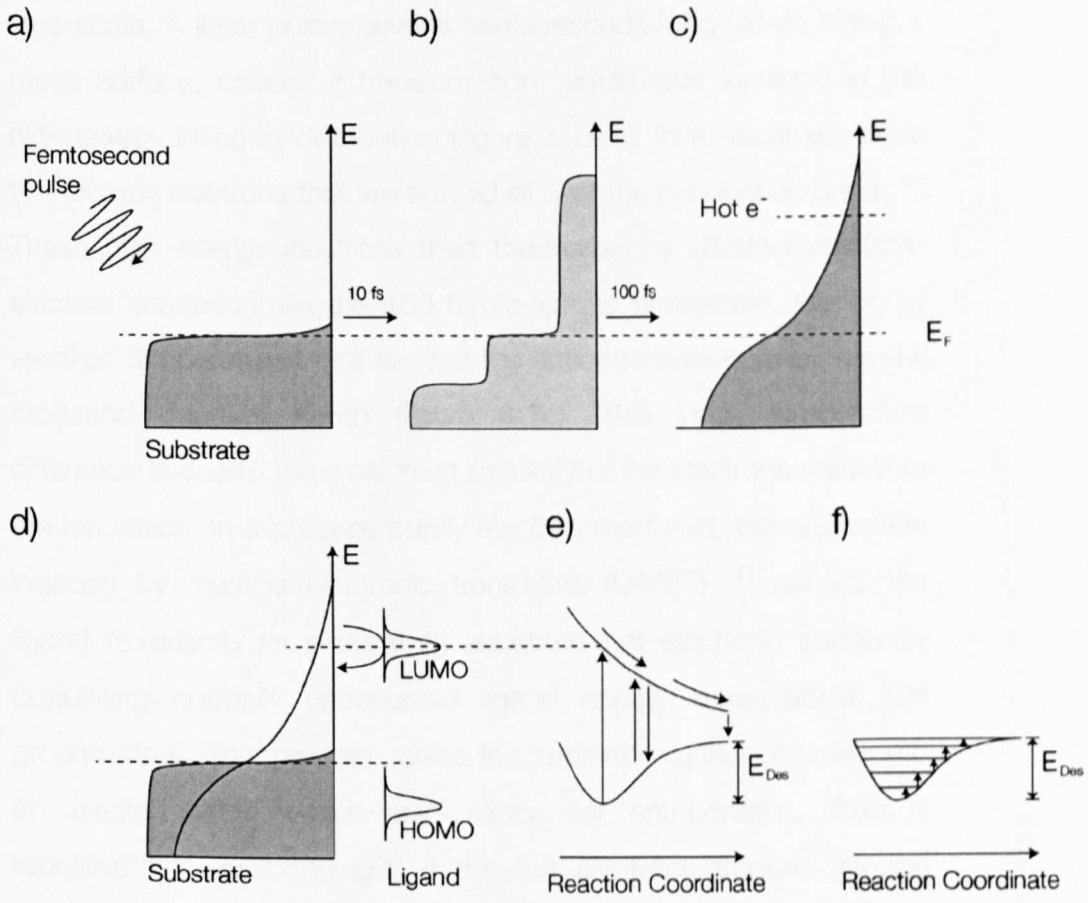

Figure 4.1.Electron distributions; Fermi-Dirac distributions; a) Fermi-Dirac distribution of the cold electrons in a metal substrate are excited by a femtosecond laser pulse, b) this causes a transient population of high energy electrons with energy above the Fermi level (E) in a non-thermal distribution, c) The electrons thermalise by electron-electron scattering resulting in a population of hot electrons. d) DIMET diagram; the hot electron mediated energy exchange due to transfer of an electron to the ligand unoccupied orbitals from the high energy end of the electron occupation distribution e) The repeated energy transfer to the ligand by the electrons supplies the necessary energy to excite the ligand out of the ground state and overcome the desorption energy. f) Hot phonon mediated breaking of bonds, more energy is added to a particular bond vibration causing the bond to break and the ligand to dissociate.

equilibrium because of electron-phonon coupling on the picosecond time scale. A laser pulse, several femtoseconds long, when hitting a metal surface, causes a transient non- equilibrium increase in the high-energy electron distribution (figure 4.1a-c). In a metal substrate this creates electrons that are spread all over the conduction band. [140] These high energy electrons then thermalise by ultrafast electron-electron scattering, on the 100 femtosecond time scale, leading to electron temperatures that exceed the lattice temperature by several thousand degrees Kelvin (figure 4.1c). This large temperature difference is due to the small heat capacity of the electrons relative to the ion lattice. In a process purely electron-mediated, the desorption induced by multiple electronic transitions (DIMET) [141] causes the ligand to desorb as a result of substrate hot electrons transiently populating normally unoccupied ligand energy levels above the ground state. This process raises the substrate-ligand complex into an excited state which can either be anti-bonding, that is repulsive[142,143], or bonding[144] if the hot electrons contain enough energy to access the lowest unoccupied molecular orbitals of the ligand (LUMO) . This new charge distribution caused by the transient electron excitation can initiate nuclear motion, converting potential energy into kinetic energy and after back electron transfer to the ground state, vibrational energy. The coupling of this transient electronic state to the vibrational degrees of freedom of the adsorbed ligand causes desorption or even reactions between co-adsorbed ligands[145] (Figure 4.1e). In the unexcited substrate state (electrons mostly below the Fermi level), the cold electrons do not have access to the higher energy unoccupied electron levels of the ligand. When

hot electrons are at high excitation densities additional excitation cycles may occur, before the vibrational relaxation takes place, allowing enough energy to accumulate in the ligand to overcome the reaction barrier and break the bond (figure 4.1e). Substrate-ligand coupling transfers energy to the ligand molecule until equilibrium is reached. Energy is then dissipated via electron scattering in the bulk, or by electron-phonon coupling. This leads to an increase in the phonon temperature, which is a much slower process than the electron temperature increase. Within the electron-phonon coupling time of the metal substrate (~1 ps) [145,146] the temperature of the two heat baths begin to equilibrate. Energy can also be deposited into the electron heat bath by exciting interband transitions (blue shifted wavelengths of the localised surface plasmon resonance), or intraband transitions (red shifted wavelengths of the localised surface plasmon resonance). [79] This causes a differences in the way in which the electrons are distributed over the conduction band. [79] These differences however equilibrate with the electron-electron scattering whilst forming the hot-electron distribution.

Hot-phonons are formed as the energy from the photons is conducted into the electrons and then in the phonons. These hot-phonons can also cause molecular bonds to break by coupling with vibrational modes of the substrate-ligand bond (figure 4.1f), such as a stretching vibration. This causes the ligand to dissociate, if enough energy is transferred. This mode of bond breaking is distinct from the hot electron mediated process due to the longer time scale on which

it occurs, given by the hot-phonon relaxation time (phonon-phonon coupling) (~500 ps). [140]

4.2 Metal nanoparticles

Metal nanoparticles, show a strong absorbance of light in specific areas of the electromagnetic spectrum. These light absorbing properties make them ideal candidates as probes,[147] molecular delivery vehicles [148] and also as heat sources[149]. As previously discussed, nanoparticles are often coated with a self-assembled ligand shell. The number of defects in this self-assembled monolayer has been shown to decrease as the size of the nanoparticle increases.[81]

More recently, nanoparticles have been shown to act as molecular tags for single molecule imaging in photothermal microscopy.[77,111-113,149] This technique is made possible by the surface plasmon resonance of metal particles, giving rise to a strong absorption of light and its conversion into heat . Any light energy absorbed and not emitted is converted to heat that is subsequently conducted into the immediate surrounding medium. This conversion of light energy to heat within the nanoparticle is a rapid process occurring on the picosecond time scale. The applied heating of the nanoparticles in this technique is over microseconds, and this allows the heat baths within the nanoparticles to remain in equilibrium.

It is possible to investigate these energy absorption and dissipation processes on gold nanoparticles by quantifying the dissociation of

ligands chemisorbed to the gold surface by a thiol-gold bond. Jain *et al.* [77] demonstrated that the femtosecond laser heating of gold nanoparticles causes DNA ligands, anchored to the gold nanoparticle surface by a gold-thiol bond, to dissociate from the gold nanoparticle causing a plasmon band shift to lower wavelengths, which was measured using UV-visible absorption spectroscopy. The authors however do not investigate over what time scale the observed ligand desorption takes place and hence it remains uncertain, precisely which processes are responsible for the breaking of the gold-thiol bond.

Here, we use a green 532 nm, 150 femtosecond long, laser pulse to induce ligand desorption and investigate the time scale of the interaction relevant for photodissociation. This femtosecond laser pulse is split into two beams, one beam travelling a fixed distance and the other over a variable delay line. This delay line introduces the delay by making the laser pulse travel a variable distance. The speed of light is 2.998×10^8 ms^{-1} so a distance of 1 mm will introduce a delay of 3.34 ps to the beam. When the beams are combined the delay becomes the determining factor whether enough energy is delivered to the electrons, quickly enough, to cause the breaking of the gold-thiol bond, before the energy has diffused into the phonons or the surrounding environment. Both beams are sent to a lens, of focal length 700 mm, which focuses the beams as a 150 μm diameter spot on the sample. The spatial and temporal overlap are adjusted and optimised using second-harmonic generation in a non-linear crystal. The gold nanoparticles that were used were capped with a peptide

monolayer consisting of two peptides; CALNN (95%) and a fluorescently labelled peptide CCALNNGGGP-acetoxymethyl coumarin (AMC) (5%). The absorption band for the AMC fluorophore is in the UV at 324 nm and does not overlap with the 532 nm femtosecond laser light, and thus will be unabated by photo-bleaching. When conjugated to the gold nanoparticle the fluorescence will be quenched due to its proximity to the gold core[150], and so only fluorophore that has dissociated from the nanoparticle will be detected by fluorescence measurements. Fluorescence could not be measured *in situ* and so was done after irradiation, removing a sample of nanoparticles from the rapidly stirred experimental volume. The irradiation time was changed as the sample volume decreased to ensure the desired mean irradiation time per nanoparticle.

The nanoparticle concentration was adjusted so that the A_{532} was 0.5 in order for the beam not to be too attenuated as it passes through the 1 cm path length cuvette. Ideally all of the sample would be illuminated by the same amount of light, but with an absorbance of 0.5 only 32 % of the light escapes the sample, meaning the front of the sample in the cuvette is irradiated by 100 % of the light energy and the back only receives 32 %. Any higher concentration would mean that there would be a greater proportion of light energy absorbed by the front of the sample than the back, but any smaller concentration would lead to weak fluorescence that would be difficult to reliably measure. It is not possible to increase the monolayers proportion of fluorescent ligand due to the ligand causing aggregation

when it constitutes greater than a 5% molar ratio, to CALNN, in the self-assembled monolayer.

Two different nanoparticle core diameters, 10 nm and 30 nm, were used in this study. This provides more evidence for the processes that are responsible for ligand dissociation. Whilst the electron-phonon coupling is independent of nanoparticle core size, the phonon-phonon coupling decreases quadratically with size [140]. This will mean that heat energy will be dispersed more slowly in the 30 nm nanoparticles than in the 10 nm. 10 nm was chosen because it is a large enough diameter to have a significant electron-phonon and phonon-phonon relaxation difference, and 30 nm was selected because as gold nanoparticles increase in size the A_{532} also increases relative to the nanoparticle concentration [8], meaning a lower concentration of particles would have to be used.

The energy delivered by the laser is critical to observe the processes of ligand desorption. If too little energy is delivered nothing will be seen, and if too much energy is delivered the ligands will dissociate all at once, and no difference will be seen when the second pulse hits the sample yielding no information on processes causing the ligand dissociation. To select the appropriate laser power the nanoparticles were irradiated with laser energies between 5 and 53 μJ (Figure 4.2). The appropriate laser power was required to not reach saturation before the final reading, thus ruling out 53 and 20 μJ, whilst allowing for the greatest signal to noise ratio. 4 μJ did not result in all of the conjugated fluorescent ligand being dissociated; therefore a laser

power of 7 μJ was selected. There is evidence to indicate that as the fluorescence plateaus in the power dependence readings

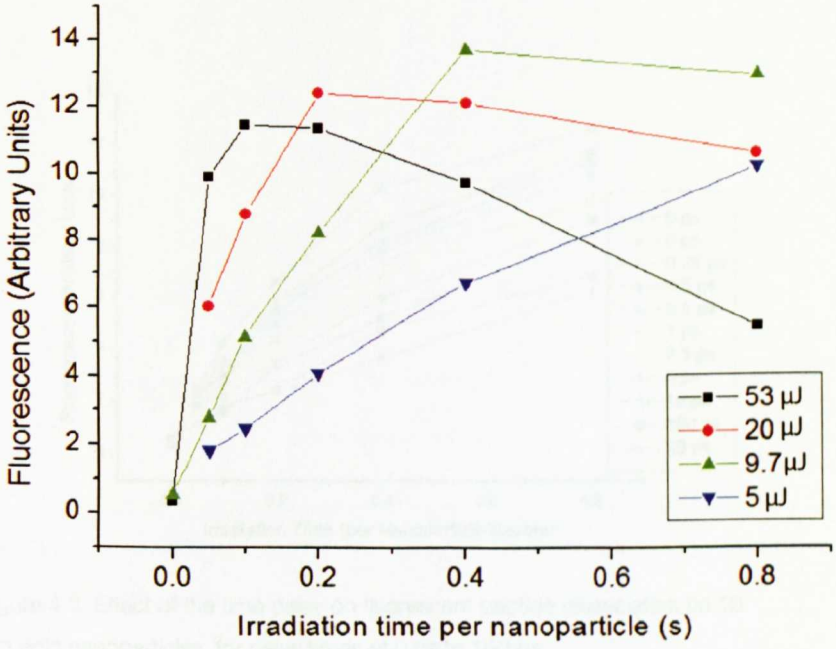

Figure 4.2. Laser power dependence of fluorescently labelled peptide dissociation from 10 nm diameter gold nanoparticles capped with 5% CCALNNGGGP-AMC and 95% CALNN. Delay between the two pulses: 0 ps.

almost all of the ligand shell has been removed from the nanoparticles because no more fluorescence can be measured with further irradiation. The fluorescence visibly decreases after saturation at both of the higher laser powers used. Whilst the cause of this is not precisely known there is evidence to indicate that it could be due to the production of free radicals produced by the laser exciting the gold

particle.[151] These radicals could react with the fluorophore causing oxidation and bleaching.

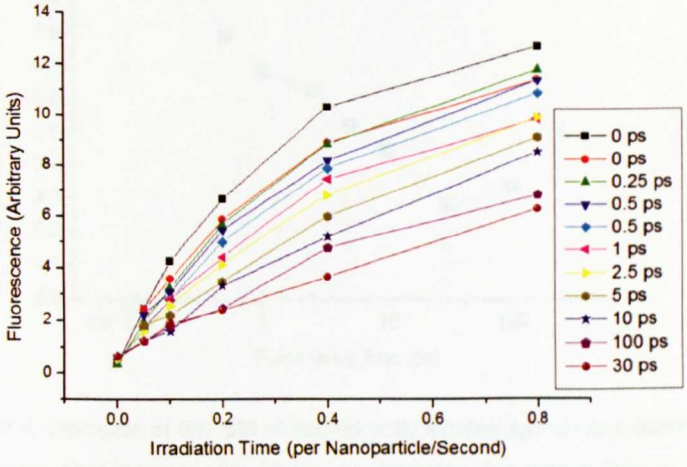

Figure 4.3. Effect of the time delay on fluorescent peptide dissociation on 10 nm gold nanoparticles, for delay times of 0 ps to 100 ps.

In the delay experiments the total energy of the recombined beams was 7 μJ. The delay between the two pulses introduced will strongly affect the amount of energy that is delivered to the electrons before the system has time to equilibrate. This allows us to determine the relaxation time scale of the relevant interaction, and thus distinguish between hot electron- and phonon-induced dissociation.

Figure 4.3 shows that a gradual decrease in the rate of fluorescence release is seen as the delay time increases. These data were fitted together with an exponential rise function, sharing the amplitude and offset but with free rate of increase to give the data shown in Figure 4.4.

The cross correlation (figure 4.4) shows a marked decay of the rate of fluorescence increase as the delay time increases. In this case, i.e. for

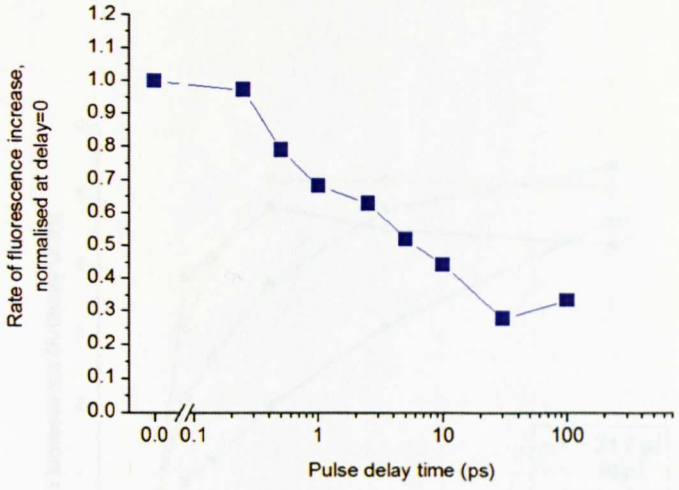

Figure 4.4. Decrease of the rate of fluorescently labelled ligand dissociation as the delay time increases for 10 nm nanoparticles. The data is from that presented in Figure 4.5.

10nm NPs, the difference between electron-phonon and phonon-phonon relaxation is too small to definitively say what processes are responsible for the release of ligands. Since the effect is strongest for the first one ps, this would indicate a hot electron mediated process. However, phonon-phonon relaxation for 10nm NPs is expected to occur with a time constant of ~15 ps, making it difficult to reliably distinguish between the two mechanisms. As discussed above, since the electron-phonon relaxation time is independent of the nanoparticle diameter, and the phonon-phonon relaxation increases quadratically with nanoparticle diameter, larger nanoparticles should show a larger

difference in the change of the fluorescence increase rate with respect to the delay time.

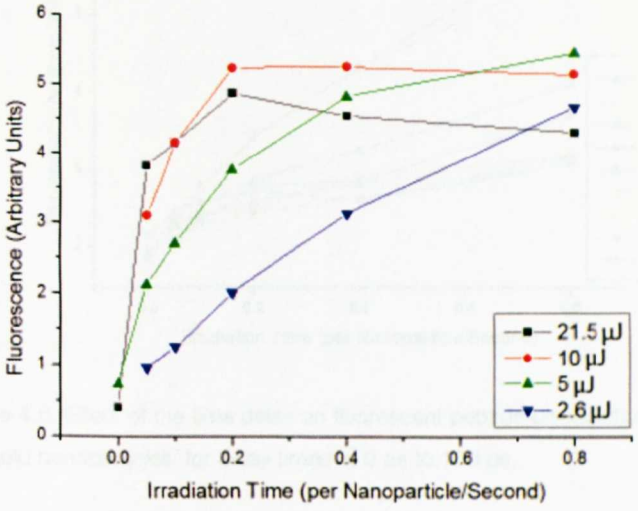

Figure 4.5. Laser power dependence of fluorophore release from 30 nm diameter gold nanoparticles capped with 5% CCALNNGGGP-AMC and 95% CALNN. Delay between the two pulses: 0 ps.

Figure 4.5 shows that the larger nanoparticles require a laser power of 5 µJ to obtain the adequate amount of fluorescence increase. Since the 30 nm particles have a lower surface area compared to the 10 nm particles for the same A_{532} the overall fluorescence is lower.

In Figure 4.7 we see that the rapid dissociation process is largely over after a delay of one ps for the 30 nm nanoparticles. This result is also very similar to the cross correlation for the 10 nm nanoparticles. The cross correlation for the 10 nm nanoparticles shows a FWHM of 2 ps and the 30 nm nanoparticles show a FWHM of 0.5 ps. We suggest

that this is most likely due to the differences in pulse energies. The electron-phonon coupling remains independent of nanoparticle size

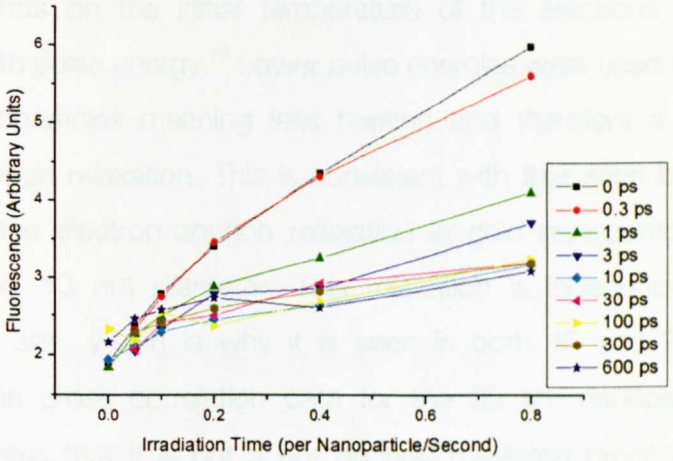

Figure 4.6. Effect of the time delay on fluorescent peptide dissociation on 30 nm gold nanoparticles, for delay times of 0 ps to 100 ps.

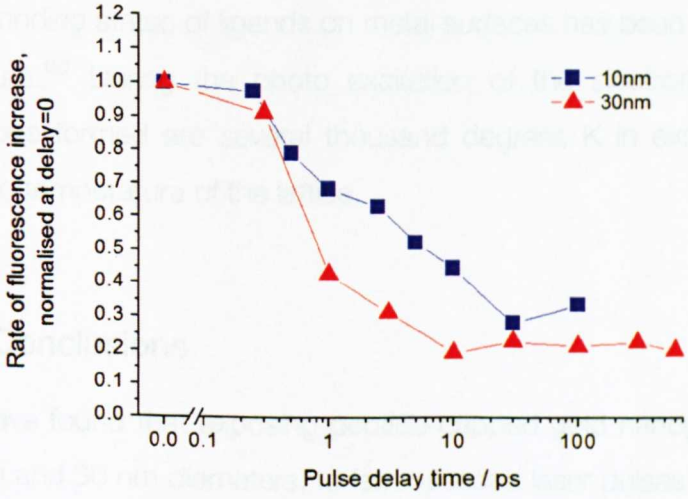

Figure 4.7. Decrease of the rate of fluorescently labelled ligand dissociation as the delay time increases for 10 nm (blue) and 30 nm (red) nanoparticles.

The data is from that presented in Figure 4.5 and 4.8 for 10 nm and 30 nm respectively.

but it depends on the initial temperature of the electrons which increases with pulse energy.[77] Lower pulse energies were used for the 30 nm nanoparticles meaning less heating and therefore a faster electron-phonon relaxation. This is consistent with that seen by Link et al. [1] for the electron-phonon relaxation in gold nanoparticles of approximately 10 nm diameter. This relaxation is independent of nanoparticle size, which is why it is seen in both 10 and 30 nm samples. The cross correlation data for the 30 nm nanoparticles clearly indicates that it is not a hot phonon mediated process that causes the dissociation of the peptide monolayer. The expected result for a phonon mediated process would be to see a decrease in fluorescence on the time scale of the phonon-phonon relaxation time of ~150 ps for a 30 nm gold nanoparticle.[78]

A hot electron-mediated ligand dissociation mechanism including the anti-bonding states of ligands on metal surfaces has been seen in the literature.[152] During the photo excitation of the electrons, the hot electrons formed are several thousand degrees K in excess of the melting temperature of the lattice.

4.3. Conclusions

We have found that exposing peptide-capped gold nanoparticles, of 10 nm and 30 nm diameters, to femtosecond laser pulses causes the dissociation of ligands held to the nanoparticle surface by a gold-

sulfur bond. This desorption is caused by the breaking of the gold-sulfur bond, which was measured by the unquenching of fluorescent ligand as it leaves the gold surface. The experimental results show that this bond breaking is not due to a thermal process where the phonons couple with the gold-sulfur bond's vibrational degrees of freedom causing the bond to break. Instead, the model of a photo-excited electron mediated process, where the hot-electrons cause the gold-sulfur bond to break through DIMET or where nascent electrons are able to occupy an anti-bonding state causing dissociation of ligands is consistent with the data that is seen. The very short cross correlation times that are observed may be due to the peptide that we have used having two cysteines. The peptide having two bonds to the surface makes this more difficult to break since the electrons will have to be significantly hotter in order to have enough energy to break both of these bonds. It is most likely that the CALNN monolayer is removed in larger proportions than the CCALNN fluorophore because of this larger energy requirement. The CCALNN fluorophore would only be able to dissociate at the hottest electron temperatures, which would then quickly dissipate into the phonons.

CHAPTER 5

Conclusions and perspectives

In this work, fundamental properties of ligand-capped nanoparticles have been explored. Whilst there is a some evidence that ligands on the surfaces of nanoparticles organise into domains, we have shown that published data claiming the presence of stripy domains on the surface of nanoparticles is due to scanning artefacts and it is unlikely that ligands organise themselves into stripes. The reported remarkable properties, whilst unusual upon first glance, can be explained in a rational manner. The observed stripes can be attributed to scanning artefacts and the cell uptake is likely to be a property of the cell line used rather than an intrinsic property of the nanoparticles. Our inability to reproduce the published results may be a reason why there are no groups that have published their own studies on these nanoparticles. This chapter also raises questions on the peer-review system where weak or subjective data, such as the published XRD spectra or using a visual scale of one to four to describe a colloid's stability, can be published in prominent scientific journals as strong evidence, but the publication of an article challenging published evidence proves to be an extremely long and difficult process (our still unpublished manuscript has now been under review for over two years).

Ultrafast heating studies have revealed that the release of ligands attached to a nanoparticle surface is mediated by electron driven

processes that opens the potential for nanoparticles as molecular delivery vehicles that can selectively release their cargo upon irradiation on the femtosecond scale. One potential other application of these experiments would be to use the release rate as an indicator of the local environment of the removed peptide. Indeed, preliminary experiments obtained during the course of the collaborative work of a third year Chemistry student project, Laura O'Neill indicates that the structure of peptide monolayers affects the rate at which fluorescent peptides are released from nanoparticles (Laura O'Neill third year report, CHEM366)(figure 5.1). In order to have more qualitative data, a study using a peptide monolayer comprising completely of a CALNN and a CALNN based fluorescent peptide would make allow greater detail to be extracted. If indeed it is confirmed that the dynamics of light-induced ligand release contains insights into their conformation and intermolecular interactions, this line of research could be expanded towards different peptide sequences, and in the first instance the peptides we have characterised in some details by spectroscopic methods.

We have seen strong evidence that CFGAILSS peptide monolayer forms some -sheet structure on the surface of nanoparticles, albeit with a proportion of random coil. This proportion of β–sheet appears to increase as the nanoparticle becomes larger, and exhibits less surface curvature. The formation of structure and controlling ligand interactions is an important step towards nanoparticles with tailored surface topology and functionality. Further studies are however

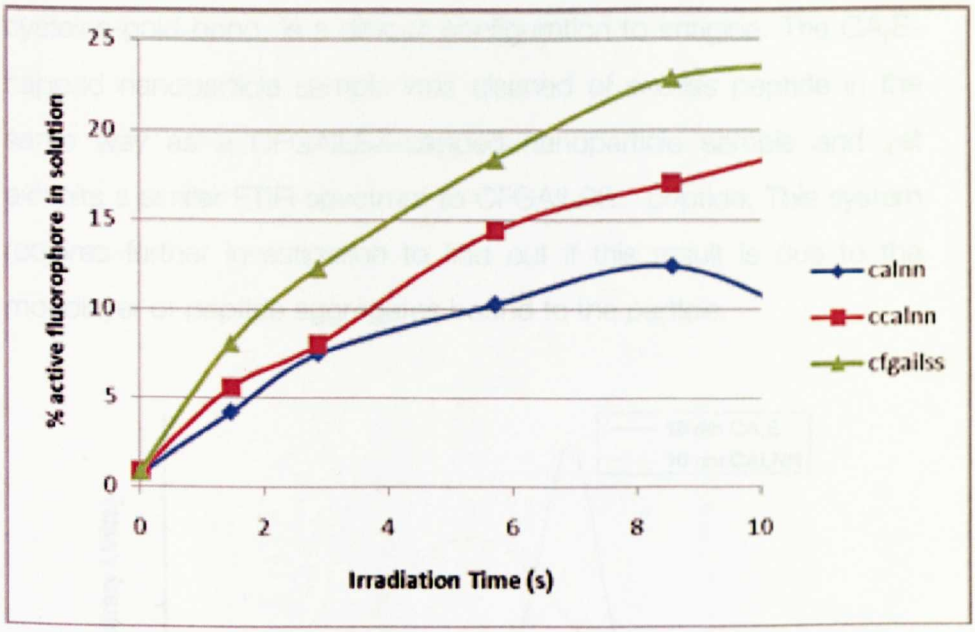

Figure 5.1. Relative fluorescence measurements for 10 nM nanoparticles in water with different peptides used after irradiation by Nd:YAG, 37.5 mJ mJ pulse energy. (Data courtesy of Laura O'Neil)

required to investigate the presence of hydrogen bonding between ligands in mixed as well as homogenous monolayers. Whilst the current data set can provide no more data, further studies using isotopic labels will be able to provide detailed inter molecular distances allowing a more accurate model to be built.

The FTIR spectra of nanoparticles coated with the peptide sequence CA_7E shows the emergence of two sharp amide I bands at 1620 cm-1 and 1680 cm-1 (figure 5.2) indicating the presence of β-sheet. The positions of these bands however are consistent with antiparallel beta-sheet, which with the peptide's forced orientation due the

cysteine-gold bond, is a difficult configuration to imagine. The CA_7E-capped nanoparticle sample was cleaned of excess peptide in the same way as a CFGAILSS-capped nanoparticle sample and yet exhibits a similar FTIR spectrum to CFGAILSS peptide. This system requires further investigation to find out if this result is due to the monolayer or peptide aggregates bound to the particle.

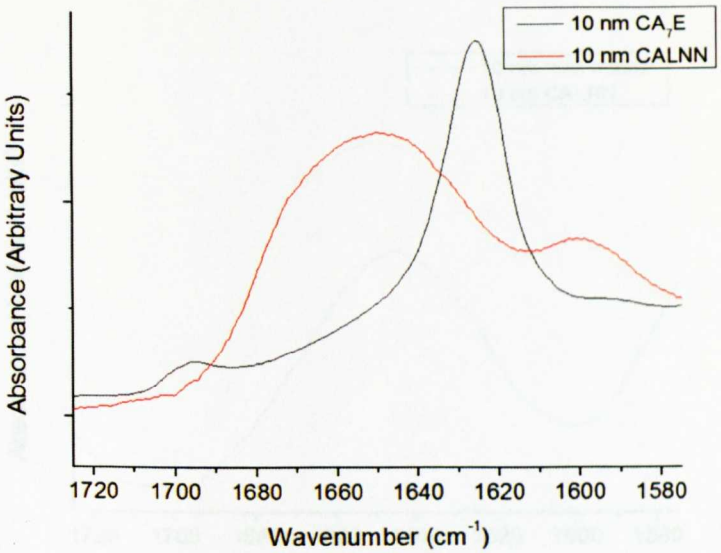

Figure 5.2 FTIR spectra of 10 nm gold nanoparticles capped with CALNN and CA_7E peptides

A prominent feature in all of the presented FTIR spectra is the presence of the COO^- band at 1600 cm^{-1}. The part of the peptide responsible for this is the solution facing C-terminus and is responsible for providing some charge repulsion in keeping the nanoparticle sample stable. Using peptides terminated with an alcohol, or polyethylene group will remove this band from the FTIR spectra and facilitate spectrum deconvolution. These "peptidols" have

been used as part of a mixed monolayer [63] named the "mix matrix". This is comprised of 70 % CVVVT-ol and 30% $HS(CH_2)_4PEG_4$-ol. The lack of a C terminal carbonyl group allow the direct analysis of the amide I band without distortion from the 1600 cm^{-1} carbonyl band (Figure 5.3).

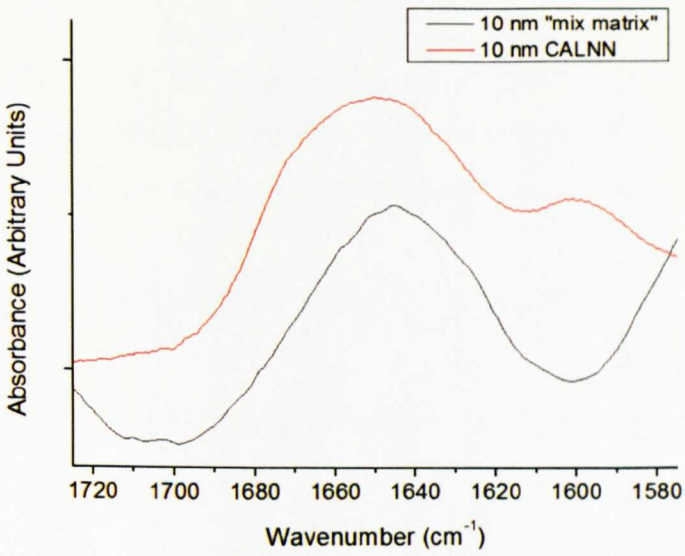

Figure 5.3 FTIR spectra of 10 nm gold nanoparticles capped with CALNN and the "mix matrix" mix of ligands.

In conclusion, elucidating and controlling the structure of ligand monolayers is a difficult challenge, and several techniques must be used in conjunction to obtain meaningful conclusions. Structured monolayers where individual ligands show a particular affinity for other ligands, provide an avenue for controlling surface properties on the nanoscale. What has evolved in nature over billions of years provides

inspiration to advance nanoscale building blocks towards self-organising nanomaterials. With more development these materials have the potential to have a level of programmability to organise via a bottom up approach, into precise objects and assemblies with as much specificity as proteins and other biomolecules.

CHAPTER 6

Materials and methods

6.1 Materials

All peptides were purchased from Peptide Protein Research Ltd (Hampshire) at > 70 % purity.

Tetrachloroaurate ($HAuCl_4$), tannic acid, trisodium citrate, sodium acrylate, dithiothreitol, Mercaptoproprionic acid and Octanethiol were all purchased from Sigma Aldrich at reagent grade quality.

Ethanol was purchased from Fischer at HPLC grade.

Sodium mercaptoundecanesulfonate was purchased from Prochimia, Poland.

Phosphate buffered saline (1x PBS) solution contains 137 mM sodium chloride, 2.7 mM potassium chloride and 10 mM phosphate buffer adjusted to pH 7.2 using HCl or NaOH.

6.2 Gold nanoparticle syntheses

Several different methods of nanoparticles were required during this work. "Stripy" nanoparticles were synthesised according to the literature to ensure the sample was representative of that which has

been published. Trisodium citrate and sodium acrylate was used in conjunction with tannic acid to synthesise nanoparticles of 10 nm diameter. Trisodium citrate was used in chapter 4 and sodium acrylate in chapter 3. Sodium acrylate was used because of its lower number of carbonyl groups since these will mask the carbonyl signal from the peptide backbone. 13 nm diameter trisodium citrate nanoparticles were used as seeds for growing into larger nanoparticles using hydroxyl amine.

6.2.1 Preparation of gold nanoparticles using trisodium citrate

The gold nanoparticles were prepared, according to Turkevich et al. [3], by adding 4 mL of 1% (w/v) sodium citrate solution to a stirred boiling solution of 100 mL of 0.01% (w/v) $HAuCl_4$ and refluxed for 30 minutes. The maximum absorption in ultraviolet-visible spectra (plasmon peak) was approximately 520 nm. The particle size was calculated to using UV/Vis and TEM according to Haiss et al. [8].

6.2.2 Preparation of gold nanoparticles using Sodium Acrylate

Particles were prepared according to Hussain et al. [153]. An aqueous solution of $HAuCl_4$ (50 mL, 1 mM) was refluxed for 5-10 min, and a warm (50-60 °C) aqueous solution of sodium acrylate (15 mL, 80 mM) was added quickly. Reflux was continued for another 30 min until a deep-red solution was observed. The particle solution was filtered

through 0.22 μm Millipore syringe filters to remove any precipitants, and the filtrate was stored at room temperature. Particle size was calculated to be 16 nm using UV/Vis [8] and TEM.

6.2.3 Preparation of gold nanoparticles using trisodium Citrate and tannic acid

Gold nanoparticle synthesis was adapted from reference [120]. All glassware and apparatus cleaned thoroughly with non-ionic detergent, ethanol, and MQ water. To 395 mL of MQ water, 5 mL of 1 % $HAuCl_4$ was added and stirred. The solution was heated to 60 °C. While this was heating, 20 mL of 1 % w/v sodium citrate was added to 78.4 mL of MQ water, and 1.6 mL of 1 % w/v tannic acid. This 100 mL solution was added to the 400 mL and the temperature was raised to 100 °C to complete the reaction. Once cooled the particles were filtered using a 0.22 μm PVDF filter to remove any precipitate. Nanoparticle suspension was stored at 4°C. The resulting particles were 10 nm in diameter with a maximum absorbance at 520 nm. Size distribution was confirmed using TEM.

6.2.4 Preparation of gold nanoparticles using sodium acrylate and tannic acid

All glassware was thoroughly cleaned as described above. 1mL of 1% w/v of $HAuCl_4$ was added to 79 ml of MQ water. This solution was heated to 60°C, whilst a 20 mL reducing solution of 4 mL 1% w/v sodium acrylate, 200 μL tannic acid (1% w/v) and 15.8 mL of MQ

water. Once the gold solution had reached 60°C, the reducing solution was added and the reaction refluxed for 30 minutes to complete. Once cooled, particles were then filtered using 0.22 μm PVDF filters to remove any precipitate. The nanoparticle suspension was stored at 4°C. The resulting particles were found to be 10 nm in diameter using TEM, with a maximum absorbance at 520 nm.

6.2.5 Preparation of gold nanoparticles using small gold nanoparticles as seeds

Nanoparticles were synthesised as described in reference [121]. Trisodium citrate reduced gold nanoparticles were made as described in 6.2.1, and sodium acrylate nanoparticles were synthesised as in 6.2.2. From this synthesis 15 mL was taken and 100 mL of MQ and 1 mL of 2 M Hydroxylamine (NH_2OH) was added, and this was stirred rapidly for 2 minutes. To this rapidly stirring solution 1 mL of 1% $HAuCl_4$ was added slowly added drop wise, and stirred for 10 minutes to form solution A (20 nm diameter). From solution A, 25 mL was taken and 75 mL of MQ and 0.562 mL of NH_2OH was added and stirred for two minutes. Finally, 1 mL of 1 % $HAuCl_4$ was added to this rapidly stirring solution to form solution B (30 nm diameter). The size distribution was determined using TEM.

6.3 Capping of gold nanoparticles

6.3.1 Formation of peptide capped nanoparticles

To 900 μL of gold nanoparticles, 100 μL of 2 mM peptide solution in deionised water or 10x PBS, was added and the particles were incubated over night. In order to remove any excess peptide the particles were either; centrifuged three times, each time removing the supernatant and replacing with MQ water, or run through a Sephadex G25 size exclusion chromatography column. If the CFGAILSS peptide was being used to form a monolayer, the particles were first dried in a rotary evaporator and then sonicated in 150 μL of hexafluoro iso-propanol (HFIP) to dissolve any fibrils that will have assembled during monolayer formation and left overnight again. The sample was then centrifuged and the excess peptide dissolved in HFIP was removed. The particles were then suspended in 0.2 M NaOH and the washing procedure was then continued as normal.

6.3.2 Synthesis of "stripy" nanoparticles

Gold nanoparticles were synthesised according to reference [59]. A saturated solution of $NaBH_4$ in HPLC grade ethanol was made, and left stirring at 4°C for 30 minutes. Meanwhile 12.7 mg of HAuCl4 was dissolved in 18 mL of HPLC grade ethanol and left to stir for 10 minutes at 4°C. For octane thiol capped nanoparticles 5.92 μL of OT was added to the gold salt mixture and left stirring for another 10 minutes. For MUS/OT capped a mixture of MUS and OT was added

to give the following monolayer compositions; for 100 % MUS nanoparticles – 8.6 mg MUS, 67 % MUS nanoparticles – 5.7 mg MUS and 1.96 μL OT, 33 % MUS nanoparticles – 2.9 mg MUS and 2.91 μL OT. These mixtures of MUS and OT in the ethanol solution were left to stir for 4 hours to ensure all MUS had dissolved. To this stirring gold/ligand solution 7 mL of the $NaBH_4$ solution was slowly added drop wise. The solution turned from yellow, to orange, to brown to a very dark brown. This mixture was left for a further two hours stirring to complete the reaction. The reaction was then transferred to the freezer to aid precipitation of the particles. The supernatant was removed, and the particles were resuspended in 10 mL of ethanol 3 times to wash away excess ligand. Particles were stored in ethanol at room temperature.

6.4 Stability of octanethiol-capped nanoparticles

5 mg of 100% OT particles were suspended in 500 μL of THF and left undisturbed for 3 weeks. The concentration of nanoparticles was measured from the absorbance at 506 nm using an extinction coefficient e =3.64 x 10^6 $M^{-1}.cm^{-1}$. The particles were first diluted in order to obtain a suitable absorbance (A_{506} < 2). The extinction coefficient was obtained (as Centrone et al.) from Liu et al.[154]

6.5.1 Fourier Transform Infrared spectroscopy

Peptide samples for FTIR were first left on the bench in 100 mM HCl for 30 minutes to remove residual TFA from peptide synthesis. The

peptide sample was then freeze-dried, resuspended in D_2O for 1 hour and then freeze-dried again to remove H_2O. Samples of peptide-capped nanoparticles were made from 50 mL of particles and 5 mL of 2 mM peptide as described in 2.3.1. Once the monolayer had formed the particles were centrifuged to reduce the volume, and then washed using a 70 mL Saphadex G25 column to remove excess peptide. Following washing, the particles were lyophilised, resuspended in 200 μL of D_2O and then freeze dried again to remove as much water as possible because water absorbs very strongly between 1700 and 1600 cm-1 in an infrared spectrum. The sample was suspended in 50 μL of D2O and loaded into a 50 μL FTIR cell, with a 50 μm PTFE spacer. FTIR spectra were recorded using a BioRad FTS-40 spectrometer with an HgCdTe (MCT) detector. A resolution of 1 cm^{-1} was used throughout and all spectra were averaged over 500 scans. The spectrometer was purged with dry air; any residual water vapour absorption was corrected by subtracting an appropriately scaled spectrum of humid air. Solvent correction was performed by subtracting appropriately scaled spectra of D_2O, measured under the same conditions and at the same temperature as peptide samples.

6.5.2 2D IR spectroscopy

2DIR spectra were measured by P Donaldson of Peter Hamm's group at the University of Zurich. Pump probe and photon echo 2DIR spectra of the amide I band of the nanoparticle samples were collected using calcium fluoride sample cells with 50um pathlength and amide I absorbances ranging from 10-200 mOD. A 300 fs population time was used for all data and all laser pulses were parallel

polarised. Excitation pulses were mainly parallel, however for the photon echo data, polarisation effects were also studied.

6.6 DTT-induced aggregation

A 90 μl solution of 110 mM DTT in PBS was added to 10 μl of nanoparticles, to give a final A_{450} = 0.8, into a 384 well plate. The aggregation parameter (A_{650}/A_{520}) was measured as a function of time to monitor the state of aggregation. The midpoint of the aggregation (AP = 0.7) was taken to compare different particle populations.

6.7 TEM analysis

TEM was performed on a Technai Spirit at 120 kV. 100 mesh TEM grids were prepared by coating with pioloform (polyvinyl butyral). A glass microscope slide was dipped in a 2% w/v pioloform in chloroform solution and left to dry. The resulting film on glass is removed and floated on water. Onto this floating film 100 mesh grids are placed and the film and grids are transferred to another slide, the copper grids in contact with the slide. Grids for study were prepared by drying 5 μl of sample, at room temperature, on a grid.

6.8 Photothermal microscopy

All photothermal microscopy was performed by Yann Cesbron.

The cells were fixed and observed by photothermal heterodyne microscopy. The absorbing beam (523 nm, Nd:YLF frequency

doubled laser) modulated at the frequency w (w/2p= 692.5 kHz) by an acousto-optic modulator and the probe beam (632.8 nm, HeNe laser) were focused on the sample using a Zeiss Achroplan 50X / 0.9 NA oil immersion objective. The beam intensities were 0.44 mW and 10.65 mW respectively. The forward interfering fields were collected with a Zeiss Achroplan 40X / 0.8 NA water dipping objective and sent onto a photodiode. The beat signal at the frequency w was extracted via a lock-in amplifier and integrated over 10 ms. All images were completed by moving the sample with a piezo-electric device (Physik Instrumente) over the fixed laser beams and were taken at the altitude of 1 mm above the glass coverslip surface.

6.9 Cell culture and nanoparticle delivery:

Cell culture work was performed by Dr Paul Free.

HeLa cells were grown in Dulbecco's Modified Eagle's Medium (DMEM) supplemented with 10% FCS (v/v) and 1% non essential amino acids (v/v), at 37°C, 5 % CO_2. Cells (between passages 8 to 20) were plated at 1.10^5 cells/mL. For all experiments, nanoparticles (33% MUS, 66% MUS or 100% MUS) were mixed with the complete medium (containing 10% FCS) and added immediately to the cells. The cells were incubated for 3 hours (37°C, 5 % CO_2) with nanoparticles at a final concentration of 400 nM. The cells were then washed three times with PBS, fixed with 4% paraformaldehyde / PBS (1 mL) for 15 minutes at room temperature, and then washed three

times with PBS before adding ultra-pure water (2 mL). Fixed cells were stored at 4°C until imaged by photothermal microscopy.

6.9 Image processing

The STM images were copied from the articles' pdf (shown as grayscale images in the Figure 2.2a and Figure 2.3a). ImageJ was used for Fast Fourier Transform (FFT) processing. The contrast and brightness of the frequency-filtered images was automatically adjusted. There was no other processing or alteration of the images.

6.10 Solid-state NMR

All Solid state NMR experiments were performed by Dr David Middleton

6.10.1 Solid-state NMR – CP-MAS

CP-MAS NMR experiments were performed with a Bruker Avance 400 spectrometer operating at a magnetic field of 9.3 Tesla. Hydrated fibril or nanoparticle samples were packed into a 4 mm zirconium rotor and rotated at a MAS frequency of between 6 kHz and 13 kHz (± 1 Hz). All experiments utilised an initial 4.0 ms ^{1}H 90° excitation pulse, 1 ms Hartmann-Hahn contact time at a ^{1}H spin-lock field of 65 kHz, 85 kHz TPPM proton decoupling[155] and a 2 s recycle delay.

6.10.2 Solid-state NMR – rotational resonance

Magnetisation exchange was measured at n = 2 rotational resonance (RR) using the constant time pulse sequence described by Balazs and Thompson[156]. The variable time pulse sequence used routinely for RR measurements can give rise to different amounts of heat being absorbed by the gold particles as a result of increasing exposure to high power irradiation (i.e., proton decoupling) in experiments with longer mixing times. Sample heating could affect the measured signal intensities and prevent the accurate measurement of dipolar couplings. In the constant time pulse scheme, the mixing time t_m is varied as normal but the overall duration of proton decoupling (t_c), and hence the heat absorbed by the sample, remains the same in each experiment. As an extra precaution against sample heating the temperature was reduced to -40 °C, which has the further advantage of reducing interference from molecular dynamics.

Magnetisation exchange was measured by adjusting the sample spinning rate (w_R) to the difference between the resonance frequencies (DW_{CC}) of the pair of spins selected (i.e., n = 1 RR) or to half the frequency difference (i.e., n = 2 RR). Measurements at n = 1 RR were not attempted for nanoparticles samples because higher MAS frequencies tended to give rise to frictional heating which severely attenuated the signal. A series of experiments at mixing times t_m of up to 50 ms was performed to measure the time dependence of difference polarisation. Data representing exchange of Zeeman order ("magnetisation exchange curves") were obtained from

the difference in intensities of each pair of peaks. Spectra were processed with 20 Hz exponential line broadening.

6.10.3 Numerical simulations of magnetisation exchange curves.

The internuclear distance (r_{CC}) between the C' and Ca spins of Ala5 at n = 2 RR were determined from numerical simulations of magnetisation exchange curves using a Fortran computer program written specifically for this purpose. Curves were calculated as described elsewhere[118,157] and are a function of the distance-dependent ^{13}C-^{13}C dipolar coupling constant d_{cc} and the zero quantum relaxation time T_2^{ZQ}. Values for ^{13}C chemical shift anisotropy and asymmetry parameters were measured from solid alanine. Simulations took into account the statistical frequency of adjacent peptides in the fibrillar or nanoparticle matrix being labelled the same site and therefore unable to participate in magnetisation exchange. The value of T_2^{ZQ} is not known, but is routinely estimated from the reciprocal sum of the two line widths; in this case, for C' and Ca. A series of curves was calculated for a range of T_2^{ZQ} values in which the upper and lower limits corresponded to half the sum of the line widths and twice the sum of the line widths, respectively. Values of r_{CC} and T_2^{ZQ} were taken from the simulated curves giving the best fit to the upper and lower error limits of the experimental data.

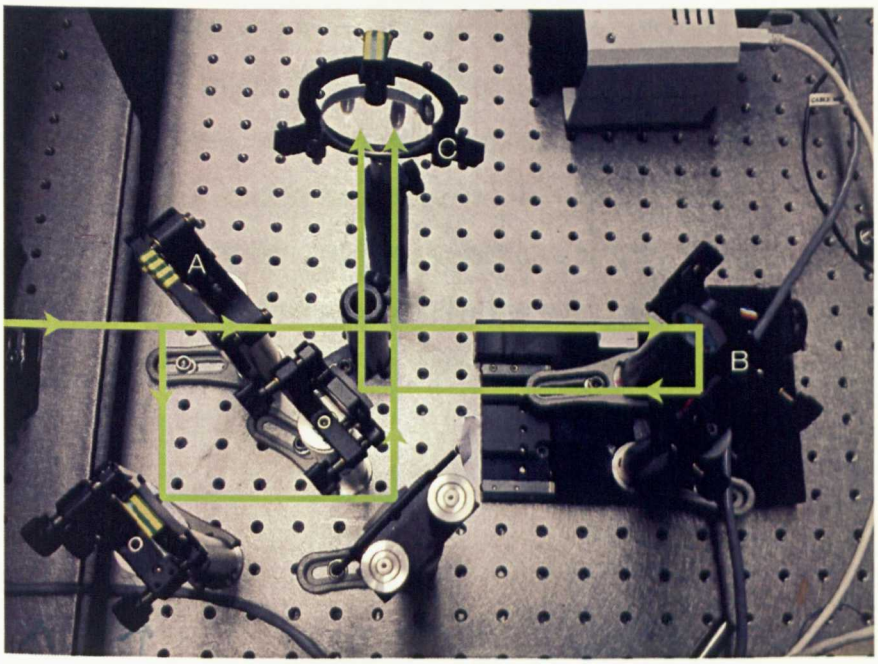

Figure 6.1 Optical table setup used in the ultrafast heating of gold nanoparticles. The laser is first split into two beams by a 50:50 beam splitter (A), a delay is introduced into one of the beams by a variable delay line (B) and both beams are focused onto a 150 μm pinhole, and then the sample, by a lens of 700 mm focal length (C).

6.11.1 Femtosecond laser irradiation

A 150 fs pump laser of 800 nm was fed into an optical parametric amplifier (OPA) splitting the laser photons into two lower energy photons, 1588 nm (signal) and 1714 nm (idler). A sum frequency process between the 800 nm pump laser and the 1588 nm signal photons generates the required 532 nm green laser used. This beam is split in half by a 50:50 beam splitter (Figure 6.1 A) and a variable delay line (Figure 6.1 B) introduces a delay into the one of the beams by increasing the distance the light travels before the two beams go through a lens of 700 mm focal length (Figure 6.1 C). The two beams

are focused first onto a 150 μm pin hole, then onto a quartz cuvette containing 1.2 mL of 95 % CALNN and 5 % CCALNNGGGP-acetoxymethylcoumarin-capped gold nanoparticles. Throughout the experiment the sample was constantly mixed by a magnetic stirrer. The sample irradiation time was calculated as the average irradiation time per nanoparticle accounting for the use of 1.2 mL of sample in a 10 mm^2 cuvette, and a 150 μm laser beam spot size.

APPENDIX

Solid-state nuclear magnetic resonance

Solid state NMR (ssNMR) can provide atomic-level resolution structural information on molecules that are not compatible with other characterisation techniques. This incompatibility may arise from a lack of solubility, an inability to crystalise, or a high molecular weight. [158] [159] The two methods that are responsible for the majority of macromolecule structures that we have today are X-ray crystallography and solution NMR. X-ray crystallography depends on the availability of high-quality crystals and solution NMR is limited to proteins with a molecular weight of 40 kD and a solubility that can allow concentrations in excess of 100 μM. SsNMR is able to provide information on atomic-level interactions.

Just like solution NMR, ssNMR deduces information on the nucleus of atoms. This information is dependent on the chemical environment of the nucleus and is measured by looking at the nucleus' angular momentum or spin. This spin interacts with a magnetic or electric field. These interactions are orientation dependant and consequently, in solids, anisotropic interactions have a significant contribution to the behaviour of these interactions. These anisotropic interactions are averaged out by the tumbling of the molecule and brownian motion in solution NMR.

The samples used in ssNMR often exhibit inhomogeneously broadened lines due to the random orientations of the molecules with respect to the external magnetic field, and not due to structural inhomogeneity. Whilst this broadening can contain useful information (refs 32-43), broad line shapes result in a reduced resolution and sensitivity. To remove this constraint ssNMR experiments are mostly performed using magic angle spinning (MAS). In MAS the sample is rapidly spun at the magic angle to the external magnetic field, approximately 54.7. At the magic angle anisotropic interactions average to zero, and when the MAS rotation frequency exceeds the inhomogeneous line width, the inhomogeneously broadened lines are reduced to sharper lines. The residual line width is often more indicative of structural inhomogeneity, dipole-dipole couplings, magnetic susceptibility effects (knight shift) [160] or transverse nuclear spin relaxation. When this spinning frequency matches the exact frequency difference between two spin systems of interest these are said to be in rotational resonance (RR). Maximum exchange of magnetisation between 2 spins/labelled sites will occur when the RR condition is exact, and the strongest coupling is observed when there is maximum magnetisation exchange. It is not always possible to spin at this RR condition and mixing time can be altered to overcome any off resonances that may occur. Mixing time refers to the length of time that the spins are allowed to evolve in the y-plane following the application of a 90 pulse to flip them there. A longer mixing time will result in less coupling than a shorter mixing time because the of the magnetisation dispersing over time (and becoming off resonance), shorter mixing times can therefore result in an increase in intensity.

BLANK PAGE
IN
ORIGINAL

BIBLIOGRAPHY

1 Link, S. & El-Sayed, M. A. Spectral properties and relaxation dynamics of surface plasmon electronic oscillations in gold and silver nanodots and nanorods. Journal of Physical Chemistry B 103, 8410-8426 (1999).

2 Wiley, B., Sun, Y. G., Mayers, B. & Xia, Y. N. Shape-controlled synthesis of metal nanostructures: The case of silver. Chemistry-a European Journal 11, 454-463, doi:10.1002/chem.200400927 (2005).

3 Turkevich, J., Stevenson, P. C. & Hillier, J. A STUDY OF THE NUCLEATION AND GROWTH PROCESSES IN THE SYNTHESIS OF COLLOIDAL GOLD. Discussions of the Faraday Society, 55-& (1951).

4 McConnell, W. P. et al. Electronic and optical properties of chemically modified metal nanoparticles and molecularly bridged nanoparticle arrays. Journal of Physical Chemistry B 104, 8925-8930 (2000).

5 Kelly, K. L., Coronado, E., Zhao, L. L. & Schatz, G. C. The optical properties of metal nanoparticles: The influence of size, shape, and dielectric environment. Journal of Physical Chemistry B 107, 668-677, doi:10.1021/jp026731y (2003).

PAGE NUMBERING AS IN THE ORIGINAL THESIS

6 Link, S. & Ei-Sayed, M. A. Optical properties and ultrafast dynamics of metallic nanocrystals. Annual Review of Physical Chemistry 54, 331-366, doi:10.1146/annurev.physchem.54.011002.103759 (2003).

7 Aiken, J. D. & Finke, R. G. A review of modern transition-metal nanoclusters: their synthesis, characterization, and applications in catalysis. Journal of Molecular Catalysis a-Chemical 145, 1-44 (1999).

8 Haiss, W., Thanh, N. T. K., Aveyard, J. & Fernig, D. G. Determination of size and concentration of gold nanoparticles from UV-Vis spectra. Analytical Chemistry 79, 4215-4221, doi:10.1021/ac0702084 (2007).

9 Mirkin, C. A., Letsinger, R. L., Mucic, R. C. & Storhoff, J. J. A DNA-based method for rationally assembling nanoparticles into macroscopic materials. Nature 382, 607-609 (1996).

10 Sharma, J., Chhabra, R., Liu, Y., Ke, Y. G. & Yan, H. DNA-templated self-assembly of two-dimensional and periodical gold nanoparticle arrays. Angewandte Chemie-International Edition 45, 730-735, doi:10.1002/anie.200503208 (2006).

11 Storhofff, J. J., Elghanian, R., Mirkin, C. A. & Letsinger, R. L. Sequence-dependent stability of DNA-modified gold nanoparticles. Langmuir 18, 6666-6670, doi:10.1021/la0202428 (2002).

12 Duchesne, L., Wells, G., Fernig, D. G., Harris, S. A. & Levy, R. Supramolecular domains in mixed peptide self-assembled

monolayers on gold nanoparticles. Chembiochem 9, 2127-2134, doi:10.1002/cbic.200800326 (2008).

13 Levy, R. Peptide-capped gold nanoparticles: Towards artificial proteins. Chembiochem 7, 1141-1145, doi:10.1002/cbic.200600129 (2006).

14 Wang, Z., Levy, R., Fernig, D. G. & Brust, M. The peptide route to multifunctional gold nanoparticles. Bioconjugate Chemistry 16, 497-500, doi:10.1021/bc0500471 (2005).

15 Caseri, W. Nanocomposites of polymers and metals or semiconductors: Historical background and optical properties. Macromol. Rapid Commun. 21, 705-722, doi:10.1002/1521-3927(20000701)21:11<705::aid-marc705>3.0.co;2-3 (2000).

16 Brust, M., Walker, M., Bethell, D., Schiffrin, D. J. & Whyman, R. SYNTHESIS OF THIOL-DERIVATIZED GOLD NANOPARTICLES IN A 2-PHASE LIQUID-LIQUID SYSTEM. J. Chem. Soc.-Chem. Commun., 801-802, doi:10.1039/c39940000801 (1994).

17 Otsuka, H., Nagasaki, Y. & Kataoka, K. PEGylated nanoparticles for biological and pharmaceutical applications. Adv. Drug Deliv. Rev. 55, 403-419, doi:10.1016/s0169-409x(02)00226-0 (2003).

18 Weare, W. W., Reed, S. M., Warner, M. G. & Hutchison, J. E. Improved synthesis of small (d(CORE) approximate to 1.5 nm) phosphine-stabilized gold nanoparticles. Journal of the

American Chemical Society 122, 12890-12891, doi:10.1021/ja002673n (2000).

19 Wang, Y., Neyman, A., Arkhangelsky, E., Gitis, V., Meshi, L., Weinstock, IA. Self-Assembly and Structure of Directly Imaged Inorganic-Anion Monolayers on a Gold Nanoparticle Journal of the American Chemical Society 131, 17412-17422, doi:10.1021/ja907815d (2009).

20 Free, P., Shaw, C. P. & Levy, R. PEGylation modulates the interfacial kinetics of proteases on peptide-capped gold nanoparticles. Chemical Communications, 5009-5011, doi:10.1039/b910657j (2009).

21 Schaeffer, N. et al. Fluorescent or not? Size-dependent fluorescence switching for polymer-stabilized gold clusters in the 1.1-1.7 nm size range. Chemical Communications, 3986-3988, doi:10.1039/b809876j (2008).

22 West, J. L. & Halas, N. J. Engineered nanomaterials for biophotonics applications: Improving sensing, imaging, and therapeutics. Annu. Rev. Biomed. Eng. 5, 285-292, doi:10.1146/annurev.bioeng.5.011303.120723 (2003).

23 Bates, A. D. & Maxwell, A. Energy coupling in type II topoisomerases: Why do they hydrolyze ATP? Biochemistry 46, 7929-7941, doi:10.1021/bi700789g (2007).

24 Bedford, L., Paine, S., Sheppard, P. W., Mayer, R. J. & Roelofs, J. Assembly, structure, and function of the 26S

proteasome. Trends Cell Biol 20, 391-401, doi:S0962-8924(10)00073-5 [pii]10.1016/j.tcb.2010.03.007 (2010).

25 Kuzuya, A. & Komiyama, M. DNA origami: Fold, stick, and beyond. Nanoscale 2, 310-322, doi:10.1039/b9nr00246d (2010).

26 Jones, S. & Thornton, J. M. Principles of protein-protein interactions. Proceedings of the National Academy of Sciences of the United States of America 93, 13-20 (1996).

27 Gazit, E. Self-assembled peptide nanostructures: the design of molecular building blocks and their technological utilization. Chemical Society Reviews 36, 1263-1269, doi:10.1039/b605536m (2007).

28 Meakin, P. AGGREGATION KINETICS. Physica Scripta 46, 295-331 (1992).

29 Enustun, B. V. & Turkevich, J. COAGULATION OF COLLOIDAL GOLD. Journal of the American Chemical Society 85, 3317-& (1963).

30 Lin, S., Li, M., Dujardin, E., Girard, C. & Mann, S. One-dimensional plasmon coupling by facile self-assembly of gold nanoparticles into branched chain networks. Advanced Materials 17, 2553-+, doi:10.1002/adma.200500828 (2005).

31 Wang, S. T., Yan, J. C. & Chen, L. Formation of gold nanoparticles and self-assembly into dimer and trimer aggregates. Materials Letters 59, 1383-1386, doi:10.1016/j.matlet.2004.12.045 (2005).

32 Boal, A. K. et al. Self-assembly of nanoparticles into structured spherical and network aggregates. Nature 404, 746-748 (2000).

33 Davis, S. A., Breulmann, M., Rhodes, K. H., Zhang, B. & Mann, S. Template-directed assembly using nanoparticle building blocks: A nanotectonic approach to organized materials. Chemistry of Materials 13, 3218-3226, doi:10.1021/cm011068w (2001).

34 Chen, C. L., Zhang, P. J. & Rosi, N. L. A new peptide-based method for the design and synthesis of nanoparticle superstructures: Construction of highly ordered gold nanoparticle double helices. Journal of the American Chemical Society 130, 13555-+, doi:10.1021/ja805683r (2008).

35 Mastroianni, A. J., Claridge, S. A. & Alivisatos, A. P. Pyramidal and Chiral Groupings of Gold Nanocrystals Assembled Using DNA Scaffolds. Journal of the American Chemical Society 131, 8455-8459, doi:10.1021/ja808570g (2009).

36 Sardar, R. & Shumaker-Parry, J. S. Asymmetrically functionalized gold nanoparticles organized in one-dimensional chains. Nano Letters 8, 731-736, doi:10.1021/nl073154m (2008).

37 Yan, B., Boriskina, S. V. & Reinhard, B. M. Optimizing Gold Nanoparticle Cluster Configurations (n <= 7) for Array Applications. Journal of Physical Chemistry C 115, 4578-4583, doi:10.1021/jp112146d (2011).

38 Sung, K. M., Mosley, D. W., Peelle, B. R., Zhang, S. G. & Jacobson, J. M. Synthesis of monofunctionalized gold nanoparticles by Fmoc solid-phase reactions. Journal of the American Chemical Society 126, 5064-5065, doi:10.1021/ja049578p (2004).

39 Levy, R. et al. A generic approach to monofunctionalized protein-like gold nanoparticles based on immobilized metal ion affinity chromatography. Chembiochem 7, 592-594, doi:10.1002/cbic.200500457 (2006).

40 Boal, A. K. & Rotello, V. M. Fabrication and self-optimization of multivalent receptors on nanoparticle scaffolds. Journal of the American Chemical Society 122, 734-735 (2000).

41 Tseng, C. H., Tambe, M. J., Lim, S. K., Smith, M. J. & Gradecak, S. Position controlled nanowire growth through Au nanoparticles synthesized by galvanic reaction. Nanotechnology 21, doi:10.1088/0957-4484/21/16/165605 (2010).

42 Zhang, Z. L. & Glotzer, S. C. Self-assembly of patchy particles. Nano Letters 4, 1407-1413, doi:10.1021/nl0493500 (2004).

43 Glotzer, S. C. & Solomon, M. J. Anisotropy of building blocks and their assembly into complex structures. Nature Materials 6, 557-562, doi:10.1038/nmat1949 (2007).

44 Barnes, W. L., Dereux, A. & Ebbesen, T. W. Surface plasmon subwavelength optics. Nature 424, 824-830, doi:10.1038/nature01937 (2003).

45 Tsunoyama, H. & Tsukuda, T. Magic Numbers of Gold Clusters Stabilized by PVP. Journal of the American Chemical Society 131, 18216-+, doi:10.1021/ja908188f (2009).

46 Jadzinsky, P. D., Calero, G., Ackerson, C. J., Bushnell, D. A. & Kornberg, R. D. Structure of a thiol monolayer-protected gold nanoparticle at 1.1 angstrom resolution. Science 318, 430-433, doi:10.1126/science.1148624 (2007).

47 Badia, A. et al. Structure and chain dynamics of alkanethiol-capped gold colloids. Langmuir 12, 1262-1269 (1996).

48 van Delden, R. A. et al. Unidirectional molecular motor on a gold surface. Nature 437, 1337-1340, doi:10.1038/nature04127 (2005).

49 Love, J. C., Estroff, L. A., Kriebel, J. K., Nuzzo, R. G. & Whitesides, G. M. Self-assembled monolayers of thiolates on metals as a form of nanotechnology. Chemical Reviews 105, 1103-1169, doi:10.1021/cr0300789 (2005).

50 Di Felice, R. & Selloni, A. Adsorption modes of cysteine on Au(111): Thiolate, amino-thiolate, disulfide. Journal of Chemical Physics 120, 4906-4914, doi:10.1063/1.1645789 (2004).

51 Butt, H. J., Seifert, K. & Bamberg, E. IMAGING MOLECULAR DEFECTS IN ALKANETHIOL MONOLAYERS WITH AN ATOMIC-FORCE MICROSCOPE. Journal of Physical Chemistry 97, 7316-7320 (1993).

52 Folkers, J. P., Laibinis, P. E. & Whitesides, G. M. SELF-ASSEMBLED MONOLAYERS OF ALKANETHIOLS ON GOLD

- COMPARISONS OF MONOLAYERS CONTAINING MIXTURES OF SHORT-CHAIN AND LONG-CHAIN CONSTITUENTS WITH CH3 AND CH2OH TERMINAL GROUPS. Langmuir 8, 1330-1341 (1992).

53 Hostetler, M. J., Templeton, A. C. & Murray, R. W. Dynamics of place-exchange reactions on monolayer-protected gold cluster molecules. Langmuir 15, 3782-3789 (1999).

54 Shaw, C. P., Fernig, D.G., Levy, R. Gold nanoparticles as advanced building blocks for nanoscale self-assembled systems Journal of Materials Chemistry 21, 12181-12187 (2011).

55 Gentilini, C. et al. Formation of Patches on 3D SAMs Driven by Thiols with Immiscible Chains Observed by ESR Spectroscopy. Angewandte Chemie-International Edition 48, 3060-3064, doi:10.1002/anie.200805321 (2009).

56 Takiue, T. & Vollhardt, D. Miscibility of alkanol and fluoroalkanol in Langmuir film at the air/water interface. Colloids and Surfaces a-Physicochemical and Engineering Aspects 198, 797-804 (2002).

57 Stahler, K., Selb, J. & Candau, F. A study of multicompartment polymeric micelles. Materials Science & Engineering C-Biomimetic and Supramolecular Systems 10, 171-178 (1999).

58 Elbert, R., Folda, T. & Ringsdorf, H. SATURATED AND POLYMERIZABLE AMPHIPHILES WITH FLUOROCARBON CHAINS - INVESTIGATION IN MONOLAYERS AND

LIPOSOMES. Journal of the American Chemical Society 106, 7687-7692 (1984).

59 Jackson, A. M., Myerson, J. W. & Stellacci, F. Spontaneous assembly of subnanometre-ordered domains in the ligand shell of monolayer-protected nanoparticles. Nature Materials 3, 330-336 (2004).

60 Hainfeld, J. F. A SMALL GOLD-CONJUGATED ANTIBODY LABEL - IMPROVED RESOLUTION FOR ELECTRON-MICROSCOPY. Science 236, 450-453 (1987).

61 Lata, S., Reichel, A., Brock, R., Tampe, R. & Piehler, J. High-affinity adaptors for switchable recognition of histidine-tagged proteins. Journal of the American Chemical Society 127, 10205-10215, doi:10.1021/ja050690c (2005).

62 Tinazli, A. et al. High-affinity chelator thiols for switchable and oriented immobilization of histidine-tagged proteins: A generic platform for protein chip technologies. Chemistry-a European Journal 11, 5249-5259, doi:10.1002/chem.200500154 (2005).

63 Duchesne, L., Gentili, D., Comes-Franchini, M. & Fernig, D. G. Robust Ligand Shells for Biological Applications of Gold Nanoparticles. Langmuir 24, 13572-13580, doi:10.1021/la802876u (2008).

64 Bruning, M. et al. Bipartite Design of a Self-Fibrillating Protein Copolymer with Nanopatterned Peptide Display Capabilities. Nano Letters 10, 4533-4537, doi:10.1021/nl1024886 (2010).

65 Zou, J. H., Dai, Q., Wang, J. H., Liu, X. & Huo, Q. Solid phase monofunctionalization of gold nanoparticles using ionic exchange resin as polymer support. Journal of Nanoscience and Nanotechnology 7, 2382-2388, doi:10.1166/jnn.2007.424 (2007).

66 Kane, R. S., Takayama, S., Ostuni, E., Ingber, D. E. & Whitesides, G. M. Patterning proteins and cells using soft lithography. Biomaterials 20, 2363-2376 (1999).

67 Mrksich, M. & Whitesides, G. M. Using self-assembled monolayers to understand the interactions of man-made surfaces with proteins and cells. Annual Review of Biophysics and Biomolecular Structure 25, 55-78 (1996).

68 Xia, Y. N. & Whitesides, G. M. Soft lithography. Annual Review of Materials Science 28, 153-184 (1998).

69 Piner, R. D., Zhu, J., Xu, F., Hong, S. H. & Mirkin, C. A. "Dip-pen" nanolithography. Science 283, 661-663 (1999).

70 Rosi, N. L. & Mirkin, C. A. Nanostructures in biodiagnostics. Chemical Reviews 105, 1547-1562, doi:10.1021/cr030067f (2005).

71 Gao, J. X., Bender, C. M. & Murphy, C. J. Dependence of the gold nanorod aspect ratio on the nature of the directing surfactant in aqueous solution. Langmuir 19, 9065-9070, doi:10.1021/la034919i (2003).

72 Xu, X. Y., Rosi, N. L., Wang, Y. H., Huo, F. W. & Mirkin, C. A. Asymmetric functionalization of gold nanoparticles with

oligonucleotides. Journal of the American Chemical Society 128, 9286-9287, doi:10.1021/ja061980b (2006).

73 Pradhan, S., Xu, L. P. & Chen, S. W. Janus nanoparticles by interfacial engineering. Advanced Functional Materials 17, 2385-2392, doi:10.1002/adfm.200601034 (2007).

74 Norgaard, K., Weygand, M. J., Kjaer, K., Brust, M. & Bjornholm, T. Adaptive chemistry of bifunctional gold nanoparticles at the air/water interface. A synchrotron X-ray study of giant amphiphiles. Faraday Discussions 125, 221-233, doi:10.1039/b303117a (2004).

75 Chen, C. L. & Rosi, N. L. Preparation of Unique 1-D Nanoparticle Superstructures and Tailoring their Structural Features. Journal of the American Chemical Society 132, 6902-+, doi:10.1021/ja102000g (2010).

76 Ionita, P., Volkov, A., Jeschke, G. & Chechik, V. Lateral diffusion of thiol ligands on the surface of Au nanoparticles: An electron paramagnetic resonance study. Analytical Chemistry 80, 95-106, doi:10.1021/ac071266s (2008).

77 Jain, P. K., Qian, W. & El-Sayed, M. A. Ultrafast cooling of photoexcited electrons in gold nanoparticle-thiolated DNA conjugates involves the dissociation of the gold-thiol bond. Journal of the American Chemical Society 128, 2426-2433, doi:10.1021/ja056769z (2006).

78 Hu, M. & Hartland, G. V. Heat dissipation for Au particles in aqueous solution: Relaxation time versus size. Journal of

Physical Chemistry B 106, 7029-7033, doi:10.1021/jp020581+ (2002).

79 Mohamed, M. B., Ahmadi, T. S., Link, S., Braun, M. & El-Sayed, M. A. Hot electron and phonon dynamics of gold nanoparticles embedded in a gel matrix. Chem. Phys. Lett. 343, 55-63, doi:10.1016/s0009-2614(01)00653-4 (2001).

80 See, V. et al. Cathepsin L Digestion of Nanobioconjugates upon Endocytosis. Acs Nano 3, 2461-2468, doi:10.1021/nn9006994 (2009).

81 Weeraman, C., Yatawara, A. K., Bordenyuk, A. N. & Benderskii, A. V. Effect of nanoscale geometry on molecular conformation: Vibrational sum-frequency generation of alkanethiols on gold nanoparticles. Journal of the American Chemical Society 128, 14244-14245, doi:10.1021/ja065756y (2006).

82 Braig, K. et al. THE CRYSTAL-STRUCTURE OF THE BACTERIAL CHAPERONIN GROEL AT 2.8-ANGSTROM. Nature 371, 578-586, doi:10.1038/371578a0 (1994).

83 Hostetler, M. J. et al. Alkanethiolate gold cluster molecules with core diameters from 1.5 to 5.2 nm: Core and monolayer properties as a function of core size. Langmuir 14, 17-30, doi:10.1021/la970588w (1998).

84 Jackson, A. M., Hu, Y., Silva, P. J. & Stellacci, F. From homoligand- to mixed-ligand-monolayer-protected metal nanoparticles: A scanning tunneling microscopy investigation.

Journal of the American Chemical Society 128, 11135-11149 (2006).

85 Centrone, A., Hu, Y., Jackson, A. M., Zerbi, G. & Stellacci, F. Phase separation on mixed-monolayer-protected metal nanoparticles: A study by infrared spectroscopy and scanning tunneling microscopy. Small 3, 814-817 (2007).

86 DeVries, G. A. et al. Divalent metal nanoparticles. Science 315, 358-361 (2007).

87 Singh, C. et al. Entropy-mediated patterning of surfactant-coated nanoparticles and surfaces. Physical Review Letters 99, 226106 (2007).

88 Carney, R. P. et al. Size limitations for the formation of ordered striped nanoparticles. Journal of the American Chemical Society 130, 798-799 (2008).

89 Centrone, A. et al. The role of nanostructure in the wetting behavior of mixed-monolayer-protected metal nanoparticles. Proceedings of the National Academy of Sciences of the United States of America 105, 9886-9891 (2008).

90 DeVries, G. A., Talley, F. R., Carney, R. P. & Stellacci, F. Thermodynamic Study of the Reactivity of the Two Topological Point Defects Present in Mixed Self-Assembled Monolayers on Gold Nanoparticles. Advanced Materials 20, 4243-4247 (2008).

91 Hu, Y., Uzun, O., Dubois, C. & Stellacci, F. Effect of ligand shell structure on the interaction between monolayer-protected gold

nanoparticles. Journal of Physical Chemistry C 112, 6279-6284 (2008).

92 Uzun, O. et al. Water-soluble amphiphilic gold nanoparticles with structured ligand shells. Chemical Communications, 196-198 (2008).

93 Verma, A. et al. Surface-structure-regulated cell-membrane penetration by monolayer-protected nanoparticles. Nature Materials 7, 588-595 (2008).

94 Hu, Y., Wunsch, B. H., Sahni, S. & Stellacci, F. Statistical Analysis of Scanning Tunneling Microscopy Images of 'Striped' Mixed Monolayer Protected Gold Nanoparticles Journal of Scanning Probe Microscopy 4, 24 (2009).

95 Kuna, J. K. et al. The effect of nanometre-scale structure on interfacial energy. Nature Materials 8, 837-842 (2009).

96 Billinge, S. J. L. & Levin, I. The problem with determining atomic structure at the nanoscale. Science 316, 561-565, doi:10.1126/science.1135080 (2007).

97 Manea, F., Houillon, F. B., Pasquato, L. & Scrimin, P. Nanozymes: Gold-nanoparticle-based transphosphorylation catalysts. Angewandte Chemie-International Edition 43, 6165-6169, doi:10.1002/anie.200460649 (2004).

98 Nel, A. E. et al. Understanding biophysicochemical interactions at the nano-bio interface. Nature Materials 8, 543-557, doi:10.1038/nmat2442 (2009).

99 Shaheen, U., Cesbron, Y. & Levy, R. Toxin assisted intracellular delivery of gold nanoparticles. Drug Discovery Today 15, 1099-1099, doi:10.1016/j.drudis.2010.09.401 (2010).

100 Nativo, P., Prior, I. A. & Brust, M. Uptake and intracellular fate of surface-modified gold nanoparticles. Acs Nano 2, 1639-1644, doi:10.1021/nn800330a (2008).

101 Rosi, N. L. et al. Oligonucleotide-modified gold nanoparticles for intracellular gene regulation. Science 312, 1027-1030, doi:10.1126/science.1125559 (2006).

102 Russ. The Image Processing and Measurement Cookbook. (1992).

103 Howland. A PRACTICAL GUIDE TO SCANNING PROBE MICROSCOPY. web.mit.edu/cortiz/www/AFMGallery/PracticalGuide.pdf.

104 Jung, J. H., Lee, S. S. & Kaneda, T. Inclusion complexation of cyclodextrins with polyglycol in mixed guest systems. Korea Polym. J. 7, 377-381 (1999).

105 Piehler, J., Brecht, A., Valiokas, R., Liedberg, B. & Gauglitz, G. A high-density poly(ethylene glycol) polymer brush for immobilization on glass-type surfaces. Biosens. Bioelectron. 15, 473-481, doi:10.1016/s0956-5663(00)00104-4 (2000).

106 Suh, K. Y., Seong, J., Khademhosseini, A., Laibinis, P. E. & Langer, R. A simple soft lithographic route to fabrication of poly(ethylene glycol) microstructures for protein and cell

patterning. Biomaterials 25, 557-563, doi:10.1016/s0142-9612(03)00543-x (2004).

107 Wagner, V. E., Koberstein, J. T. & Bryers, J. D. Protein and bacterial fouling characteristics of peptide and antibody decorated surfaces of PEG-poly(acrylic acid) co-polymers. Biomaterials 25, 2247-2263, doi:10.1016/j.biomaterials.2003.09.020 (2004).

108 Kuehner, D. E. et al. Lysozyme net charge and ion binding in concentrated aqueous electrolyte solutions. Journal of Physical Chemistry B 103, 1368-1374, doi:10.1021/jp983852i (1999).

109 Han, G. et al. Controlled recovery of the transcription of nanoparticle-bound DNA by intracellular concentrations of glutathione. Bioconjugate Chemistry 16, 1356-1359, doi:10.1021/bc050173j (2005).

110 Imai, J., Hasegawa, H., Maruya, M., Koyasu, S. & Yahara, I. Exogenous antigens are processed through the endoplasmic reticulum-associated degradation (ERAD) in cross-presentation by dendritic cells. International Immunology 17, 45-53, doi:10.1093/intimm/dxh184 (2005).

111 Berciaud, S., Cognet, L., Blab, G. A. & Lounis, B. Photothermal heterodyne imaging of individual nonfluorescent nanoclusters and nanocrystals. Physical Review Letters 93, 257402 (2004).

112 Boyer, D., Tamarat, P., Maali, A., Lounis, B. & Orrit, M. Photothermal imaging of nanometer-sized metal particles among scatterers. Science 297, 1160-1163 (2002).

113 Cognet, L. et al. Single metallic nanoparticle imaging for protein detection in cells. Proceedings of the National Academy of Sciences of the United States of America 100, 11350-11355 (2003).

114 Levy, R. et al. Rational and combinatorial design of peptide capping Ligands for gold nanoparticles. Journal of the American Chemical Society 126, 10076-10084, doi:10.1021/ja0487269 (2004).

115 Irvine, G. B., El-Agnaf, O. M., Shankar, G. M. & Walsh, D. M. Protein aggregation in the brain: The molecular basis for Alzheimer's and Parkinson's diseases. Molecular Medicine 14, 451-464, doi:10.2119/2007-00100.Irvine (2008).

116 Ferreira, S. T., Vieira, M. N. N. & De Felice, F. G. Soluble protein oligomers as emerging toxins in Alzheimer's and other amyloid diseases. IUBMB Life 59, 332-345, doi:10.1080/15216540701283882 (2007).

117 Tenidis, K. et al. Identification of a penta- and hexapeptide of islet amyloid polypeptide (IAPP) with amyloidogenic and cytotoxic properties. Journal of Molecular Biology 295, 1055-1071, doi:10.1006/jmbi.1999.3422 (2000).

118 Madine, J. et al. Structural Insights into the Polymorphism of Amyloid-Like Fibrils Formed by Region 20-29 of Amylin

Revealed by Solid-State NMR and X-ray Fiber Diffraction. Journal of the American Chemical Society 130, 14990-15001, doi:10.1021/ja802483d (2008).

119 Haggqvist, B. et al. Medin: An integral fragment of aortic smooth muscle cell-produced lactadherin forms the most common human amyloid. Proceedings of the National Academy of Sciences of the United States of America 96, 8669-8674, doi:10.1073/pnas.96.15.8669 (1999).

120 Muhlpfordt, H. THE PREPARATION OF COLLOIDAL GOLD PARTICLES USING TANNIC-ACID AS AN ADDITIONAL REDUCING AGENT. Experientia 38, 1127-1128 (1982).

121 Brown, K. R. & Natan, M. J. Hydroxylamine seeding of colloidal Au nanoparticles in solution and on surfaces. Langmuir 14, 726-728 (1998).

122 Barth, A. Infrared spectroscopy of proteins. Biochimica Et Biophysica Acta-Bioenergetics 1767, 1073-1101, doi:10.1016/j.bbabio.2007.06.004 (2007).

123 Haris, P. I. & Chapman, D. THE CONFORMATIONAL-ANALYSIS OF PEPTIDES USING FOURIER-TRANSFORM IR SPECTROSCOPY. Biopolymers 37, 251-263, doi:10.1002/bip.360370404 (1995).

124 Chirgadze, Y. N. & Nevskaya, N. A. INFRARED-SPECTRA AND RESONANCE INTERACTION OF AMIDE-ONE VIBRATION OF PARALLEL-CHAIN PLEATED SHEET.

Biopolymers 15, 627-636, doi:10.1002/bip.1976.360150403 (1976).

125 Krimm, S. & Abe, Y. INTERMOLECULAR INTERACTION EFFECTS IN AMIDE I VIBRATIONS OF BETA POLYPEPTIDES. Proceedings of the National Academy of Sciences of the United States of America 69, 2788-2792, doi:10.1073/pnas.69.10.2788 (1972).

126 Sheppard, N. & Erkelens, J. VIBRATIONAL-SPECTRA OF SPECIES ADSORBED ON SURFACES - FORMS OF VIBRATIONS AND SELECTION-RULES FOR REGULAR ARRAYS OF ADSORBED SPECIES. Applied Spectroscopy 38, 471-485, doi:10.1366/0003702844555133 (1984).

127 Greenler, R. G., Snider, D. R., Witt, D. & Sorbello, R. S. THE METAL-SURFACE SELECTION RULE FOR INFRARED-SPECTRA OF MOLECULES ADSORBED ON SMALL METAL PARTICLES. Surface Science 118, 415-428, doi:10.1016/0039-6028(82)90197-2 (1982).

128 Lee, S. J., Han, W.H., Kim, K. Perfluorocarbon-stabilized silver nanoparticles manufactured from layered silver carboxylates. Chemcomm, 442-443 (2002).

129 Barth, A. & Zscherp, C. What vibrations tell us about proteins. Quarterly Reviews of Biophysics 35, 369-430, doi:10.1017/s0033583502003815 (2002).

130 Barth, A. Selective monitoring of 3 out of 50,000 protein vibrations. Biopolymers 67, 237-241, doi:10.1002/bip.10085 (2002).

131 Jackson, M. & Mantsch, H. H. THE USE AND MISUSE OF FTIR SPECTROSCOPY IN THE DETERMINATION OF PROTEIN-STRUCTURE. Critical Reviews in Biochemistry and Molecular Biology 30, 95-120, doi:10.3109/10409239509085140 (1995).

132 Surewicz, W. K., Mantsch, H. H. & Chapman, D. DETERMINATION OF PROTEIN SECONDARY STRUCTURE BY FOURIER-TRANSFORM INFRARED-SPECTROSCOPY - A CRITICAL-ASSESSMENT. Biochemistry 32, 389-394, doi:10.1021/bi00053a001 (1993).

133 Cheatum, C. M., Tokmakoff, A. & Knoester, J. Signatures of beta-sheet secondary structures in linear and two-dimensional infrared spectroscopy. Journal of Chemical Physics 120, 8201-8215, doi:10.1063/1.1689637 (2004).

134 Hamm, P., Helbing, J. & Bredenbeck, J. in Annual Review of Physical Chemistry Vol. 59 Annual Review of Physical Chemistry 291-317 (2008).

135 Demirdoven, N. et al. Two-dimensional infrared spectroscopy of antiparallel beta-sheet secondary structure. Journal of the American Chemical Society 126, 7981-7990, doi:10.1021/ja049811j (2004).

136 Bredenbeck, J. et al. Transient 2D-IR spectroscopy: Snapshots of the nonequilibrium ensemble during the picosecond conformational transition of a small peptide. Journal of Physical Chemistry B 107, 8654-8660, doi:10.1021/jp034552q (2003).

137 Woutersen, S., Mu, Y., Stock, G. & Hamm, P. Hydrogen-bond lifetime measured by time-resolved 2D-IR spectroscopy: N-methylacetamide in methanol. Chemical Physics 266, 137-147, doi:10.1016/s0301-0104(01)00224-5 (2001).

138 Hochstrasser, R. M. Two-dimensional IR-spectroscopy: polarization anisotropy effects. Chemical Physics 266, 273-284, doi:10.1016/s0301-0104(01)00232-4 (2001).

139 Kohlmann, O. et al. NMR diffusion, relaxation, and spectroscopic studies of water soluble, monolayer-protected gold nanoclusters. Journal of Physical Chemistry B 105, 8801-8809, doi:10.1021/jp011123o (2001).

140 Frischkorn, C. & Wolf, M. Femtochemistry at metal surfaces: Nonadiabatic reaction dynamics. Chemical Reviews 106, 4207-4233, doi:10.1021/cr050161r (2006).

141 Misewich, J. A., Heinz, T. F. & Newns, D. M. DESORPTION INDUCED BY MULTIPLE ELECTRONIC-TRANSITIONS. Physical Review Letters 68, 3737-3740, doi:10.1103/PhysRevLett.68.3737 (1992).

142 Menzel, D. & Gomer, R. DESORPTION FROM METAL SURFACES BY LOW-ENERGY ELECTRONS. Journal of Chemical Physics 41, 3311-&, doi:10.1063/1.1725730 (1964).

143 Redhead, P. A. INTERACTION OF SLOW ELECTRONS WITH CHEMISORBED OXYGEN. Can. J. Phys. 42, 886-& (1964).

144 Antoniewicz, P. R. MODEL FOR ELECTRON-STIMULATED AND PHOTON-STIMULATED DESORPTION. Physical Review B 21, 3811-3815, doi:10.1103/PhysRevB.21.3811 (1980).

145 Groeneveld, R. H. M., Sprik, R. & Lagendijk, A. EFFECT OF A NONTHERMAL ELECTRON-DISTRIBUTION ON THE ELECTRON-PHONON ENERGY RELAXATION PROCESS IN NOBLE-METALS. Physical Review B 45, 5079-5082, doi:10.1103/PhysRevB.45.5079 (1992).

146 Juhasz, T., Elsayedali, H. E., Smith, G. O., Suarez, C. & Bron, W. E. DIRECT MEASUREMENTS OF THE TRANSPORT OF NONEQUILIBRIUM ELECTRONS IN GOLD-FILMS WITH DIFFERENT CRYSTAL-STRUCTURES. Physical Review B 48, 15488-15491, doi:10.1103/PhysRevB.48.15488 (1993).

147 Wang, Z. & Ma, L. Gold nanoparticle probes. Coordination Chemistry Reviews 253, 1607-1618, doi:10.1016/j.ccr.2009.01.005 (2009).

148 Dhar, S., Daniel, W. L., Giljohann, D. A., Mirkin, C. A. & Lippard, S. J. Polyvalent Oligonucleotide Gold Nanoparticle Conjugates as Delivery Vehicles for Platinum(IV) Warheads.

Journal of the American Chemical Society 131, 14652-+, doi:10.1021/ja9071282 (2009).

149 Hirsch, L. R. et al. Nanoshell-mediated near-infrared thermal therapy of tumors under magnetic resonance guidance. Proceedings of the National Academy of Sciences of the United States of America 100, 13549-13554, doi:10.1073/pnas.2232479100 (2003).

150 Dulkeith, E. et al. Fluorescence quenching of dye molecules near gold nanoparticles: Radiative and nonradiative effects. Physical Review Letters 89, doi:203002 10.1103/PhysRevLett.89.203002 (2002).

151 Krpetic, Z. et al. Inflicting Controlled Nonthermal Damage to Subcellular Structures by Laser-Activated Gold Nanoparticles. Nano Letters 10, 4549-4554, doi:10.1021/nl103142t (2010).

152 Bonn, M. et al. Phonon- versus electron-mediated desorption and oxidation of CO on Ru(0001). Science 285, 1042-1045, doi:10.1126/science.285.5430.1042 (1999).

153 Hussain, I., Brust, M., Papworth, A. J. & Cooper, A. I. Preparation of acrylate-stabilized gold and silver hydrosols and gold-polymer composite films. Langmuir 19, 4831-4835, doi:10.1021/la020710d (2003).

154 Liu, X., Atwater, M., Wang, J. & Huo, Q. Extinction coefficient of gold nanoparticles with different sizes and different-capping ligands. Colloids Surf. B 58, 3-7 (2007).

155 Bennett, A. E., Rienstra, C. M., Auger, M., Lakshmi, K. V. & Griffin, R. G. HETERONUCLEAR DECOUPLING IN ROTATING SOLIDS. Journal of Chemical Physics 103, 6951-6958, doi:10.1063/1.470372 (1995).

156 Balazs, Y. S. & Thompson, L. K. Practical methods for solid-state NMR distance measurements on large biomolecules: Constant-time rotational resonance. Journal of Magnetic Resonance 139, 371-376, doi:10.1006/jmre.1999.1791 (1999).

157 Levitt, M. H., Raleigh, D. P., Creuzet, F. & Griffin, R. G. THEORY AND SIMULATIONS OF HOMONUCLEAR SPIN PAIR SYSTEMS IN ROTATING SOLIDS. Journal of Chemical Physics 92, 6347-6364, doi:10.1063/1.458314 (1990).

158 Petkova, A. T. et al. A structural model for Alzheimer's beta-amyloid fibrils based on experimental constraints from solid state NMR. Proceedings of the National Academy of Sciences of the United States of America 99, 16742-16747, doi:10.1073/pnas.262663499 (2002).

159 Luca, S., Heise, H. & Baldus, M. High-resolution solid-state NMR applied to polypeptides and membrane proteins. Accounts of Chemical Research 36, 858-865, doi:10.1021/ar020232y (2003).

160 Knight, W. D. NUCLEAR MAGNETIC RESONANCE SHIFT IN METALS. Physical Review 76, 1259-1260, doi:10.1103/PhysRev.76.1259.2 (1949).